Title
High temperature studies of electric-field noise in a surface ion trap

Author
Noel, Crystal

Publication Date
2019

Peer reviewed|Thesis/dissertation

High temperature studies of electric-field noise in a surface ion trap

by

Crystal Noel

A dissertation submitted in partial satisfaction of the

requirements for the degree of

Doctor of Philosophy

in

Applied Science and Technology

in the

Graduate Division

of the

University of California, Berkeley

Committee in charge:

Professor Harmut Häffner, Chair
Professor Dmitry Budker
Professor James Analytis

Spring 2019

High temperature studies of electric-field noise in a surface ion trap

Abstract

High temperature studies of electric-field noise in a surface ion trap

by

Crystal Noel

Doctor of Philosophy in Applied Science and Technology

University of California, Berkeley

Professor Harmut Häffner, Chair

Electric-field noise is a major limiting factor in the performance of ion traps and other quantum devices. Despite intensive research over the past decade, the nature and cause of electric field noise near surfaces is not well understood. This dissertation reports the high-temperature dependence of electric-field noise above an Al-Cu surface using a trapped $^{40}Ca^{+}$ ion as a probe.

We employ a novel setup with a surface ion trap mounted on a heater for studies of the temperature dependence of electric-field noise. To characterize the Al-Cu material, we explore the effects of heat treatment through *ex situ* annealing followed by inspection in a scanning electron microscope. To calibrate the temperature of the trap, we demonstrate the use of thermal imaging for monitoring the temperature of an ion trap in vacuum.

The temperature and frequency dependence of electric-field noise above the surface is measured using the heating rate of a single ion in a surface-electrode Paul trap. We find that the heating rate saturates at temperatures greater than 450 K. We find that the frequency dependence shows a $1/f$ behavior, and has a lower frequency scaling exponent at high temperatures than at room temperature. We show that these results are a reflection of the surface-related noise by eliminating other possible sources of noise.

Building on historical data for resistance fluctuations in thin films, we develop the thermally-activated fluctuator model to describe the results. We find that a broad distribution of fluctuators with energy barriers peaked around 0.5 eV accurately models both the temperature and frequency dependence of the electric-field noise measured. We present the interpretation of this model as a way to infer that the cause of electric-field noise in the trap is likely defect motion in the metal surface, connecting the problems faced in ion trapping to a large body of work in solid state physics.

To the women who came before me

and to those who will come after.

Contents

List of Figures

List of Tables

Acknowledgments

A PhD is an emotional journey that nothing and no one can prepare you for. It requires support, and I got it from lots of different people.

My family has always supported me and I could not have done this without them. Even though they lived thousands of miles away, I always felt their love and interest in my well-being.

It started in Berkeley with the house on the hill. Matt Gilbert is a supportive and caring friend. I know he is destined for greatness, and he has encouraged me to believe the same about myself. Charlie Hill was a beacon of integrity in the darkness of graduate school and I have to thank him for being the roommate I needed and an incredible friend.

I have many lab mates to thank, some of which I will mention here. Tony Ransford was the best first lab partner anyone could have asked for. Dylan Gorman kept me sane with his quick wit and by being an understanding friend. I found a great friend and colleague in Erik Urban. I was lucky to have post-doc mentors like Boerge Hemmerling, Clemens Matthiesen, Sara Mouradian, and Eli Megidish. My thesis work had more downs than ups, but I was not suffering alone. I need to thank Maya Berlin-Udi and Clemens Matthieson, who put up with me as I dealt with it all in my own way. Their patience, support, and perseverance got me through it all.

Hartmut has been an advisor, a mentor, and a friend. He has taught me what makes a good physicist.

The physics support staff are extremely friendly and I want to thank them for doing their jobs so well that it makes graduate school just a little less unpleasant. Anne Takizawa and Joelle Miles and the entire physics department adopted me, right up until the moment I walked across the stage. Carlos Bustamante is not only a helpful staff member, but also a friend.

The Applied Science and Technology community is small, but supportive in its own way. I'd like to especially thank Professor Dave Attwood, Kenny Gotlieb, Elio Champenois, Jonathan Morris, Brandon Wood, and Kasra Nowrouzi for their kindness and support.

There is one person who I cannot thank enough, who has supported me in a way that only someone who loves me fiercely could do, Calvin McPhail-Snyder.

Chapter 1

Introduction

There is growing investment and interest in quantum information related research that uses well controlled quantum systems to study complex phenomena. Successful engineering of a large quantum simulator or universal computer promises opportunities for further understanding of topics like chemistry and high temperature superconductors [1].

The fundamental building block for quantum simulation or computation is a qubit (quantum bit), which is a two-state quantum system that is well-controlled and isolated from the environment. Trapped ions make fantastic qubits [2]. Quantum information can be encoded in long-lived electronic states, and the strong Coulomb interaction between ions can be used to create entanglement. Ions are trapped by oscillating electric fields and laser light provides quantum control over the qubit. The trap itself is often a small chip that is patterned with electrodes where voltages are applied to create the necessary fields. These chips can be micro-fabricated using processes developed in the silicon industry.

Ions in the same trap are coupled via the Coulomb interaction such that information can be transferred between ions via their shared motional modes. However, oscillating electric fields cause decoherence of the motion of trapped ion qubits. When trapped close to a surface, ions are sensitive to both static and oscillating electric fields created at the surface and in the bulk of the trap material. Ions are not the only quantum technology that suffer from surface-related noise; others include superconducting qubits and NV-centers in diamond [3, 4]. Despite intensive research over the last decade, the cause of electric-field noise at surfaces is not well understood. In this thesis, we aim to illuminate the source of the noise in a micro-fabricated ion trap not only to understand the physical mechanism, but also to work towards creating reliable low-noise ion traps for future research in quantum information.

Towards these goals, we perform high-temperature studies of electric-field noise in a surface ion trap. This work required integration of an industrial heater into the ultra-high vacuum ion trapping chamber. The heater used was designed for operation above 1000°C in high-vacuum. High-temperature operations in ultra-high vacuum are made difficult by the increased outgassing and low melting or burning temperature of some materials.

We found that the noise increased with increasing temperature, as was expected, but then saturated above about 200°C. We devised extensive checks to verify the results were due to

surface-related electric field noise, and not another technical noise source in the experiment. We find that a single model, the thermally activated fluctuator (TAF) model, describes both the frequency and temperature scaling results. The model was developed by Dutta, Dimon, and Horn [5] to explain resistance fluctuations in metal films. It is the high temperature realization of the tunneling two-level system (TTLS) noise common in superconducting qubit technologies [6] or the two-level states in amorphous solids [7]. The results in this thesis advance the understanding of electric-field noise in ion traps by connecting to a large body of work in solid state physics and highlighting the role that the structure of the metal might play.

The following chapters build to the TAF model interpretation of the electric-field noise in a surface ion trap. In Chapter 2, the fundamental physics of ion trapping and qubit control are outlined. Chapter 3 provides an overview of electric-field noise in ion traps, specifically the previous information related to temperature scaling of the noise. In addition, Chapter 3 details how the electric-field noise is measured in this work. The experimental setup, including the unique heater used for the high-temperature studies, is described in Chapter 4. Chapter 5 contains possible high temperature effects and the temperature calibration. Finally, the results are summarized in Chapter 6 and they are put into the context of the TAF model in Chapter 7.

Chapter 2

Quantum control

Linear Paul traps confine charged particles in an approximate harmonic potential minimum. In this work, we focus on trapping a single $^{40}Ca^{+}$ ion using a surface trap. A surface trap is a Paul trap with the electrodes fabricated onto a single plane. The electronic energy levels of $^{40}Ca^{+}$ can be simplified to a two-level system (qubit) that is addressable using lasers. The motional state of the ion can also be manipulated and read-out using lasers. In this chapter, we describe the fundamental aspects of quantum control of a trapped $^{40}Ca^{+}$ ion.

2.1 Paul trap

A Paul trap uses both static and oscillating electric fields to confine charged particles using a quadrupole potential, which when expanded around the potential minimum is:

$$\Phi = \frac{\Phi_0}{r_0^2}\left(\alpha x^2 + \beta y^2 + \gamma z^2\right).$$

In this equation, Φ_0 is the voltage applied to the electrode a distance r_0 away from the trapping location. Coefficients α, β, and γ determine the shape of the potential. From LaPlace's equation, $\nabla^2\Phi = 0$ [8], it is impossible to set these coefficients to be all the same sign and create a confining potential in every direction with static voltages. Illustrated in Fig. 2.1a is a simple four rod electrode configuration with a vanishing γ coefficient.

Instead, if an oscillating potential is also applied such that

$$\Phi_0(t) = V_{\mathrm{DC}} + V_{\mathrm{RF}}\cos(\Omega_{\mathrm{RF}}t)$$

then the equation of motion becomes the Mathieu equation in each direction, e.g. for x:

$$\frac{d^2x}{d\tau^2} + (a - 2q\cos(2\tau))x = 0$$

where $\tau = \frac{1}{2}\Omega_{\mathrm{RF}}t$ and $a_x = -8\alpha QV_{\mathrm{DC}}/mr_0^2\Omega_{\mathrm{RF}}^2$ and $q_x = 4\alpha QV_{\mathrm{RF}}/mr_0^2\Omega_{\mathrm{RF}}^2$ are the Mathieu parameters, where m is the mass of the ion and Q is the charge. The ratio of a_x to q_x is the

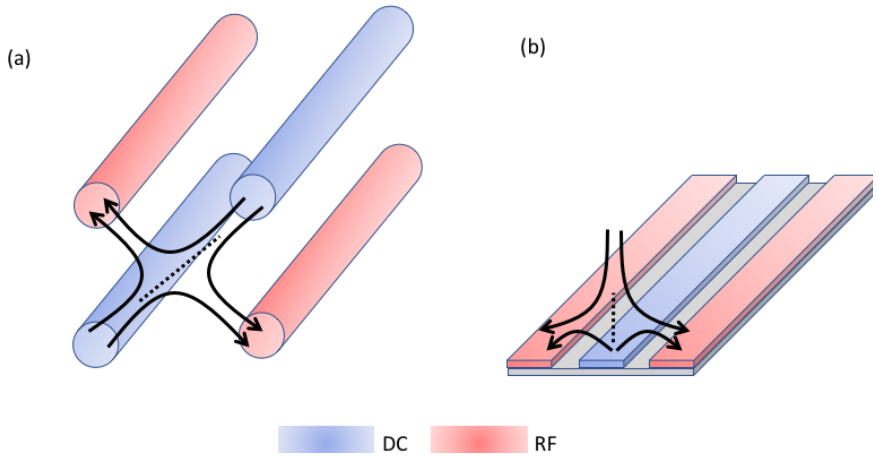

Figure 2.1: (a) 3D linear paul trap design with four rods: two that are direct current (static voltages) or ground, and two have an applied radiofrequency tone (oscillating voltage). Electric field lines are shown for when the RF rods are at a potential lower than the DC rods, creating a quadrupole potential, or a saddle point, that is confining in the direction indicated by the dashed line. When the RF voltage changes to a potential above that of the DC rods, the confinement will be in the direction perpendicular to the dashed line. Pseudopotential confinement occurs everywhere along the center of the trap. DC end caps are added at either end for the third dimension of confinement. (b) 2D Paul trap design, or linear surface trap, with the same field lines and confining direction indicated by the dashed line. This design exhibits the same trapping behavior along the center axis as (a), but with a lower trap depth. DC electrodes placed along the outside of the RF electrodes can provide the third dimension of confinement.

strength of the DC confinement V_{DC}, over the RF confinement V_{RF}. For appropriate choices of the confinement strength, V_{DC}, V_{RF}, and frequency used, Ω_{RF}, there is a stable trapping configuration for an ion of a given charge and mass that satisfies the stability requirements imposed on the Mathieu parameters. Detailed plots of the stability regions depending on the a and q parameters are available in the Roos thesis and elsewhere [9, 10]. The motion of the ion in a potential that is symmetric about x and y is then

$$x(t) = x_0 \cos(\omega_x t + \phi_x)\left(1 + \tfrac{q_x}{2}\cos(\Omega_{\mathrm{RF}} t)\right) \tag{2.1}$$

where $\omega_x = \frac{\Omega_{\mathrm{RF}}}{2}\sqrt{a_x + q_x^2/2}$ is the secular frequency of the ion motion in the x direction and ϕ_x is an arbitrary phase (and similarly for y) [9]. In the axial z direction, the quadruple confinement is typically provided by DC voltages.

If the ion is sufficiently close to the center of the trap, then a pseudo-potential approximation can be made, ignoring the motion at Ω_{RF} (the second term of Eqn. 2.1), called micromotion. This approximation will generally hold if the ion remains near the ground state of motion and positioned in the center of the trap. Stray static electric fields that

displace the ion from the center of the trap modify the equation of motion and result in an additional term x_E:

$$x(t) = (x_E + x_0 \cos(\omega_x t + \phi_x)) \left(1 + \tfrac{q_x}{2} \cos(\Omega_{\mathrm{RF}} t)\right), \tag{2.2}$$

and this motion exhibits micromotion in the pseudopotential approximation. These stray fields can be compensated using additional DC voltages. The pseudo-potential is then a harmonic oscillator potential with oscillation frequency $\omega_{x,y}$ in the radial directions. With a given trap geometry, simulations can be used to find a stable (conditioned on real frequency solutions, $\omega_{x,y} \in \mathbb{R}$) radio-frequency amplitude and voltage to apply to the quadrupole RF-electrodes for successful trapping. In general, the solution in use will be when the DC confinement is small and $a_x \ll q_x \ll 1$. In the axial direction, the potential is set to be approximately harmonic by applying DC voltages to trap electrodes to create a potential of the form

$$U_2 = \frac{2z^2 - x^2 - y^2}{2}$$

at the chosen trapping location in the pseudopotential minimum. The voltages necessary to achieve such a potential can be obtained using an electrostatic simulation given a certain trap geometry.

2.2 Surface traps

Traditional 3D ion trap designs such as the four rods shown in Fig. 2.1a are not readily scalable into a system of a large number of ions. They do not provide the necessary local control of the potential to split and merge large chains of ions. By fabricating electrodes into a single 2D plane [11], a quadrupole potential can still be created using radiofrequency fields as shown in Fig. 2.1b. Surface traps were adopted in order to scale to many qubits, provide flexibility in design, increase control over potentials, and integrate other components such as electronics or optical elements.

On the large scale, a surface trap can be as simple as a printed circuit board [12], requiring only an insulating substrate with a suitable pattern of conducting electrodes. Using microfabrication techniques standard for electronic device fabrication, smaller scale traps can be made that trap ions 30-500 μm from the surface, depending on the size of the geometry of the electrodes [13, 14]. Materials with low-RF loss such as fused silica or sapphire are generally used as the insulating substrate, and the top electrode layer is usually a metal such as gold or aluminum alloys. Electrodes can be patterned with an etching process using chemicals or lasers. Recent progress in surface trap fabrication has led to extension of the design to include through-silicon-vias [15], sometimes with multiple conducting layers in a stack under the trap surface [16].

The trap depth is the energy an ion needs to classically escape a confining potential. In a traditional 3D rod trap, the trap depth is determined by:

$$D_x = \frac{m}{2}\omega_x^2 d_x^2$$

where d_x is the distance between the center of the trap and the electrode (similarly in the y and z directions). In these types of traps, the distance is usually greater than 1 mm and the depth is a few eV. The depth of a surface trap must, in general, be determined using numerical simulations due to the breakdown of the quadrupole potential away from the center of the trap (see Fig. 2.1b) and is weakest in the direction perpendicular to the surface. In general, surface trap depths are lower than their 3D counterparts ($\sim$ 50 meV), and the ions are trapped much closer to the electrodes ($\sim$ 100 μm). With a lower trap depth, collisions of ions with background gas can easily transfer enough energy for the ion to leave the trap, making the lifetime of trapped ions shorter than their 3D counterparts. In addition, the proximity to the surface means that electric-field noise increases the energy of the ions, resulting in heating of the secular motion (discussed in Chapter 3). The high electric-field noise limits the viability of surface traps in the future for trapped ion quantum processing and is the subject of this dissertation.

2.3 Calcium ion

The $^{40}Ca^{+}$ ion has one valence electron and its energy levels are shown in Fig. 2.2 with relevant transition wavelengths labeled. A qubit requires a stable two-level system, and in $^{40}Ca^{+}$ the $S_{1/2}$ and $D_{5/2}$ states can be used for this purpose since $D_{5/2}$ is long-lived ($\tau \approx 1$ s). In an applied magnetic field, the $S_{1/2}$ ($D_{5/2}$) level splits into 2 (6) energy levels due to the Zeeman effect (Fig. 2.2b) where the shift in energy for a sub-level with Landé factor g_j is [9]

$$\Delta E = g_j \mu_B B m_j$$

that results in a Zeeman splitting of 4.2 kHz/mG for the $S_{m=-1/2}(g_j = 2) \rightarrow D_{m=-5/2}(g_j = 6/5)$ transition [17]. These levels are used as the qubit (referred to as carrier) in this thesis, and the transition can be addressed using laser light near 729 nm.

There is a finite probability that if the ion is in the $P_{3/2}$ ($P_{1/2}$) state it will decay into $D_{5/2}$ ($D_{3/2}$), which is out of the S-P manifold used for cooling and readout. In addition to the qubit laser, there are two beams used for pumping out of the D state and into the P state. When the ion is trapped in $D_{5/2}$, light near 854 nm is used to pump into $P_{3/2}$ (used during electronic state preparation). Similarly, when the ion is trapped in $D_{3/2}$, light near 866 nm is used to pump into $P_{1/2}$ (used during cooling and readout).

2.4 State preparation and measurement

Optical pumping

Optical pumping is used to prepare the electronic state of the ion into the desired qubit $S_{-1/2}$ ground state. The 729 nm laser is tuned to the $S_{+1/2} \rightarrow D_{-3/2}$ transition as indicated by OP in Fig. 2.2b. The 729 drives the ion from $S_{+1/2} \rightarrow D_{-3/2}$ and the broad 854 nm

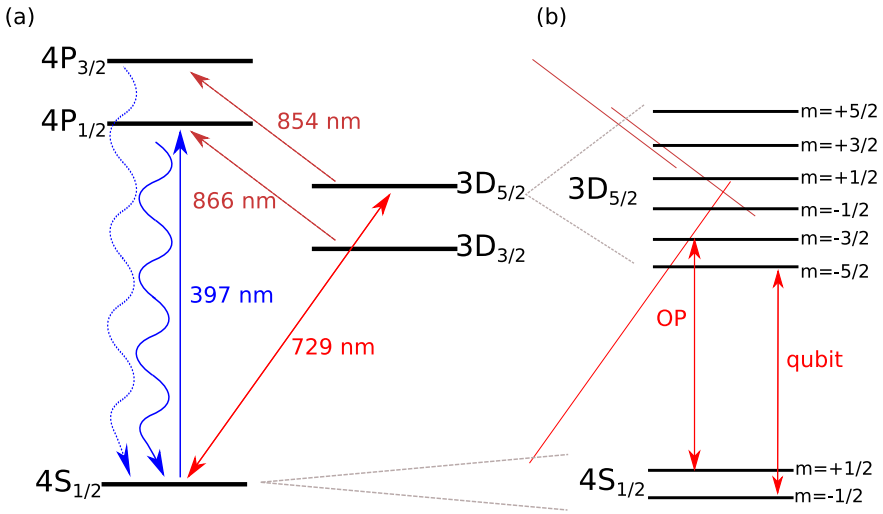

Figure 2.2: (a) $^{40}Ca^{+}$ energy level diagram and wavelengths of relevant transitions. The $S_{1/2} \rightarrow P_{1/2}$ transition is addressed with 397 nm light for Doppler cooling and readout. Since there is a finite probability that the ion decays into $D_{3/2}$ from $P_{1/2}$, light near 866 nm is used during cooling and readout to repump the ion into the $S_{1/2}$ - $P_{1/2}$ manifold. The qubit formed by the $S_{1/2}$ and $D_{5/2}$ states can be controlled with light near 729 nm. (b) Zeeman splitting of the qubit states in a magnetic field. The 'qubit' arrow indicates the chosen carrier transition in this work, which can be addressed using light near 729 nm. In addition to the 854 nm repump, the transition used for optical pumping is labeled 'OP'.

re-pump sends the ion into the $P_{3/2}$ state which decays quickly via a 393 nm transition to $S_{-1/2}$. Using several cycles of this scheme we achieve near 100% preparation into $S_{-1/2}$.

Doppler cooling

The motional state of the trapped ion is prepared in a thermal state with a small expectation value of the number of motional quanta, n, using Doppler cooling. Absorbed photons exert a radiation pressure force on atoms in a laser field. In a simplified two-level atom, if the laser is tuned lower than the transition by an amount δ, then due to the Doppler effect, atoms moving into the beam will preferentially absorb the photons. The recoil of the emitted photon after absorption is in a random direction, so on average this is a cooling force when the atom is confined. Using this force to cool trapped atoms is called Doppler cooling [18]. In calcium, the $S_{1/2} \rightarrow P_{1/2}$ transition is good for Doppler cooling; since the lifetime of the excited state is only 7.7 ns and many photons will scatter in a short amount of time [9]. The 866 nm repump beam is used to counteract decay from $P_{1/2}$ into the metastable $D_{3/2}$ state. The cooling is most efficient when the laser detuning is set to half the linewidth below the transition, $\Delta = -\Gamma/2$. The lowest temperature that can be reached is [18]

$$k_B T_{dop} = \tfrac{1}{2}\hbar\Gamma. \tag{2.3}$$

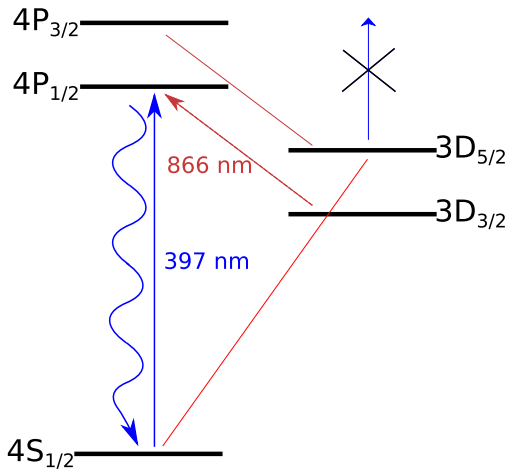

Figure 2.3: During readout, both the 397 nm and the 866 nm beams are used. If the ion is in the ground state, then it will fluoresce 397 nm photons and the ion is observed as 'bright'. The broad 866 nm beam insures that the ion is not trapped in the $D_{3/2}$ state. If no fluoresence is observed (the ion is 'dark'), then it is in the excited state.

For the $S_{1/2} \rightarrow P_{1/2}$ transition with $\Gamma = 20$MHz, an ion with a motional frequency of 1 MHz will cool to about $\bar{n} = 10$.

State read-out

The electronic state read-out scheme is shown in Fig. 2.3. If the ion (qubit) is in the ground electronic state, then with applied 397 nm and 866 nm beams the ion will fluoresce. Conversely if the ion is in the excited $D_{5/2}$ manifold, then there will be no fluorescence. Readout usually lasts about 0.5-1 ms. Photons are collected by a photo-multiplier tube with typical count rates of 30-40 k-counts/s in the bright state. Dark state counts are typically less than 1 k-counts/s, allowing for low readout errors even with poor light collection efficiency. In practice, an experiment is repeated 100 times to build up statistics. A histogram is constructed with two groups of counts for 'bright' and 'dark' that have little to no overlap. A threshold is chosen between the two groups, above which the ion is considered 'bright'.

2.5 Qubit coherent operations

Laser-ion interaction

With the choice of $S_{m=-1/2}$ and $D_{m=-5/2}$ as our two-level system, we can tune a laser to address the transition with a qubit frequency ω_0 near $hc/(729\text{ nm})$ as shown in Fig. 2.2b. The energy of the two-level system is characterized by Pauli spin matrices σ_i, and the motional state of the ion by the harmonic oscillator creation and annihilation operators, $\hat{a}$ and $\hat{a}^\dagger$.

The Hamiltonian for the ion in the trap is described by

$$H_0 = \hbar\omega_t(\hat{a}^\dagger\hat{a} + \tfrac{1}{2}) + \tfrac{1}{2}\hbar\omega_0\sigma_z$$

with ω_t the trapping frequency. If a laser field is added to the system with frequency ν and wave-number k, the interaction is described by [9]

$$H_1 = \tfrac{1}{2}\hbar\Omega_0\left(\prod_s e^{i\eta_s(\hat{a}_s^\dagger+\hat{a}_s)}\sigma^+e^{-i\nu t} + \prod_s e^{-i\eta_s(\hat{a}_s^\dagger+\hat{a}_s)}\sigma^-e^{i\nu t}\right)$$

for each motional mode s in 3D in the rotating wave approximation in the frame of the ion. The bare Rabi frequency, Ω_0, is determined by the coupling strength of the quadrupole transition and the amplitude of the applied field E and can be approximated by $\hbar\Omega_0 = \frac{k}{2}Eea_0^2$. If the laser makes an angle ϕ with a particular mode s, then for that mode

$$\eta_s = k\cos\phi\sqrt{\frac{\hbar}{2m\omega}} \tag{2.4}$$

is the Lamb-Dicke parameter describing the ratio of the spatial extent of the ground state wavefunction to the wavelength of the laser used for the interaction. If ϕ is small, the laser has overlap mostly on a single mode of motion, and the Hamiltonian in the interaction picture can be written as a 1D case,

$$H_I = \tfrac{1}{2}\hbar\Omega_0\left(e^{i\eta(\hat{a}^\dagger+\hat{a})}\sigma^+e^{-i\Delta t} + e^{-i\eta(\hat{a}^\dagger+\hat{a})}\sigma^-e^{i\Delta t}\right) \tag{2.5}$$

where $\Delta = \nu - \omega_0$.

This expression simplifies in the Lamb-Dicke regime ($\eta^2(2n+1) \ll 1$) and has significant coupling only to transitions that have $\Delta n \leq 1$. For the measurements in this thesis, the relevant transition is the carrier, where the laser is on resonance with the electronic transition ($\Delta = 0$), and the motional state of the ion is unchanged ($\Delta n = 0$). In this case, for a Taylor expansion at $\eta = 0$, the interaction Hamiltonian reduces to

$$H_I = \tfrac{1}{2}\hbar\Omega_n(\sigma^+ + \sigma^-) \tag{2.6}$$

$$\Omega_n = \Omega_0(1 - \eta^2 n)$$

If the laser wave vector has a projection on multiple modes of motion, then the occupation of other modes will contribute to the Rabi frequency of the flop:

$$\Omega = \Omega_0\prod_s\left(1 - \eta_s^2 n_s\right) \tag{2.7}$$

where the product is over the motional modes s with their respective η_s and occupation n_s values.

If the laser is tuned by the motional frequency from the carrier, then transitions that have $\Delta n = \pm 1$ occur, called the motional sidebands. If $\Delta = +\omega_t$ ($\Delta = -\omega_t$), then a quanta of motion is added (subtracted) and the internal state goes from the ground state to the excited state. The Rabi frequency of the blue (red) sideband, in which n is increased (decreased) is $\Omega_{\mathrm{BSB}} = \eta\sqrt{n+1}\Omega_0$ ($\Omega_{\mathrm{RSB}} = \eta\sqrt{n}\Omega_0$), where n is the starting occupation of the motional mode. Rabi flops on the motional sidebands also have a n dependence, and decay for an ion in a thermal state. The trap frequency can be measured by scanning the frequency of a laser over a motional sideband and calculating the frequency difference to the carrier.

2.6 Carrier Rabi flops

A Rabi flop on the carrier transition can be used to read out the motional state of a trapped ion due to the dependence of the Rabi frequency on the motional state. In a conventional two-state Rabi flop under the Hamiltonian $H_I = \frac{1}{2}\hbar\Omega_0(\sigma^+ + \sigma^-)$, the state flops sinusoidally between the two states with Rabi frequency Ω_0. If an ion is in the ground state of motion, the flop is sinusoidal and continues with full contrast for an arbitrary amount of time assuming there are no other dephasing mechanisms. Instead, if the ion is in a higher number state, then the Rabi frequency depends on n as in Eqn. 2.6. An illustration of these differences is depicted in Fig. 2.4a. Finally, if the ion is not in a single number state, but a combination, then the time evolution must be summed between them.

To determine the motional state of a trapped ion, we first assume the ion is in a thermal motional state. We consider the evolution of a starting state of $|S\rangle\langle S| \otimes \rho_{\mathrm{th}}$, which is the tensor product of the ground electronic state with a thermal state of motion. The state $\rho_{\mathrm{th}} = \sum_{n=0}^{\infty} p_n |n\rangle\langle n|$ is a maximal entropy state with no nonzero off-diagonal elements. For an ion in a thermal state of motion with average occupational state $\bar{n}$, the probability to be in each motional state p_n are [9]

$$p_n = \frac{1}{\bar{n}+1}\left(\frac{\bar{n}}{\bar{n}+1}\right)^n. \tag{2.8}$$

With a laser on resonance with the carrier transition, the time evolution under the Hamiltonian in Eqn. 2.6, is a Rabi flop with the excited state probability:

$$p_D(t) = \sum_{n=0}^{\infty} p_n \sin^2(\Omega_n t). \tag{2.9}$$

The result is a Rabi flop that decays in time to an incoherent state where $p_D(t) = 0.5$ as the Rabi frequencies for different n states become out of phase. This dephasing effect is illustrated for a few different n states in Fig. 2.4a. An example of a ground state and a thermal state Rabi flop are shown in Fig. 2.4b. We find that we can observe and extract $\bar{n}$ reliably for $\bar{n}$ up to about 150 quanta in the range of accessible trap frequencies around 1 MHz.

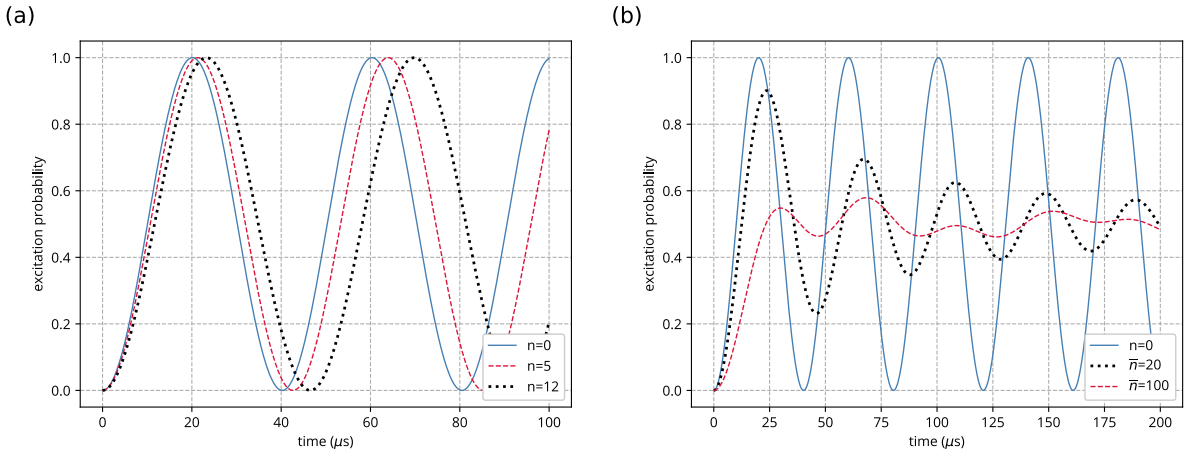

Figure 2.4: (a) Carrier Rabi flop expectations for a $^{40}Ca^{+}$ ion with a secular trap frequency of 800 kHz and motional states of $n = 0$ (blue solid), $n = 5$ (red dashed), and $n = 12$ (black dotted) showing how different motional states dephase over time. (b) The solid blue curve shows the expectation for a carrier Rabi flop for an ion in the motional ground state (n=0). The black dotted curve is for the same bare Rabi frequency Ω_0, but with a $^{40}Ca^{+}$ ion in a thermal state of motion with an average occupation $\bar{n} = 20$ and a trap frequency of 800 kHz. The red dashed curve shows the evolution under the same conditions, but with a thermal state with $\bar{n} = 100$.

2.7 Measuring heating rates

Electric-field noise at the trap frequency can couple to the ion motion and increase the motional mode occupation, which is measured as a heating rate in quanta per time. A heating rate measurement in this thesis consists of several carrier Rabi flops, with a wait-time inserted between state preparation and the excitation pulse. We determine the trap frequency by scanning the qubit laser near where we predict the motional sideband should occur, and calculating the frequency detuning of the sideband from the carrier. The measured trap frequency is used to calculate the Lamb-Dicke parameter, which enters into the extraction of $\bar{n}$ in a carrier Rabi flop.

An example of a single heating rate measurement is in Fig. 2.5, which shows four Rabi flops with varying wait-times, and therefore increasing $\bar{n}$. The heating rate $\dot{\bar{n}}$ is determined from a linear fit to the extracted $\bar{n}$ values. In the next chapter, we provide experimental details of this method and discuss the topic of electric-field noise more broadly.

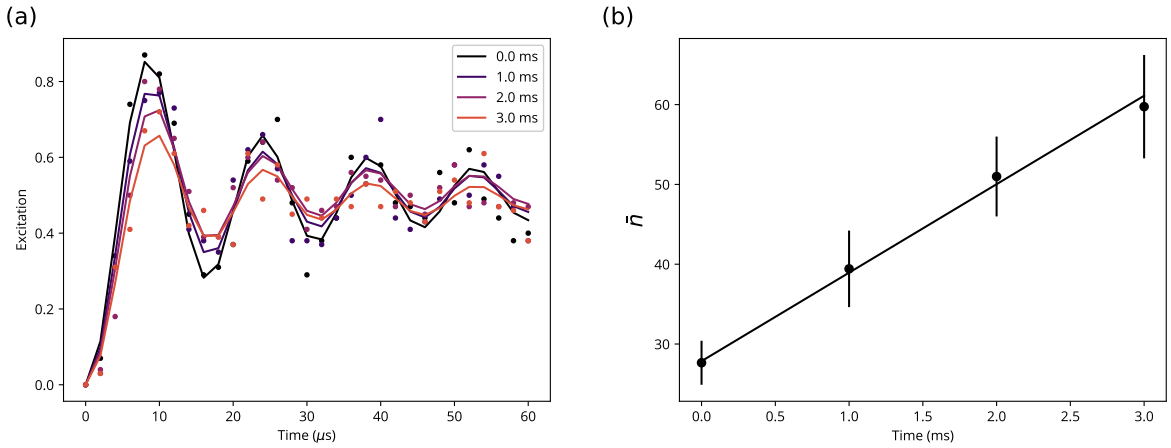

Figure 2.5: A sample heating rate measurement with a trap frequency of 880 kHz. (a) Four sequential carrier Rabi flops with increasing wait time, indicated by the legend. The bare Rabi frequency, or π-time is determined from the zero-wait flop. As the wait time is increased, so is the resultant motional occupation and the Rabi flop decays more quickly. (b) Corresponding fits to the carrier flops determine the average motional mode occupation assuming a thermal distribution. To find the heating rate $\dot{\bar{n}}$, we use a linear fit; in this case the heating rate is 11(2) quanta/ms.

Chapter 3

Electric-field noise (EFN)

A trapped ion is sensitive to electric-field noise (EFN) at the normal mode frequencies of the trapping potential. In the limit of small micromotion, the electric-field noise spectral density S_E is related to the heating rate $\dot{\bar{n}}$ by [19]

$$\dot{\bar{n}} = \frac{q^2}{4m\hbar\omega} S_E(\omega, T, d) \tag{3.1}$$

where q is the charge of the ion, m is the mass, and ω is the motional frequency. Here we also assume a strong scaling of S_E that decreases with frequency to neglect micromotion sideband contributions from noise at the drive frequency of the trap. S_E can depend on factors such as frequency ω, temperature of the trap itself T, and distance to the nearest surface d.

The main source of EFN, in a carefully engineered system, is the surface of the trap itself. If a fluctuating electric-field has a frequency component and direction overlapping a particular mode, then it will add energy to that motional mode. By measuring the occupation of the mode over time (heating rate), we can extract the noise spectral density S_E. The behavior of S_E is analyzed to understand the source of the noise. In this chapter, we discuss previous measurements of EFN related to temperature and frequency behavior. We describe the experimental details of the carrier Rabi method used to measure heating rates and study the temperature and frequency dependencies of EFN.

3.1 Limits of EFN on ion trap qubits

Naively, one could avoid the problem of EFN by building larger traps where ions are trapped far from any surfaces. However, in order to scale ion traps into many-qubit systems it is desirable to make the traps smaller. Trapping close to the surface decreases the voltages needed, and therefore the power dissipation at the trap that could cause heating of the substrate. It will likely be necessary to shuttle ions quickly between trapping regions for particular operations or storage. Fast shuttling with low voltages requires that the ions are

close to the electrodes for increased field strength. Shuttling and local addressing operations will also require fine control of the potential on the scale of the ion spacing (several microns) [20]. Coupling the motion of ions to other ions or other hybrid systems such as integrated microwave components [21] or coupling via an integrated floating electrode [22], requires small ion-electrode distances.

Single qubit gates use carrier Rabi flops, which have a second order dependence on n (Eqn. 2.6). While for one single qubit gate, this effect might be negligible, if there are many gates in a long sequence (without sympathetic cooling), then the carrier flop will deteriorate over the length of the sequence. For a sequence of 1000 gates each lasting 10 μs the entire sequence will last a total of 10 ms. If the heating rate is 100 quanta/s, then by the end of the sequence the ion will have acquired 1 quanta, which is enough to change the Rabi frequency by 1%. These kinds of errors could dominate the error rate of long sequences of gates.

Two qubit gates may be even more limited by heating rates than single qubit gates. Entanglement between trapped ions is mediated through their shared motional modes. The original proposal for an entangling gate by Cirac and Zoller [23] relied on the use of ground state cooled ions. Relaxing this requirement allows for higher fidelity gates with more realistic cooling parameters. An entangling gate that does not require ground state cooling was proposed by Mølmer and Sørensen in 1999 [24]. Known as the MS gate, it has become the popular choice of entangling gate in the ion trap community. The gate involves driving the ion near the red and blue sidebands to entangle the ions' motion with the internal states. In theory, the MS gate works for ions in thermal states of motion, but the gate is more sensitive to laser noise. Thermal state gates have been implemented, and show a lower fidelity than ground state cooled ions [25].

Heating of the motional mode during the gate, however, will cause an increased error rate even in theory. If we assume pessimistically that a change in n during the gate always causes an error, then a modest heating rate of 100 quanta/s in a 10 μs gate would cause an error rate on the order of 10^{-3}. Even if a mode with a low heating rate is chosen for the gate, ion strings have many modes of motion that could have a projection on the laser direction. The occupation of the other modes have second order contributions to sideband Rabi frequencies during the gate, similar to the carrier behavior (Eqn. 2.7). If those modes heat faster, the contribution could become significant.

The highest fidelities achieved at NIST have an error rate of $8(4) \times 10^{-4}$ with a heating rate contribution of 0.2×10^{-5} [26]. At Oxford, motional heating contributed 0.2×10^{-3} of the $1.1(7) \times 10^{-3}$ error budget of their best two-qubit gates. In these state of the art two-qubit gates, there are other contributing factors in the error rate such as spontaneous emission, but motional heating is certainly playing a role already, especially when considering that the above mentioned results were obtained in relatively large traps. Understanding the sources of EFN will help inform the design and engineering of ion traps with lower heating rates, and hopefully eliminate the contribution of heating to errors in trapped ion quantum computation.

3.2 Excess EFN

For a perfect metal electrode, we expect the lower limit of EFN to be thermal Johnson noise, but the observed heating rates are much higher. Figure 3.1 shows a compilation of published ion trap EFN measurements at room temperature. The indicated approximate Johnson noise limit is calculated for the trap used in this work and may not apply exactly to other measurements. Still, there are several orders of magnitude between any measured results and anticipated lower limits, and the excess noise has been termed 'anomalous heating'.

To attempt to reach the lower limit, electrode materials are chosen for high conductivity. Naively, the lower limit of electric-field noise spectral density is from the Johnson noise of the nearby electrodes alone [27, 28, 19]:

$$S_E = \frac{S_V}{D^2} = \frac{4k_B T R(\omega, T)}{D^2} \tag{3.2}$$

and the resistance R of the electrode is assumed to have no frequency dependence. The distance parameter D is an effective distance that is calculated by finding the electric field at the trapping position along the axis of motion E_z from a given electrode with an applied voltage V [29]:

$$E_z = \frac{V}{D}. \tag{3.3}$$

This effective distance is relevant to technical noise sources that are across the entire electrode, and it is not the same as the distance to the nearest surface, which is relevant for local, intrinsic noise sources. The effective distance for the trapping positions and motional mode used in this work is about 1 cm, even though the distance to the nearest surface is closer to 70 μm.

However, in addition to the noise from the electrodes, there are often many different electrical elements connected to trap electrodes like resistors, capacitors, and wires that can all contribute to the Johnson noise, effectively raising the real resistance R. It is possible to construct a low-pass filter that minimizes these effects, like the one used in this work (Sec. 4.5). The filter works by adding higher resistance components; the increased attenuation of the filter outweighs the increased thermal noise [19]. If such a filter is constructed, then the remaining contributing resistances are generally from the electrodes themselves, the wirebonds, and their connections to the filter network. In the case of the measurements in this work, we estimate the real resistance to be around 6-8 Ω [30].

For a 7 Ω real resistance with an effective distance of 1 cm, at 1 MHz trapping frequency, the Johnson noise anticipated is $S_E \approx 10^{-15}$ V^2/m^{2}Hz. At this limit, we would expect a flat frequency spectrum and, for a perfect thin metal film, a T^2 temperature dependence [31]. Having fabricated a trap, without directly measuring the resistance in the trapping region and likely destroying the trap, it is difficult to know the value of R exactly. It is also likely that the resistance has a frequency and temperature dependence that is not well understood. However, we can take this lower limit as an approximation, and note that measured values are several orders of magnitude away. We also note that even with similarly high-conductivity

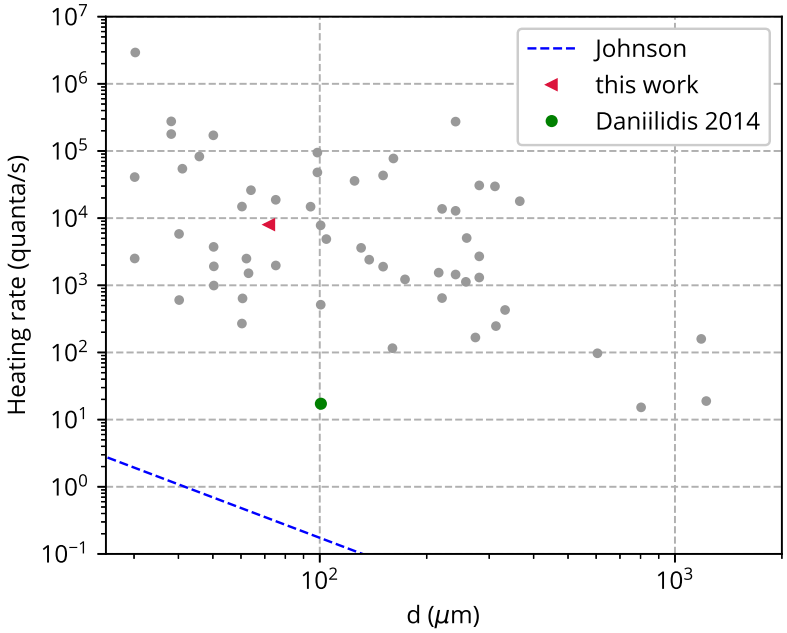

Figure 3.1: Electric-field noise measurements as collected by Brownnutt *et al.* [19] for traps at room temperature, normalized to 1 MHz trap frequency and mass of $^{40}Ca^{+}$ using Eqn. 3.1. The heating rate measured by Daniilidis *et al.* (green filled circle) was in a trap that had been argon-ion milled [30]. Indicated by the red triangle is the room temperature value for this work, which lies on the high side of observed heating rates. The dashed line represents the expected Johnson noise in those two highlighted results.

materials that some traps perform better than others for no discernible reason. Despite a decade of research, there is still not a clear understanding in the field of what dominates the 'anamalous heating'. The only guiding factor is that understanding dynamics at the surface of the trap seems to be the key.

3.3 Surface matters

Creating a perfect metal electrode is a difficult technical problem, and even with the precautionary measures taken with ion trap fabrication, we expect imperfections such as polycrystalline structures, surface roughness, and carbon contamination or oxide layers [32, 33, 34]. The strong scaling with distance to the electrode surface suggests that the source of the 'anomalous' heating is the surface of the trap itself. There are several other hints that coalesce to imply that noise processes on the metal surfaces play a key role in the excess electric-field noise observed.

One particularly strong piece of evidence is the success of ion-milling to significantly reduce heating rates. Argon-ion milling in particular is a popular method for cleaning metal surfaces that removes surface contamination such as carbon molecules or oxide layers. It works by filling the chamber with argon gas and creating energetic electrons that ionize the Ar^+ gas. The Ar^+ ions are then accelerated toward the sample by a voltage difference, and the ions bombard the surface. It is a violent process that removes up to several layers of contamination depending on the energy of the ions and the dosage to the surface. Researchers at NIST-Boulder and UC-Berkeley saw a 100-fold reduction in heating rate after Ar-milling the surface of gold and Al-Cu traps [32, 30].

There are even more hints that the surface dominates heating rates in surface traps. We observe heating rate increases after a trap is exposed to atmospheric contamination. Pulsed laser light has been shown to reduce heating rates above Al electrodes [35]. There is no indication that a particular electrode material performs better than another, for example in measurements in the same system Sedlacek *et al.* [36] observe similar behavior in Au and Nb traps prior to any surface treatment. This observation is evidence that the bulk properties of the electrode material were not dominating the noise in those traps. For these reasons, we focus on understanding the noise with models for processes happening on (or near) the surface of the trap.

3.4 Temperature scaling of EFN

Temperature is a particularly interesting parameter to study in relation to EFN because in general the proposed models have very different predicted temperature scalings. A simple model of diffusion of adatoms on a smooth surface predicts an Arrhenius temperature scaling [19, 34]. One model for a thin dielectric layer shows linear temperature scaling under somewhat simplified assumptions [37], but this dependency could vary depending on the properties of the dielectric, which are largely unknown in the case of an ion trap. The fluctuating adatom dipole model assumes atoms or molecules that are fixed to the surface and have phonon-induced vibrations. In this model, there are predicted correspondences between a range of frequency and temperature scalings [38]. Finally, there is a general model for $1/f$ noise from thermally activated fluctuators that has many possible temperature scaling expectations that should correlate with frequency scaling close to $1/f$. That model is described in detail in Chapter 7 and is the subject of this thesis. In general, measuring temperature and frequency scaling together could reveal the applicability of these models.

Previous results

Up to the results presented in this thesis, temperature dependence of EFN in ion traps has been measured in cryogenic experiments that range from a few Kelvin to around room temperature. The first time a trap was cooled in a cryostat, the heating rate was 10 times lower at 150 K than at room temperature [39]. Since then, improvements as large as 7-8 orders of

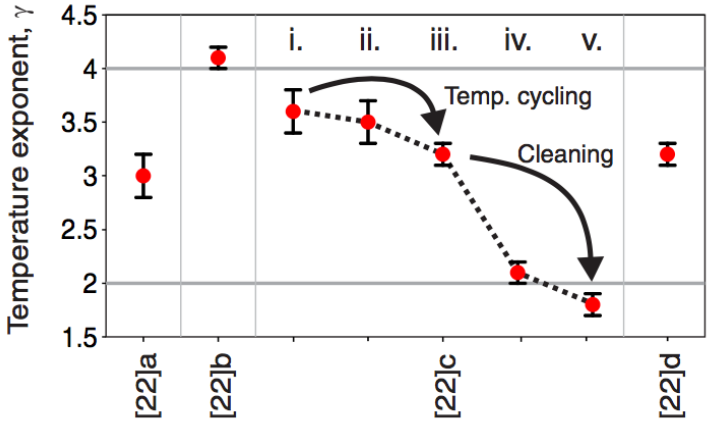

Figure 3.2: In these measurements from Labaziewicz *et al.*[41], various power law exponent γ values were observed at cryogenic temperatures. The letters a, b, c, d refer to different traps. Trap c underwent temperature cylcing up to 130 K after step i and up to 340 K after step ii. The cleaning after steps iii and iv refers to warming the trap to room temperature, breaking vacuum, and cleaning with lab solvents. This figure is from [19]

magnitude have been observed in traps near 4 K [40]. Brownnutt *et al.* remarked that 'bad' traps (those with high room temperature heating rates) seem to show more improvement at cold temperatures [19].

Prior to this work, detailed measurements of temperature scaling have been completed at MIT and MIT Lincoln Lab. The majority of those measurements have shown a power-law scaling in temperature of the form

$$S_E = S_0 \left[1 + \left(\frac{T}{T_0}\right)^{\gamma}\right]$$

with T_0 ranging from 17-70 K and γ between 1 and 4. Labaziewicz *et al.* [41] observed a variety of power law scalings after different treatments of gold-electrode traps such as exposure to air and cleaning in solvents. Those effects are summarized in Fig. 3.2. Detailed measurements in gold-electrode traps by Bruzewicz *et al.* in 2015 showed an average value of $\gamma = 1.59(3)$ across frequencies in the range of 0.6-1.5 MHz [42]. In what seems to be an outlier, one measurement in 2014 [43] showed an exponent that was lower at low temperatures than at high temperatures.

In recent results from MIT Lincoln Lab [36], several different temperature scaling behaviors were observed. As shown in Fig. 3.3, both the Au and Nb trap followed a power law at first. The traps were then treated with *ex situ* ion milling (ESIM), which removes the top layer of the surface including any carbon contamination or oxide layer. After treatment, the data are better described by an Arrhenius curve. The effects of the ESIM differed between

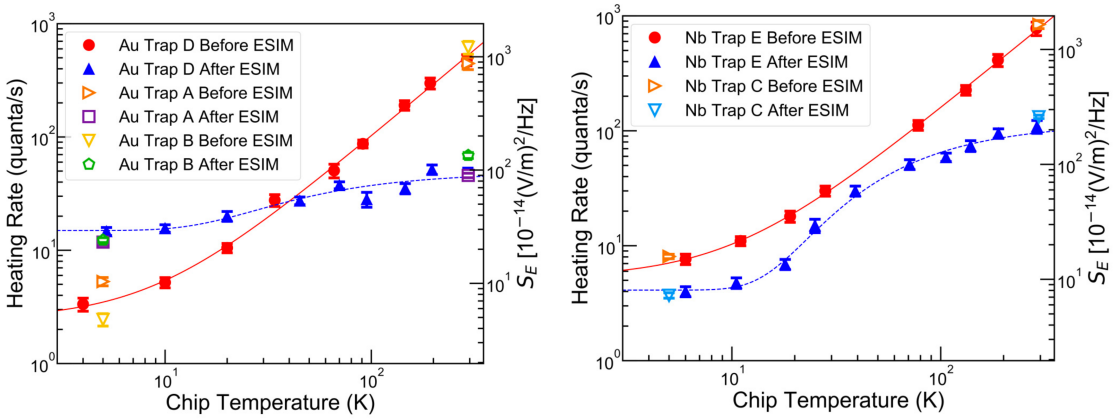

Figure 3.3: Recent results from MIT Lincoln lab show a variety of temperature scaling. ESIM refers to *ex situ* ion milling, which is known to reduce the heating rate in various types of traps. Important features to note are that the Au and Nb behaved similarly prior to cleaning, and exhibited a power law scaling consistent with previous results. After ion milling however, the data more closely follow an Arrhenius curve, and the materials seem to have responded differently. This figure is from [36].

materials, suggesting the source of the noise and the effects of the treatment and subsequent air exposure are material dependent.

In this work, we will also discuss frequency scaling measurements in conjunction with temperature. A range of power law frequency scalings have been previously observed. In published measurements, the value of the exponent, α has been around 0.5-1.5 [19]. At NIST, a scaling of 1.5 has been observed several times in gold traps [32, 44]. Lincoln Lab has published values ranging from 0.5 to 1.6 [43, 41, 42]. Berkeley traps made with Al-Cu that were not ion-milled have exhibited $\alpha \approx 1$ [30, 33]. To our knowledge, measurements for which a single model explains the scaling of noise as a function of both temperature and frequency have not been reported so far.

3.5 Experimental considerations for the carrier Rabi method

The carrier Rabi method for measuring heating rates is especially useful when the $\bar{n}$ values involved are high (> 10 quanta), since the effect being measured is Rabi frequency shifts that are second-order in the Lamb-Dicke parameter $\sim \eta^2 n$ (Eqn. 2.6). The Lamb-Dicke parameter typically has values around $\eta = 0.1$ for measurements presented in this thesis. There are several experimental considerations and limitations for using this method that we present here.

Intensity noise on the 729 nm light that drives the Rabi flop can also skew heating rate

measurements. If the noise is on the time scale of the repetition rate for each wait time, then it causes an additional decay of the flop. Since the noise would affect all the flops equally, the heating rate would not be very sensitive to this type of noise. However, if the noise if slower, then the bare Rabi frequency might change between flops. In this case, the bare Rabi frequency from the first flop would not work well for fits of subsequent flops. If drifts of the intensity continue on the scale of an entire heating rate measurement (a few minutes), then this could bias the heating rate up or down depending on the direction of the drift. The effects of intensity noise are more more pronounced for low $\bar{n}$ flops, since they require more cycles within a single flop to see the decay envelope. For high $\bar{n}$ flops such as the ones presented in this thesis, this effect is smaller than our experimental errors.

Stray-field compensation

To avoid micromotion-related heating effects, a preliminary step to a heating rate measurement is compensation of stray electric fields that displace the ion from the RF null. If a trapped ion is displaced from the RF null, there is a non-vanishing component of the electric field from the RF electrodes that directly couples voltage noise to the ion. In addition, the gradient of the noisy field from the RF electrode causes mixing between the micromotion and the secular motion of the ion in the trap, which demodulates the RF noise components. A detailed derivation of these effects is available in Brownnutt *et al.* [19].

Stray fields can be compensated using added static electric fields to push the ion into the RF null, indicated by a minimization of the observed micromotion. The micromotion will be as minimized as possible when the RF null and the DC null are in the same point in space. This motion also causes a modulation of the qubit laser light due to the corresponding Doppler shift. If the laser is scanned at Ω_{RF} detuned from the carrier, then a peak in the spectrum will be observed (a micromotion sideband). The amount of micromotion is measured by driving a Rabi flop of the micromotion sideband. We then minimize the Rabi frequency of this sideband by tuning the static fields applied, while maintaining high Rabi frequency on the carrier. In the case of the trap used in this thesis, the first-order micromotion Rabi frequency was more than 50 times lower than the carrier Rabi frequency once micromotion was compensated. The ratio of the first-order Rabi frequency R_1 to that of the carrier R_0 can be roughly converted to an amplitude of excess micromotion u using:

$$\frac{R_1}{R_0} \approx \tfrac{1}{2}\beta^2$$

where $\beta = |\vec{k} \cdot \vec{u}|$ is the modulation index of the micromotion, with $\vec{k}$ the wave vector of the laser, and $\vec{u}$ the excess micromotion [45]. For $\frac{R_1}{R_0} < 50$, the associated amplitude of excess micromotion is $|\vec{u}| < 23$ nm (ground state wavefunction spread is < 15 nm) in the direction parallel to the laser (axial direction in this case).

Rabi flop parameters

There are limitations to the parameters of Rabi flops that are accurately represented by fits to thermal distributions. If the Rabi frequency becomes comparable to the motional frequency, then the rotating-wave approximation breaks down. The power-broadened carrier transition overlaps the motional sidebands, which drives transitions that change the motional state unintentionally. The 2π-time of a single carrier flop is set to be about 20 μs, which is longer than one motional period.

The flop is measured up to at least 4π rotations to increase accuracy of the Rabi frequency fitting. At each time, for 100 repetitions, the pulse is applied and the ion electronic state is read out. This repetition builds up enough statistics to ascertain the excited state probability p_D. The uncertainties on the data follow Poissonian statistics where $\sigma = \sqrt{p * (1-p)/N)}$ is the standard error for N repetitions.

Fitting

To find $\bar{n}$ given the time evolution of the excited state probability $p_D(t)$, we fit the Rabi flop to Eqn. 2.9. We use least-square fitting that minimizes the residuals between the data and calculated thermal state evolution with a given $\bar{n}$, π-time, and optical pumping efficiency. The assumption that the ion is in a thermal state of motion holds because both the Doppler cooling process and the heating from noise are incoherent.

In general, the optical pumping was 95-100% efficient, meaning we efficiently prepared the internal electronic state into $S_{m=-1/2}$. The π-time or bare Rabi frequency is determined from the fit to the zero wait time flop in a given sequence, and is then held fixed in subsequent fits with increasing wait time. We assume the detuning from the carrier is negligible (the interaction is on resonance). A detuning would speed up the Rabi flop and could cause an underestimation of $\bar{n}$. The uncertainty in $\bar{n}$ is determined from the fit of the flop.

One way to decrease the uncertainty on the heating rate and account for slow drifts in parameters such as initial cooling and Rabi coupling due to laser beam drifts over time, is to measure several rates in a row and then group all the measured $\bar{n}$ into a single set before fitting the data with a linear model. It would also be advantageous to randomize the wait times, as long as the stability of the bare Rabi frequency, derived from the zero-wait time flop, is accounted for by repeating the zero-wait time flop often.

The Lamb-Dicke parameter η is calculated using Eqn. 2.4 from the measured trap frequency along the chosen axis of motion. In this work, the laser axis is parallel to the trap surface and at an angle $\phi = 11^\circ$ to the axis of DC confinement. If this angle were not small, it would be impossible to extract the occupation of a single mode with the carrier flops alone.

Chapter 4

Experimental setup

4.1 Overview

The ion-trap setup used in this work is unique because in order to study possible sources of electric-field noise, it combines normal ion trapping capabilities with surface science tools. In this chapter, we describe the full setup in detail. The vacuum chamber has several specialized tools and an involved process for achieving ultra-high vacuum necessary for trapping ions. The surface trap used in this thesis is a simple linear design fabricated on to a glass substrate. There is a heater that allows for temperature scaling studies of electric-field noise. Electronics are filtered to prevent unwanted voltage noise entering the system. Finally, there are several electrical components, connections, and voltage sources for trapping as well as the imaging components and lasers for ion measurement and manipulation.

4.2 Vacuum chamber

The vacuum chamber used in this experiment is larger than standard ion-trapping chambers to accommodate extra surface science capabilities. A photo of the chamber appears in Fig. 4.1 with important tools labeled. Attachments to the main chamber include:

- Residual Gas Analyzer (RGA) for monitoring the total pressure and partial pressure of different background gases based on their mass
- Resistively heated tube containing calcium granules that serves as a source for neutral calcium. This oven is mounted so that calcium atoms travel 90° to the laser that addresses the frequency sensitive transition for photoionization, which avoids any Doppler shifts.
- Auger spectrometer for analyzing surface composition of the trap and identifying surface contaminants such as carbon and oxygen
- All-metal angle valve attached to a double turbo pump for bake-out

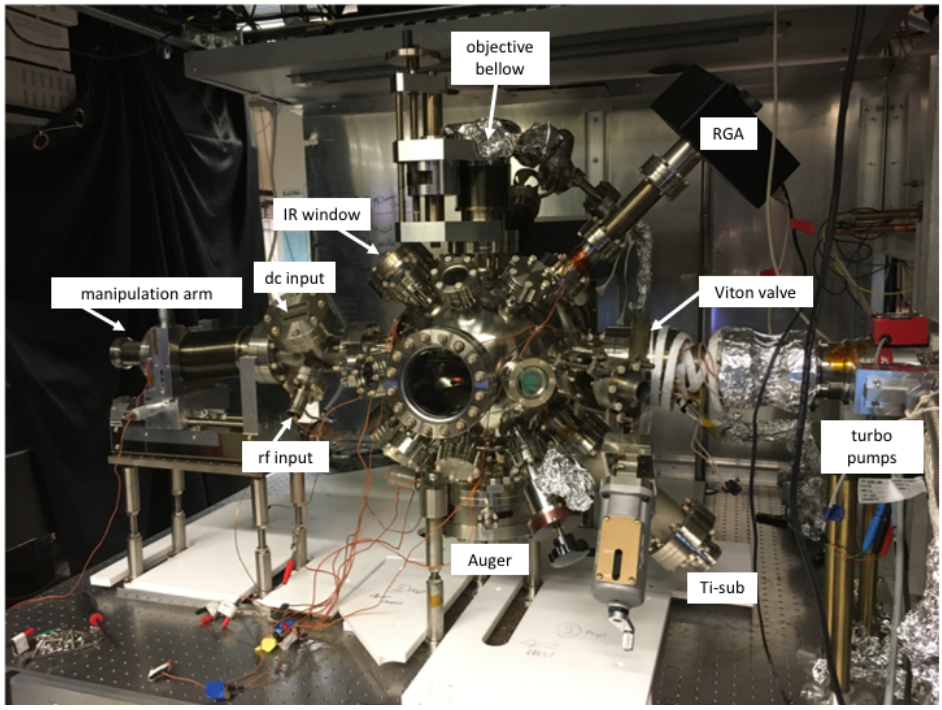

Figure 4.1: Components from the list in Sec. 4.2 are labelled on a photo of the vacuum chamber. The ion pump is on the opposite (back) side in this perspective. Only the back and left side walls of the Faraday cage are in place. The labeled Viton gate valve was removed during the leak hunting procedure, and is believed to be the cause of the elevated pressures. It has been replaced with an all-metal angle valve. Below the chamber are white sheets of Teflon for isolation of the heater tent from the chamber during baking and for insulation from ground when electronics are placed on the table

- Infrared transmitting ZnSe window for thermal imaging (Section 4.7)
- Several anti-reflection coated windows for transmission of laser beams (Section 4.6)
- Electron-gun with incorporated leak valve to allow for Argon milling (not used in this work)
- Ion pump with high capacity (1000 L/s) for maintaining UHV during regular operation without a mechanical pump. The high capacity is necessary due to the large surface area in the chamber that out-gasses to contribute to the background gas levels.
- Titanium-sublimation pump (Ti-sub)
- Manipulation arm with the trap mounted on the end that allows for rotation and translation of the trap in vacuum.

Achieving UHV at levels suitable for ion trapping ($< 10^{-11}$ torr) is no small feat. Doing so in a chamber with so many extra components only makes it that much more difficult. Careful consideration must be taken when choosing materials to use inside the vacuum to ensure that there is no outgassing at levels above 10^{-11} torr at room temperature. All-metal components are preferred, but some insulating materials are also necessary. Macor ceramic and UHV Kapton are in use in this chamber. Each flange is sealed using a copper gasket (CF) that must be tightened in a star pattern around the flange with small steps in each turn of a bolt to avoid leak points. Once sealed, the chamber must be baked for 1-2 weeks depending on the number of times the chamber or components have been previously baked. Our baking temperature is limited to 165°C due to the solder on the filter board, which is at risk of re-flowing at higher temperatures. Baking is done using a custom insulated baking tent that fits around the chamber and is fitted with large heaters.

After a bake, the Ti-sub is fired for 60 s at 50 A, which heats a Ti source and sublimates Ti so that is coats the inside surfaces of the vacuum chamber. The Ti atoms are reactive, and background gases will 'stick' to the freshly deposited layer of Ti. The Ti-sub needs to be re-fired after any contamination of the vacuum or sometimes after long periods of UHV operation. We observe that the Ti-sub does deposit some Ti on the top of the trap surface.

As previously discussed in Chapter 2, surface traps suffer from low trap depths, and collisions with background gas may knock an ion out of the trap. Therefore, ion lifetimes in our system are highly sensitive to elevated pressures in the chamber. For a pressure of around 2×10^{-9} torr, we observe ion lifetimes of about two minutes. During several iterations of baking and trapping over the > 5 year usage of the chamber, the ion lifetimes declined and it became clear that the ion lifetimes were not long enough for measurements of any kind.

Due to the number of vacuum components that are on the chamber, it was not clear which one could be contaminating the vacuum. A leak test was performed by monitoring the RGA and blowing helium around all of the flanges. No helium was observed entering the chamber, so the bad vacuum must have been from something inside that was outgassing. To find it, we removed suspicious pieces of equipment from the chamber, baked, and checked the pressure. This process, and the pressures measured are summarized in Fig. 4.2. There was a gate valve on the chamber for the turbo pump that had been present since it's first construction and bake. The gate valve was not all metal, but in fact had a Viton seal (an organic material). Its minimum pressure specification was only 10^{-10} torr. We believe this was the source of our vacuum issues, since once removed, the pressure decreased to lower than the previous values. It is also important to note that at the same time, an IR window was removed that had residue and discoloratoin inside that may have been from baking at temperatures higher than the windows specifications, which are unknown. After re-installing components necessary for ion trapping and surface science, the pressure remained low and ion lifetimes were improved to many hours. Under these conditions, we find that at room temperature the achievable pressure is less than 10^{-11} torr.

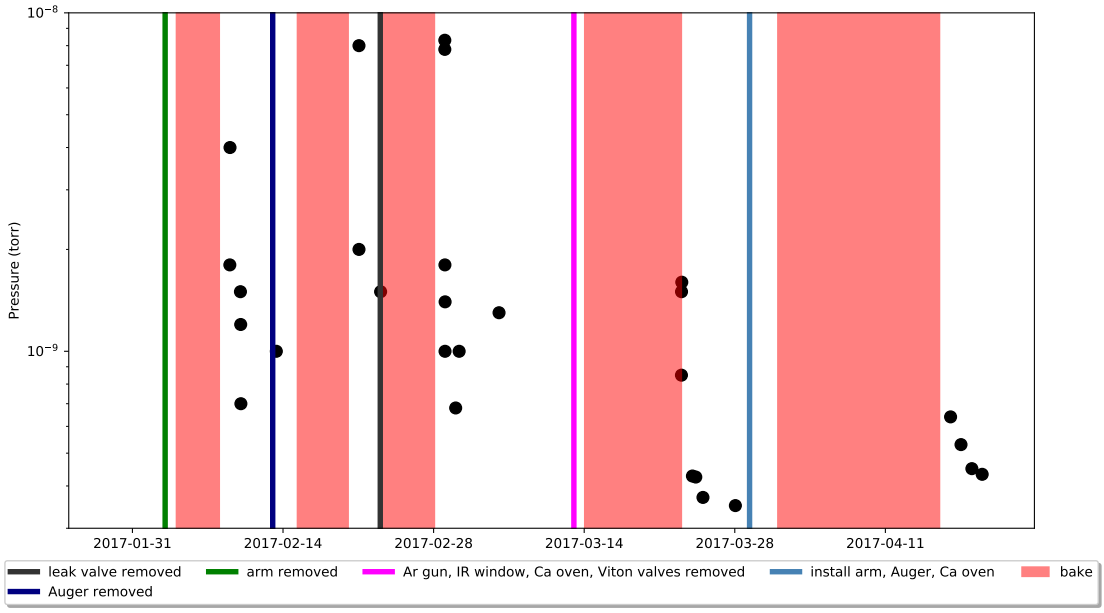

Figure 4.2: Summary of the pressure during the process of searching for the vacuum component limiting the achieveable pressure. The black data points show the pressure measured with the RGA at various times indicated by the date in the format year-month-day. Red regions indicate that a bake occurred. Each vertical line indicates the removal or re-installation of one or more components of the chamber as labelled. After each bake, the ion pump is turned on and the Ti-sub is fired, resulting in a decrease of the pressure. However, after about one day, the pressure increases back to the level of 10^{-9} torr. Finally, after the removal of several items including the Viton valves (indicated by the pink line), the pressure decreased significantly. The manipulation arm with the trap, the Auger, and the oven were reinstalled and the pressure stayed low. After this process, with several runs of the Ti-sub, the pressure reached levels unmeasurable by the RGA ($< 10^{-11}$ torr).

4.3 Trap

To study surface noise, we use a trap with a trapped ion height (72 μm) that is low enough to be sensitive to the noise, but not so low that the heating rates are too high to measure reliably. It is a simple linear design that has a large usable trapping region in case a portion of the trap or electrode connections are damaged.

The trap is a basic single metal layer design. The electrode pattern is fabricated onto a 500 nm thick fused silica substrate by Translume using laser ablation; the pattern is shown shown in Fig. 4.3a, with a view zoomed into the trapping region in Fig. 4.3b. The gap between electrodes is 20 μm, which is large to avoid metal deposits during ion milling that could create unwanted electrical connections. Metal is evaporated onto the top surface of the trap in the UC Berkeley Marvell Nanofabrication Laboratory using e-beam evaporation. First, a titanium sticking layer of about 10 nm is evaporated to assist in the adhesion of the metal to the surface. Second, about 500 nm of aluminum is evaporated and then on top, 30 nm of copper. There are more details about the properties of this specific metal mixture in Chapter 5. The evaporation is done at an angle of 30° to the surface. The shallow angle prevents metal deposition in the bottom of the trench that would connect neighboring electrodes. The evaporation is repeated with the trap rotated 180° about an axis perpendicular to the top surface to coat both sides of the trench. The small amount of metal down the trench sidewall shields the ion from the insulating glass substrate. The trench dimensions and evaporation results are shown in Fig. 4.3c. An optical image of the trapping region after evaporation is shown in Fig. 4.3b.

The trap design is a simple linear Paul trap made for trapping at $\approx$ 72 μm from the surface. In this trap, referred to as the H-trap, the RF electrodes are asymmetric (65 μm and 80 μm wide, with a 65 μm wide center electrode between them), which creates rotated principal trapping axes with respect to the symmetrically applied DC voltages.. This asymmetry allows for the possibility of rotating the axes further using a DC-bias on the RF electrodes. Simulations show that with 100-200 V amplitude on the RF electrodes, radial trap frequencies of 3-6 MHz can be reached. There are 10 DC electrodes on either side of the trap that are used for tuning the axial potential. Trapping is possible above anywhere along the center of the center electrode.

The trap is electrically connected via wire bonds to the chip carrier (CLCC) with 600 pF capacitors. The CLCC is made of Macor and topped with gold bond pads. Figure 4.4a shows the trap and CLCC after wirebonding. The assembly is then placed into a ceramic socket attached to the filter board (described in Section 4.5). Fuzz Buttons® (Custom Interconnects) are gold springs capped with flat tops which, when compressed, provide a reliable and low-resistance ($< 1\ \Omega$) electrical connection. They are used in the socket to make the electrical connections from the CLCC to the board below.

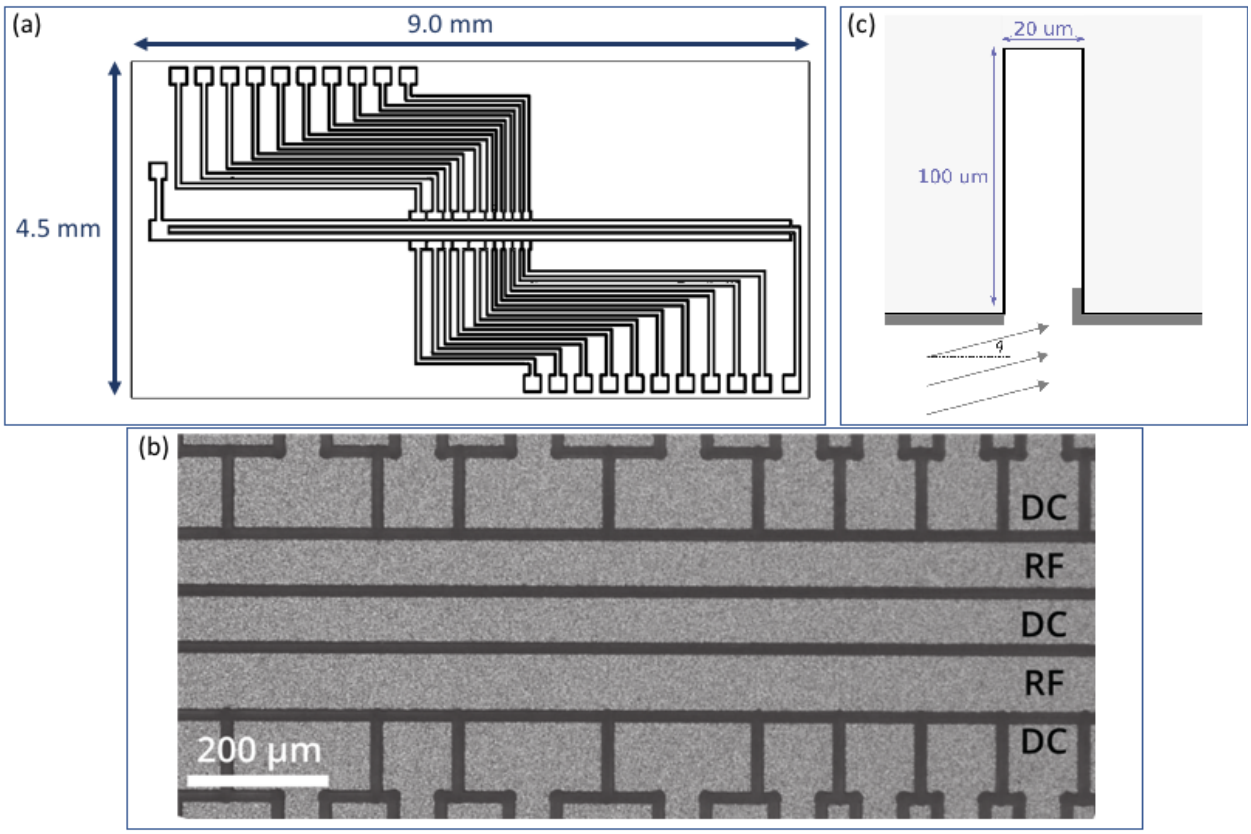

Figure 4.3: (a) H-trap design with wirebonding pads on the edges of the trap trip. The black traces are the trenches that electrically isolate the electrodes after evaporation of metal. (b) Grey-scale optical microscope image of the trap surface prior to vacuum-installation. (c) Cross-section schematic of a trap trench during evaporation of metal from below. Arrows indicate the direction of e-beam evaporated metal at an angle $\theta = 30°$ to the surface. The evaporation coats the top surface of the trap as shown, without landing in the bottom of the trench. The process is repeated at 180° around an axis perpendicular to the top surface, or equivalently at an angle of $\theta = -30°$ to the surface.

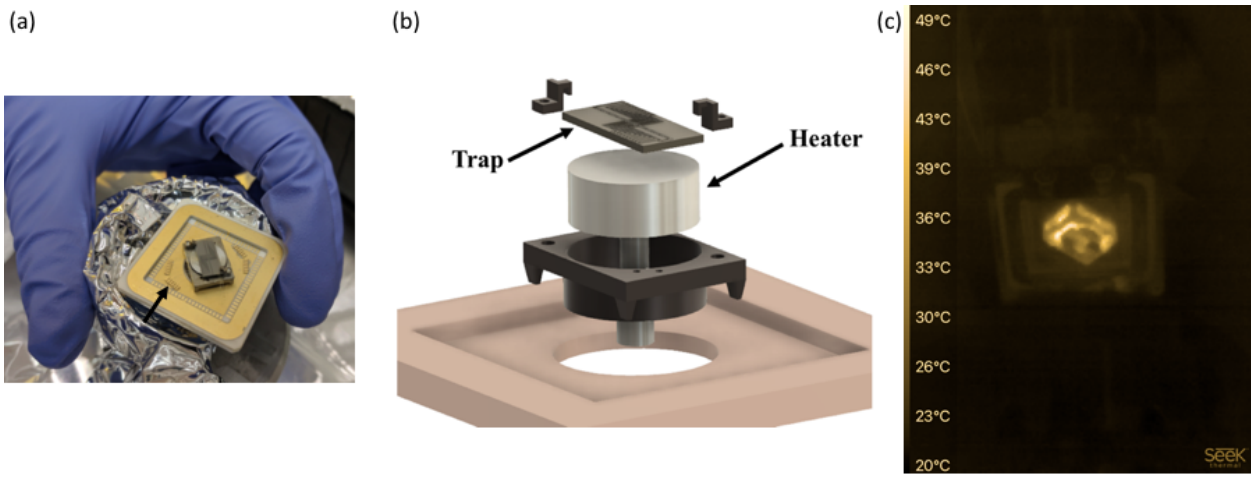

Figure 4.4: (a) Top view of the assembled trap and heater before wirebonding. The small black arrow points to the 600 pF through capacitors soldered to the CLCC. (b) Exploded view of the heater assembly. The trap is clamped directly onto the button heater with the two small stainless steel clamps that are screwed into the stainless steel holder below. (c) A thermal image showing that the heater and trap are thermally isolated from the rest of the assembly

4.4 Heater

The trap is directly mounted onto a button heater as shown in Fig. 4.4(a-b). The heater is manufactured by HeatWave Labs (101136 0.320" 1200^{o}C UHV Button Heater) and is made of an alumina core with a molybdenum outer shell. The heater is attached to the CLCC via a small screw making contact with the stem (see Fig. 4.5 for details). The design isolates the elevated temperatures to the heater and the trap alone, as confirmed by thermal images (example in Fig 4.4c).

Monitoring the heater for shorts to ground and connectivity requires a 4-wire measurement due to the low value of the resistance of the heater itself (0.4 Ω at room temperature). The ground lead (Fig. 4.5c) is connected to trap ground via the stainless steal mount that contacts the CLCC. The heater lead (Fig. 4.5a) goes directly into the ceramic inside the heater, and we use a hollow cylindrical piece of Macor ceramic to isolate that wire from ground (Fig. 4.5(d)). With two wires connected to each lead, and sent out through vacuum feedthroughs, a 4-wire measurement is possible to determine the resistance of the heater. During operation, we monitor the resistance and current to determine how the heater behavior changes from one measurement to the next.

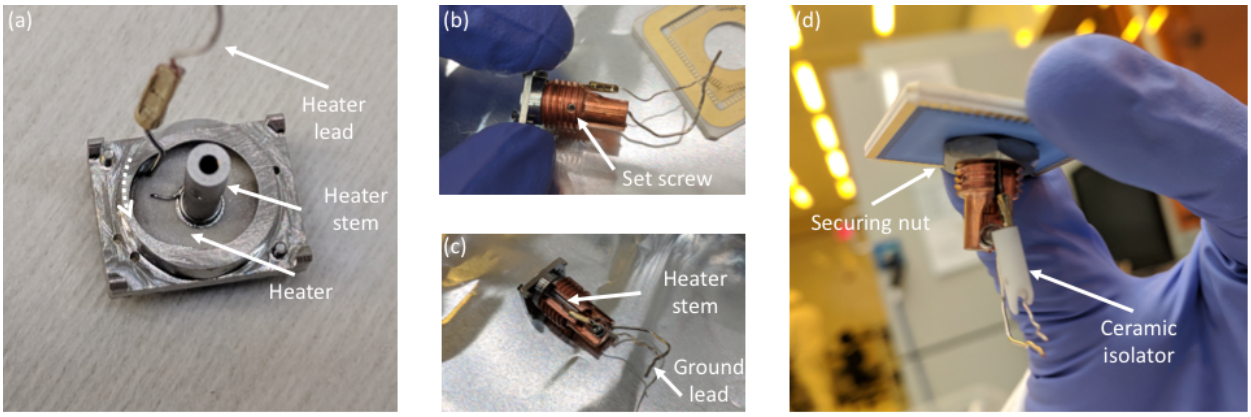

Figure 4.5: Several different views of the heater assembly (a) The hole in the stainless steel holder for the heater is asymmetric, so it is necessary to rotate the heater until the heater lead is in the augmented part of the hole before attaching the copper heat sink. This ensures electrical isolation between the heater lead and the stainless steel holder. (b) A set screw on either side is screwed into the heat sink until it makes contact with the heater stem, which secures the heater to the heat sink. (c) The heater stem serves as the ground connection via the set screws and the ground lead attached to the copper heat sink. (d) The securing nut is screwed onto the copper heat sink, creating pressure between the stainless steel holder on top of the CLCC and the nut, which secures the assembly to the CLCC. The ceramic isolator is pushed into the copper heat sink and ensures electrical isolation of the heater lead.

4.5 Electronics

A schematic overview of the setup is presented in Fig. 4.6 including the electronics, vacuum chamber, and Faraday cage. To avoid ground loops or any noisy or faulty ground connections, special attention is paid to the grounding of each component. The chamber is only directly connected to ground due to the ion pump connection via the power strip. The signal generator is grounded to improve impedance matching of the RF resonator (Sec. 4.5). The only direct ground connection to the wall inside the Faraday cage is through commericial EMI filters. Finally, the DC voltage source (DAC) has a ground connection via the USB cable to the computer.

To set the Zeeman splitting of the energy levels of the ion, we use magnetic field generating coils. The coils are on opposite sides of the chamber in a Helmholtz configuration and aligned perpendicular to the axial trap direction. A current of 2 A corresponds to about 2 G at the center of the trap. When the heater is in use, the magnetic field from the nearby current changes the magnitude and direction of the magnetic field at the ion by up to 0.5 G. This change must be monitored during measurements to correctly calculate the Zeeman splitting and frequency of the carrier. We find that the field produced by the heater is very stable, and causes no detectable additional dephasing due to magnetic field noise. We also observe

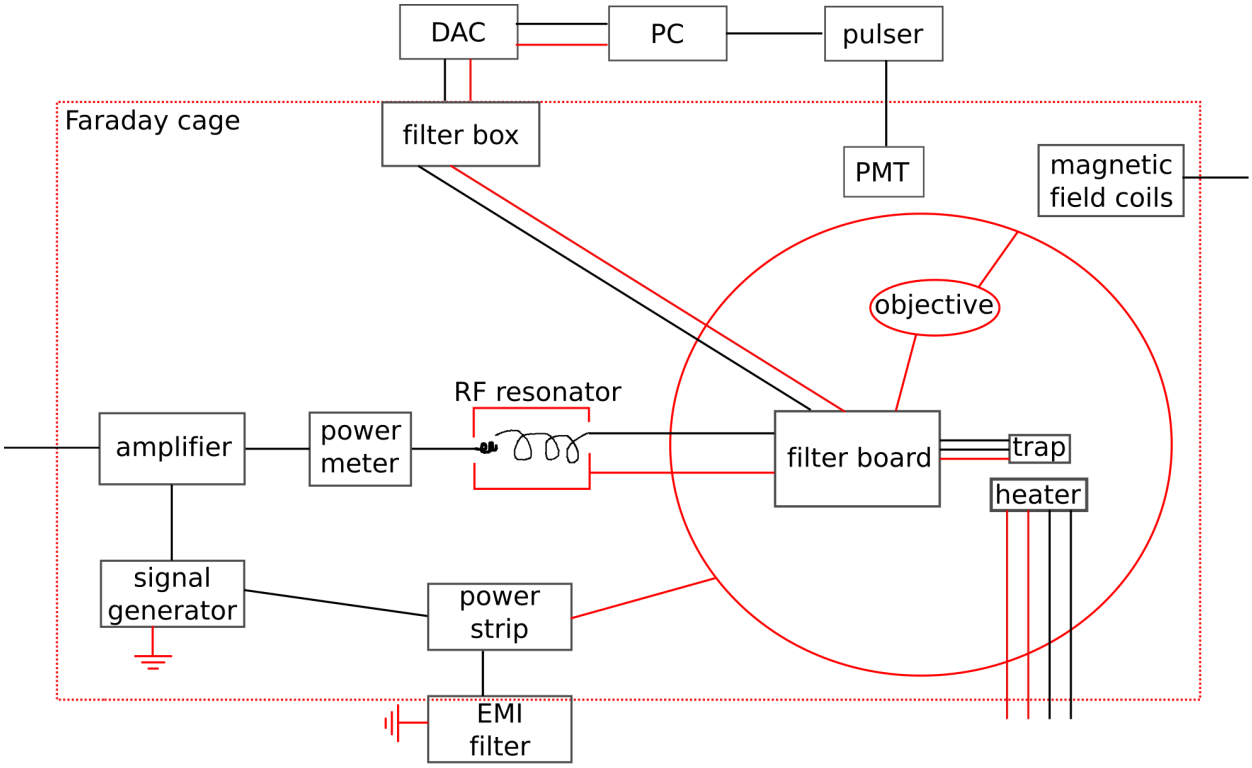

Figure 4.6: Schematic of the electrical components and their connections. A black line is a wire that is not ground. The red lines indicate a connection to ground as defined by the surface of the optical table and the wall. The large grounded circle is the vacuum chamber and any wires that cross the boundary are isolated from the chamber with a vacuum feedthrough. Any wires that cross the Faraday cage wall are filtered using common-mode choke filters (Sec. 4.5, Fig. 4.9). Details of the filter board, DAC, filter box, and EMI filter are in Sec. 4.5. The trap is detailed in Sec. 4.3.

that the long term stability of the magnetic field is similar to the stability of the field from the Helmholtz coils, with variations of up to a fraction of a mG in the span of minutes.

DAC

The heating rates measured in this dissertation are along the axial mode of motion, whose confinement is set by DC voltages applied directly to the trap electrodes. It is necessary to use low-noise voltage sources that can be readily changed for adjusting the trap frequency and achieving micromotion compensation. We use a custom built digital to analog converter (DAC) to supply these voltages that is located outside of the Faraday cage to avoid radiofrequency pickup from the trap RF drive. The DAC can be programmed via an Opal Kelly FPGA to assign voltages via 28 AD660 DAC chips with outputs from -10 V to +10 V. Noise

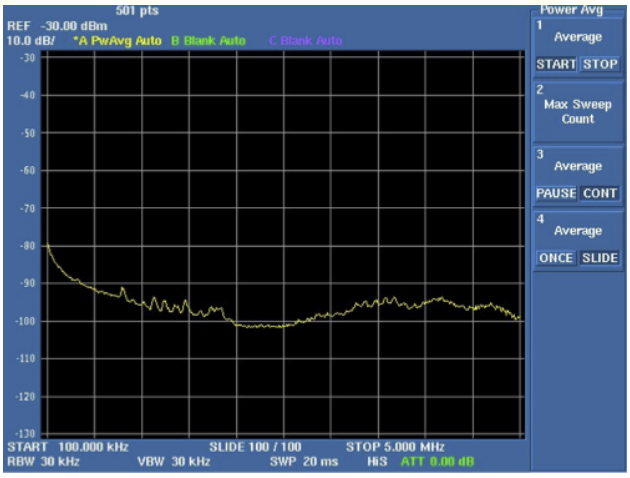

Figure 4.7: Sample spectrum analyzer measurement of the voltage noise from the DAC showing inputted noise below -90 dBm/Hz around 1 MHz before any additional filtering.

measured at DAC outputs on a spectrum analyzer was below -90 dBm/Hz around 1 MHz as shown in Fig. 4.7 for the noisiest output observed.

Filtering

To block electromagnetic interference (EMI) from the environment, the entire vacuum chamber is enclosed in a Faraday cage constructed from 1.25 mm thick aluminum walls. Any conducting wire entering the chamber is low-pass filtered at the cage wall, excluding the PMT signal, which needs to be fast for the TTL pulse that signals the ion detection. Power for the signal generator and the ion pump is provided through a commercial EMI power line filter (FN2010B-30-08) with at least 30 dB of attenuation at 1 MHz that connects to a power-strip in the cage (Fig. 4.6). The trap DC voltages are filtered in several stages before the voltages reach the trap. The DAC outputs are connected to a filter box at the Faraday cage wall with four stages of RC filters whose circuit diagram is shown in Fig. 4.8a. The voltages then enter vacuum and are filtered once again by an in-vacuum single-stage of RC filter. There are two capacitors, one for the low-frequency cutoff and the other to filter the noise from the first capacitor (Fig. 4.8b). Finally, there are 600 pF capacitors soldered on the chip carrier that are wirebonded directly to the trap.

All other conducting lines entering the chamber are filtered using common mode choke with high magnetic permeability toroids as shown in Fig. 4.9 along with several sample measurements of the filter function. They work by rejecting any common mode signals in the toroid due to the high permeability of the material, which create a low-pass filter.

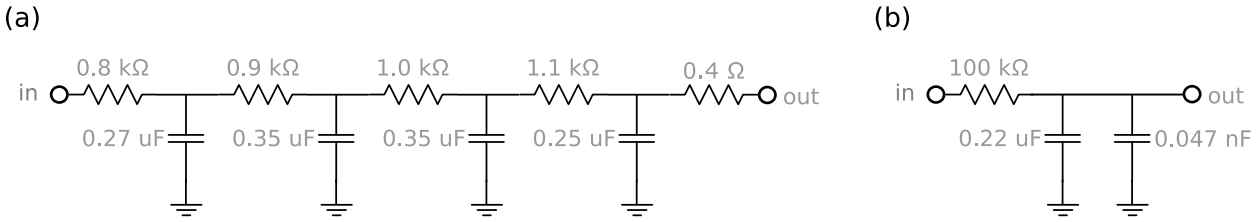

Figure 4.8: (a) Four-stage RC filter in the filter box for trap DC voltages; located at the Faraday cage wall. (b) Single stage in-vacuum filter for trap DC voltages

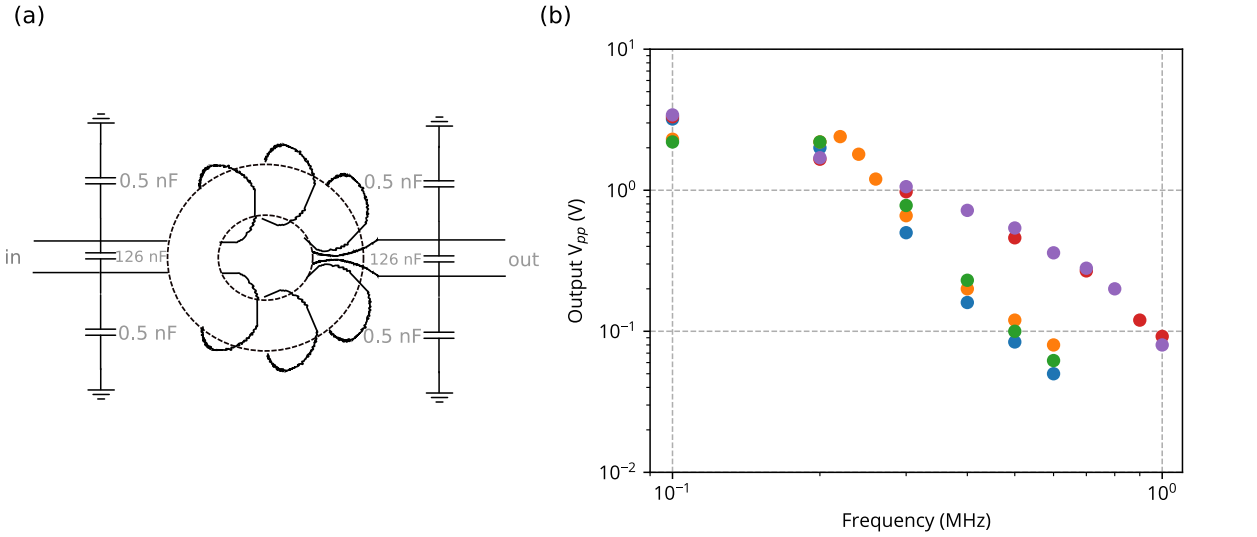

Figure 4.9: (a) Circuit diagram for common mode choke filter used for conducting wires entering the Faraday cage. The toroid is a high magnetic permeability material, and the windings directed are such that only common mode (low frequency) signals are permitted. (b) Measured filter function of several different choke filters used, which may have slightly different filter functions depending on the quality of construction. In this test, the input voltage was 10 V_{pp}.

Radiofrequency resonator

Since the trap is a capacitive load, it is necessary to use an impedance-matched circuit to provide a high-voltage alternating signal with low power dissipation on the trap. The trap itself is about 2 pF, but with the long wires connecting the trap to the feed-through the capacitance is closer to 30 pF. The RF resonator that allows for impedance matched transfer of power consists of a copper coil inside a copper can. The coil wire is a refrigerator coil that is several millimeters thick and coiled into about five turns. The resonance of the coil with a 30 pF capacitor is 100 MHz. When connected to the trap, the resonance is 35 MHz due to the large inductance of the wires leading to the trap in vacuum along the manipulation arm. The resonator is inductively coupled using a small coil of copper wire in the copper can that is isolated from the rest of the resonator. The can is then housed inside an aluminum box to reduce the radiated power.

The signal generator used for the RF voltage is a Rohde and Schwarz, with a 5 W amplifier and a power meter for monitoring reflected power and calibrating impedance matching. The signal generator is connected through a power meter to the inducer coil. Details of the connections, including the grounding and isolation are shown in Fig. 4.6. The output impedance of the resonator should match the impedance of the long wires and trap for maximum power transmission to the trap. In practice, the inductor coil and the lengths of the connecting BNC cables can be adjusted to achieve a minimal reflection of power, measured on the power meter as standing-wave ratio (SWR), ideally between 1.1 and 1.5.

4.6 Lasers

There are six different lasers used for trapping and manipulating $^{40}Ca^{+}$. Details of the laser setup including the layout in the lab are available in the thesis by T. Pruttivarasin [46]. Every laser we use is a diode laser. Excluding the 375 nm and 729 nm lasers, all the lasers are locked using the Pound-Drever-Hall (PDH) scheme to a reference cavity with piezo-tunability. The 397 nm (422 nm) light is doubled from a 794 nm (844 nm) source in a bow-tie cavity. The most stable cavity is for the 729 nm laser, which is used as the frequency reference for the wavemeter. The 729 nm laser is locked via a double injection procedure as outlined in the thesis by D.J. Gorman [47] and amplified in a custom built tampered amplifier to several hundred mW of light. The two lasers needed for photoionization provide light at 375 nm and 422 nm. All of the lasers are located in a separate room from the experiment, providing some thermal stability compared to the main lab space, and brought to the experimental optical table via long optical fibers.

On the experimental optical table, the cooling and manipulation lasers (not photoionization) are routed through acousto-optic modulators (AOMs). Each beam goes through an AOM double-pass to control the power and frequency of the beam before it is coupled to an optical fiber that leads to the chamber [46]. The AOMs are driven with RF signals that are amplified to provide the power needed. The 'pulser' is the electronic circuit that programs

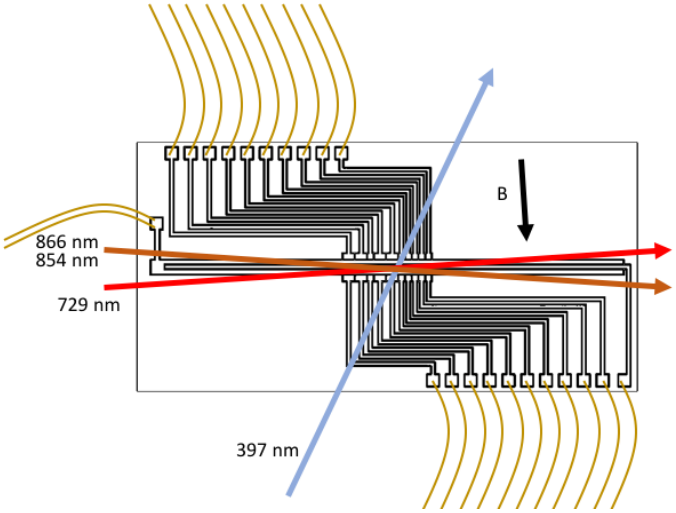

Figure 4.10: Layout of the laser beams above the trap surface. The 729 nm beam is aligned $\approx 11°$ from the trap center axis and perpendicular to the magnetic field (B). The Doppler cooling 397 nm is aligned to have a projection on the two trap axes parallel to the surface.

and runs the DDS boards and details of that are in the thesis by T. Pruttivarasin [46].

Each beam is aligned over the trap surface with a collimator mounted on two translation stages. The layout of the lasers on the trap surface is depicted in Fig. 4.10. The Doppler cooling 397 nm beam has a projection on all three axes, with the smallest projection on the vertical axis. The 729 nm beam is aligned as close to parallel to the axial mode of motion as possible while avoiding the RF wirebonds in the beam path.

4.7 Imaging

Optical

The objective used for imaging is mounted into a bellow with a viewport on the end. The bellow extends the location of viewport further into the vacuum chamber and closer to the trap. By stretching and compressing the bellow, the objective can be moved up and down in vacuum not only for improving imaging, but also to clear the field of view of the trap from other angles. A 90:10 pellicle mirror splits the light between the PMT and the camera, respectively. Ions are detected using a photo-multiplier tube (PMT) that is positioned at the image plane corresponding to about 70 μm above the trap. The camera can be used for imaging ions as well, but is not used for detection during experiments, only initial trap and laser alignment.

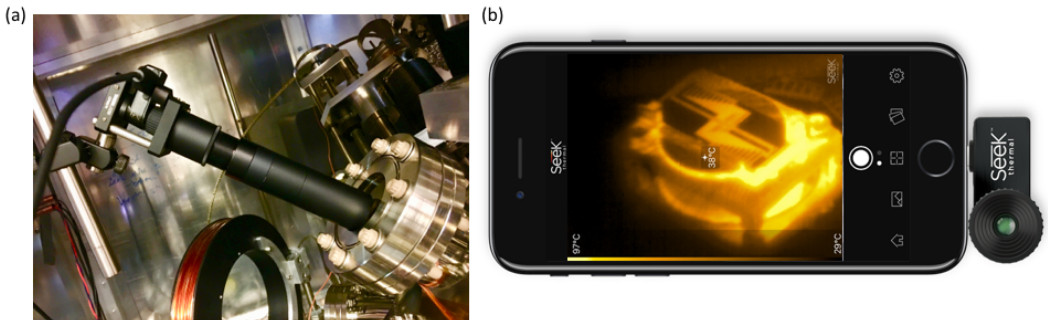

Figure 4.11: (a) Thermal camera is shown mounted outside the vacuum chamber. The black tube contains several ZnSe lenses in a telescope configuration for increased zoom. The vacuum window is an IR-transmitting ZnSe window. (b) Sample thermal image of the trap and heater in vacuum, and illustration of the camera connection to an iPhone. The temperature scale bar must be calibrated for losses through the lenses and window, as well as emissivity (see Chapter 5).

Thermal

A Seek Thermal, model CompactXR, camera is used for thermal imaging of the trap and temperature calibration. It is mounted outside the vacuum chamber with a view of the trap through a special infrared-transmitting window made of ZnSe. Several ZnSe lenses can also be used to increase the zoom. See Fig. 4.11 for setup details and a sample photo with increased zoom. Details of the calibration are in Chapter 5.

Chapter 5

The heater: possible high-temperature effects and temperature calibration

With an *in situ* heater capable of achieving temperatures upwards of 1000°C, there are several possibilities for interesting heat-induced effects to consider. The surface of the trap is known to have some non-metal contaminants such as carbon-based molecules. These molecules could desorb from the surface if the temperature of the trap becomes high enough to overcome the binding energy. Annealing the metal of the trap electrodes is also a possibility, and in this chapter we explore the micro-structural changes of different Al-Cu compositions. Finally, we also aim to measure electric-field noise while the heater is in operation, and here we describe the calibration of the trap temperature during those measurements.

5.1 Desorption

At elevated temperatures, some compounds will begin to desorb from the surfaces of metals. This process, along with the diffusion from the bulk to the surface, is what is used to lower the attainable pressure in the vacuum chamber. It is possible that by heating the trap, we might desorb some compounds and change the surface environment, and thereby the electric-field noise.

Our collaborators at Lawerence Livermore National Laboratories, Keith Ray and Vincenzo Lordi, shared with us some calculations of the residence time of various carbon-based molecules on a gold surface. The residence time is defined by the average time a molecule will stay on a surface before the thermal energy is enough to overcome the binding energy and release it. They calculate the binding energy from first principles [48] and then apply the Arrhenius rate equation to determine the average residence time [49]. While the general consensus is that carbon and oxygen compounds are the main contaminants on surface traps [30, 50], what is not known in what molecular form they may be bound to the surface. Fur-

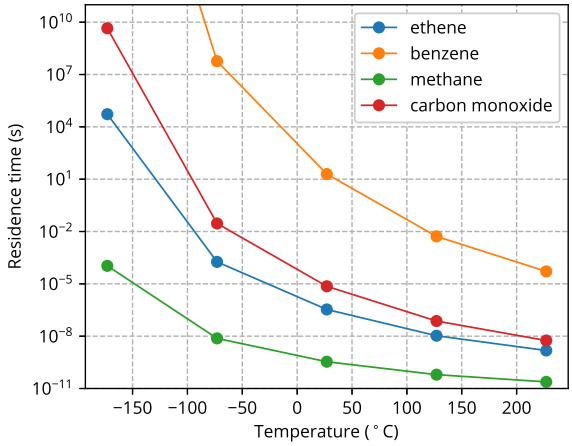

Figure 5.1: Residence time for various non-covalently bound carbon-based contaminants on gold based on calculations by collaborators at LLNL.

ther, depending on how a particular molecular compound or atom binds to the surface, the desorption will happen at a different temperature. According to their calculations, shown in Fig. 5.1, non-covalently bound species such as carbon monoxide and methane will not stick well to the surface even at room temperature. Benzene may undergo a desorption process during the trap baking procedure, when temperatures reach higher than 100°C. There may also be larger hydrocarbon molecules with more van der Waals interactions with the surface that result in a higher binding energy and a higher temperature desorption process. It is likely that after baking the chamber and trap at upwards of 150°C for two weeks, most of these molecules would have been removed from the surface and therefore are not a factor in the heating rates studied here. Strongly-bound species would not desorb until much higher temperatures (400-500°C), which have not yet been reached in this experiment. As discussed in the next section, it may be possible to reach above 400°C without significant trap damage or microstructure changes.

Monitoring the background gas in the chamber as the trap heats might reveal what types of bonds the contaminants make with the metal surface. As of the measurements presented in this thesis, no observable background gas is present with the heater on, but the ion lifetimes do shorten at higher temperatures. Shortened lifetimes are most likely caused by background gas collisions that either knock the ion out of the trap or form molecular compounds with the ion. This observation suggests that during these particular measurements, the pressure was elevated near the ion, even though it was not detectable in the larger chamber. While desorption has yet to play a dominant role in the noise measurements presented in this work, it is possible that it may become an important factor as the temperature is increased.

5.2 Annealing

One relatively unexplored aspect of electric-field noise in ion traps is the role of the structure of the metal surface. In order to explore this, it is ideal to have a trap that has a surface structure that can be deterministically changed *in situ*. For example, a change in the average grain size could illuminate the role of grain boundaries in the noise. A grain in a polycrystalline metal is a region of the metal that has the same crystal structure or packing arrangement of atoms. Grain boundaries exist where grains with different orientations or structures meet. If a metal has smaller grains, then it will have more dense grain boundaries.

The combination of Al and Cu, when prepared in the correct ratio, is a material that can be heated and cooled under certain conditions to create this effect of *in situ* changing grain structures. The phase diagram for this system is shown in Fig. 5.2a. With low concentrations of Cu, indicated by the percentage by weight (wt%), added into the Al matrix, there are two possible solid phases. The α phase is solid and Al-rich, whereas the θ phase is solid $CuAl_2$. With a concentration of 5.65-52.5 wt% Cu, when the solid solution is heated above 548°C, it will begin to melt. However, for < 5.65 wt% Cu, the solution will remain solid and undergo a phase transition into the α phase at higher temperatures. This behavior of having a phase transition without melting the metal is a process that might be achieved *in situ* with an ion trap. In particular, the process would not lead to melting of the trap electrodes that would cause unwanted metal flow into the trench boundaries between electrodes. It would be interesting to study the effect of such a phase transition on the electric-field noise detected by a trapped ion. These types of measurements might reveal the role that the structure of the metal plays in the 'anomalous heating' instead of focusing solely on adatoms as previous proposed models and studies have done.

In the context of the work presented in this thesis, there are two different Al-Cu mixtures to discuss. The first is the current mixture used for the trap electrodes, which is 14 wt% Cu. This mixture is not designed to have a solid state phase transition, but we explore its properties to anticipate possible effects during heater operation. The results of *ex situ* annealing tests are summarized in the following section, showing that significant changes to the structure will likely only occur at temperatures near the melting point. The second mixture is one that is less than 5.65 wt%, which means that it should undergo a solid state phase transition. In the following section, we specifically outline the behavior of a 4 wt% sample and postulate that creating such a trap might allow exploration of this phase transition in situ.

It is also important to note that even though our traps are fabricated by evaporating aluminum and then adding a layer of copper on top, the baking process to achieve high vacuum (Sec. 4.2) will keep the sample at 165°C for several days, allowing the copper to diffuse randomly, but non-uniformly, into the aluminum. We have observed evidence of this process in the changing color of the trap from copper colored to gray after baking.

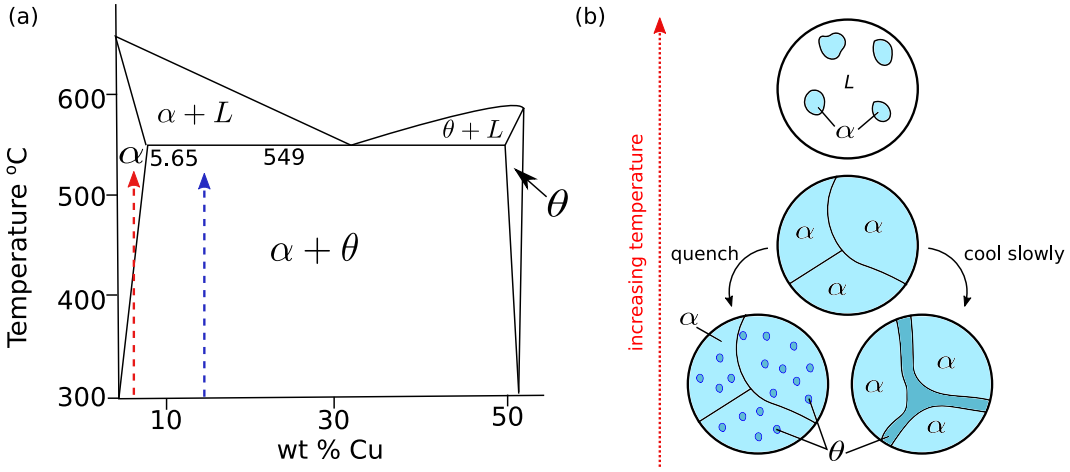

Figure 5.2: (a) Phase diagram for a solution that is primarily Al, with the wt%Cu added as indicated on the x-axis. The solid lines indicate a phase transition in the material. The α phase is solid and Al-rich, whereas the θ phase is solid $CuAl_2$. L indicates a liquid phase. The red arrow traces at 4 wt% sample, showing that it stays solid up to above 550°C, unlike the 14 wt% sample (blue arrow), which would melt about the eutectic at 549°C. (b) An illustration of the 4 wt% material behavior (red arrow from (a) extended above 600°C). If the solution is cooled slowly over several hours from above the phase transition (around 400°), then large θ phase regions separate the different α grains. If the sample is instead quenched to room temperature, a more uniform distribution of small clusters of θ phase will precipitate. [Adapted from "Precipitation Hardening" by H.K. Khaira] [51]

Current trap composition

The trap that was used for the electric-field noise measurements presented in this thesis is mainly Al, with 14 wt%Cu. The phase diagram in Fig. 5.2 shows that we expect this mixture to have mixed α and θ phases and melt above 550°C. Annealing tests were performed to evaluate the effects of heating a 14 wt%Cu sample to determine the possible effects of heating the trap that is in use.

We collaborated with several students of Professor Zettle at UCB for these annealing tests. The tests consisted of taking a trap sample, annealing under vacuum, and viewing the sample with a Scanning Electron Microscope (SEM). A trap that was fabricated with the same composition, but had been sitting in a plastic container in the clean room was used. Annealing was done in a glass tube at $\approx 10^{-8}$ torr in a programmable furnace. The recipe used was a 1 hour ramp-up/down to/from annealing temperature, which was maintained for 3 hours. First, a 150°C anneal was done to show what the typical trap conditions might be after baking to achieve UHV. Fig. 5.3a-c shows the SEM images of the trap surface after the first anneal. The structure is fine-grained and shows a few leftover skinny structures that were not present in freshly evaporated samples. It is probable that these structures

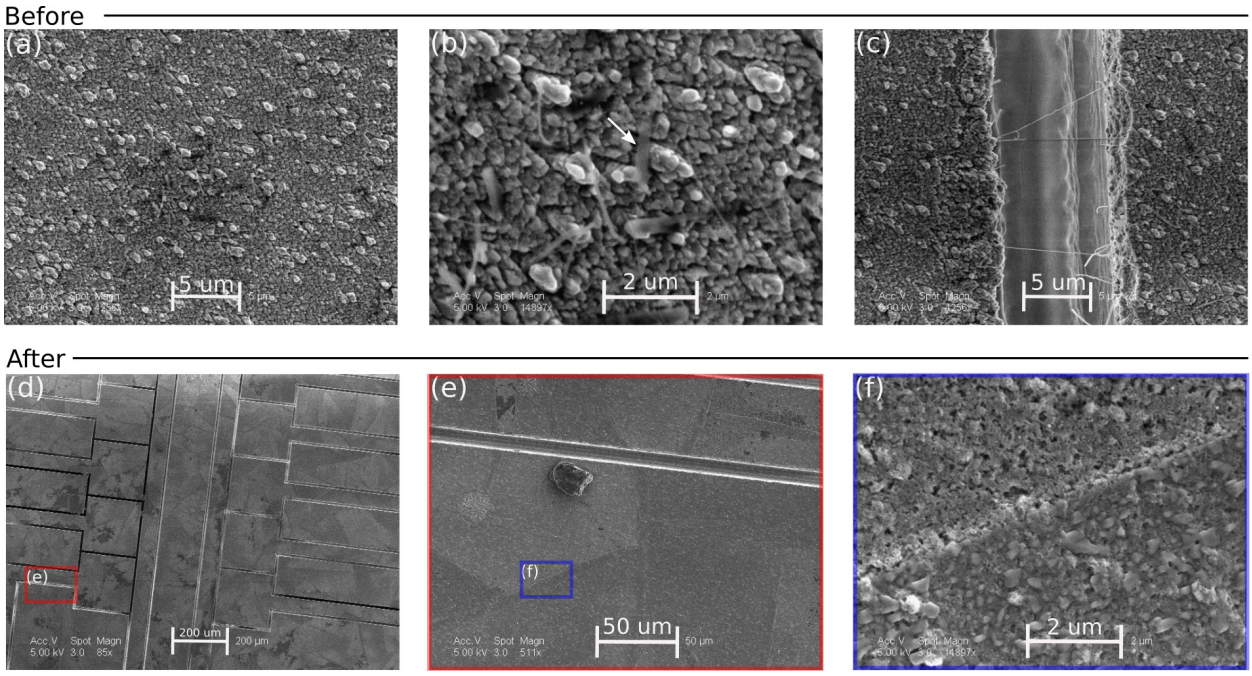

Figure 5.3: (a-c) Pre-annealing SEM images of the 14 wt% sample similar to the one used in this study. (a) This uniform fine grained structure was present on the whole trap surface. (b) Ribbon-like grains were only observed in aged traps, and were removed by a 200°C anneal (c) Whiskers were found in the trap trenches; also removed by a 200°C anneal (d-f) SEM images of the 14 wt% sample after a 600°C anneal (d) Large grains precipitated over the entire trap surface (e) The size of the grains was on the order of hundreds of μm^2 (f) An up close image of one of the large grain boundaries. SEM images taken by S. Matt Gilbert.

appear after the trap is aged at room temperature in ambient clean room conditions. These conditions were likely the same for the trap after the bake in vacuum.

We also observed an interesting phenomenon within the trenches in the aged traps. Fig. 5.3c shows whisker structures present in the trenches, which are unique to the aged samples. These whiskers were removed by annealing at 200°C, and do not appear in freshly evaporated samples.

After annealing at 200-550°C in steps of 50°C, there was no discernable change in the surface structure. However, once a 600°C anneal was done, larger grains began to form as shown in Fig. 5.3d-f that were hundreds of μm^2 in size and covered the entire trap surface. While this transition would be interesting to observe in vacuum, the trap suffered damage from the annealing process that would make trapping impossible as shown in Fig. 5.4. Due to the high temperatures necessary, it is not likely that this recipe will exhibit the formation of large grains without irreparable damage to the trap. Instead a lower wt%Cu sample should be used, such as the 4 wt% sample described in the next section.

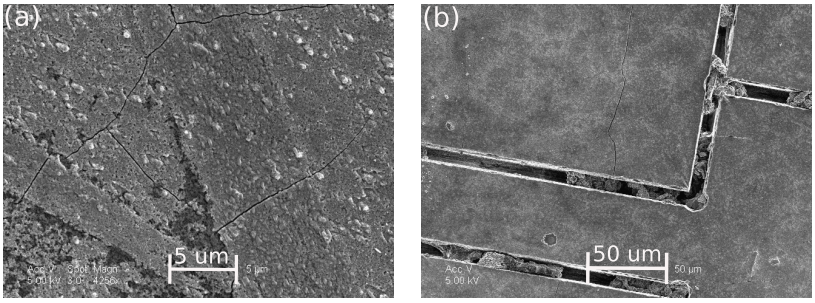

Figure 5.4: (a-b) Damage observed in 14 wt% samples annealed at 600°C including cracking and metal deposited into the trenches. SEM images taken by S. Matt Gilbert.

Achieving a phase transition in the solid state

We now explore the behavior of a sample that is 4 wt% Cu, which should undergo a phase transition in the solid state. While this does not apply to the trap used in this thesis, it is an interesting possibility for a future iteration.

A sample that is 4 wt% Cu, when heated to 550°C is a solid solution with copper atoms randomly mixed into the aluminum structure, with a single α phase of material (phase diagram in Fig. 5.2a). If it is cooled slowly, θ phase consisting of $CuAl_2$ will form large zones that may separate aluminum rich regions into grains [52]. See Fig. 5.2b for an illustration. In contrast to this behavior, if the sample is quenched, say into room temperature water, the copper atoms remain randomly diffused in the super-saturated solution. If the alloy is then aged, at a slightly elevated temperature (e.g. 150-200°C), the copper atoms will precipitate into small clusters called Guinier-Preston zones (GP zones). This process would leave a more uniform grain structure, with small clusters of Cu-rich regions throughout the material (see Fig. 5.2b). The difference in behavior is due to the fact that at elevated temperatures (> 300°C) vacancies are more mobile in the solution. If the material is cooled slowly, the large number of vacancies in the α phase will diffuse during the extended time at high temperatures to create the large regions of θ phase, leaving few vacancies at room temperature and a very stable structure. If the material is quenched into a supersaturated solution of copper atoms and vacancies, the diffusion happens during the aging process and reduced mobility causes clustering into smaller plates of less than 0.1 μm in size (GP zones). These plates are coherent with the aluminum lattice, but due to the size difference of the elements, cause a distortion of the lattice.

While rapidly quenching a sample in vacuum is a huge technical hurdle, slow cooling of the trap is easily implemented. If a trap is made with 4 wt% Cu, heated *in situ* to 550°C, then cooled over several hours to room temperature, it should be possible to create a dramatic change in grain structure that might influence the electric-field noise near the surface.

In order to explore the possibility of implementing such a process, we used the annealing procedure described in the last section to try and observe the phase transition. This test

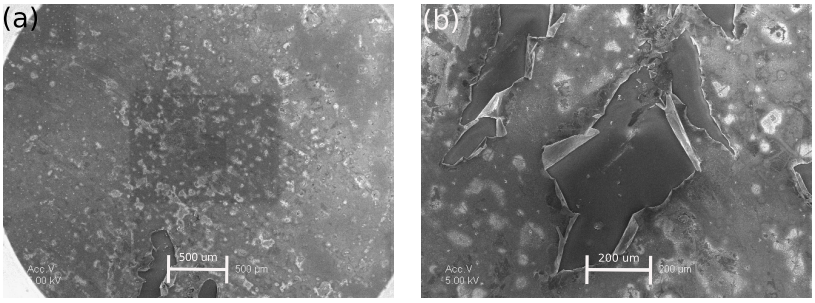

Figure 5.5: Damage and other odd behavior in a 4 wt% sample evaporated onto a glass slide instead of a fused silica trap substrate. (a) After starting with a smooth surface similar to other samples, we observe clumping of the metal (rectangles are an artifact of the microscope) (b) Peeling of the metal film on the large scale, unlike the fused silica samples. SEM images taken by Yasmeen Musthafa.

used two kinds of substrates, fused silica traps and glass slides, which were each evaporated with 4 wt% Cu. The same annealing procedure was used, with a final temperature of 600°C to ensure that the phase transition had been reached. It was determined that the samples on glass slides behaved qualitatively different than the fused silica samples, showing peeling and odd clumping (Fig. 5.5). In the trap samples, the metal bulged into the trenches in many locations and cracked across large areas (similar to the 14 wt% sample in Fig. 5.4). Fused silica samples are needed, and careful development of a process that is less destructive to the trap needs to be done before this process can be realized in vacuum.

5.3 Determining trap temperature in vacuum

The heater installed underneath the trap is a resistive heater, which means that electrical power is converted to heat. Power is also absorbed in the form of electromagnetic radiation from the environment at room temperature, which sets the lower limit of the temperature when zero electrical power is applied. The heat is then either conducted via contact between the heater and other objects or lost via electromagnetic radiation. In equilibrium, the power in, which is the sum of electrical power and absorbed radiation, must equal the power out. This balance determines the final temperature, T, that the heater can reach:

$$P_{\text{elec}} + \epsilon' \sigma T_0^4 = k'(T - T_0) + \epsilon' \sigma T^4 \tag{5.1}$$

where T_0 is room temperature, σ is the Stefan-Boltzmann constant, and $k' = kA/\Delta x$ is an adjusted conduction coefficient that depends on the surface area, A of contact and the thickness, Δx, of material between the heater and an object at room temperature. There may be many different points of heat conduction, resulting in k' that is actually a sum, $k' = \sum_i k_i A_i / \Delta x_i$. The radiation term is also modified as indicated by $\epsilon' = \sum_i \epsilon_i A_i$, since there may be several materials with different emissivity, ϵ_i and area, A_i. We first take

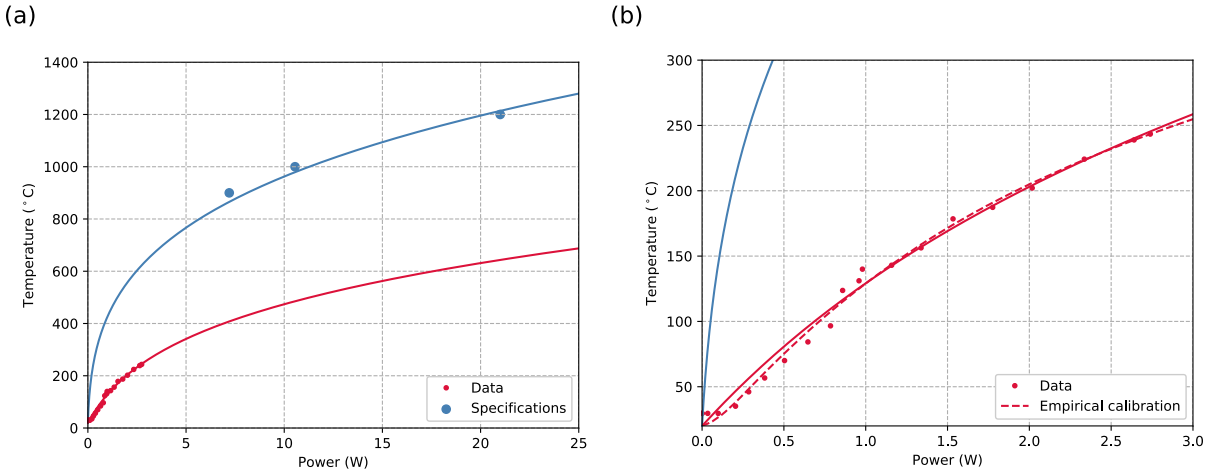

Figure 5.6: (a) Input electrical power vs. temperature of the heater at equilibrium. Blue dots are the specifications of the heater as provided by the manufacturer. Data taken during the calibration are shown as smaller red dots (zoomed into low powers to make visible in (b)). These data already have the correction applied for the camera and window as determined by Eqn. 5.3. Solid lines are fits to the conduction and radiation model, Eqn. 5.1. (b) Low power limit of the plot in (a). Dashed line is the accepted empirical calibration.

this simple model and fit the specifications for the heater to this model, using k' and ϵ' as the free parameters. We find $k' = 10^{-11}$ W/K and $\epsilon' \approx 10^{-5}$ m^2 provide the best fit to the specification data. Without an additional heat load, the heater is totally dominated by radiation, and the value of ϵ' is reasonable given the estimated emissivity ($\epsilon = 10^{-2}$ for molybdenum) and surface area ($A \approx 10^{-3}$ m^2) of the heater. The fit to this model of conduction and radiation is shown with the heater specifications in Fig. 5.6.

When the heater is installed in vacuum, the final temperature reached will depend on the way heat is conducted and radiated in the system. The first attempts to calibrate the final temperature used a thermocouple that was clamped onto a trap on top of the heater. It became clear that the heater behavior depended heavily on the placement and tightness of the clamp, changing the heat conduction, and making the calibration change from run to run. These type of calibrations would never result in an accurate estimate of the trap temperature in the absence of the thermocouple and clamp.

To successfully determine the temperature of the trap while the heater is in operation, we use thermal imaging. First, we discuss the calibration of the thermal camera. During the temperature scaling measurements presented in this thesis, the current applied and the voltage across the heater were monitored to determine the input electrical power. Afterwards, a calibration was done using the thermal camera to determine the actual temperature of the trap T_a based on the optical power recorded by the thermal camera. Later in this section, we compare the calibration to the model for heat conduction and radiation in Eqn. 5.1.

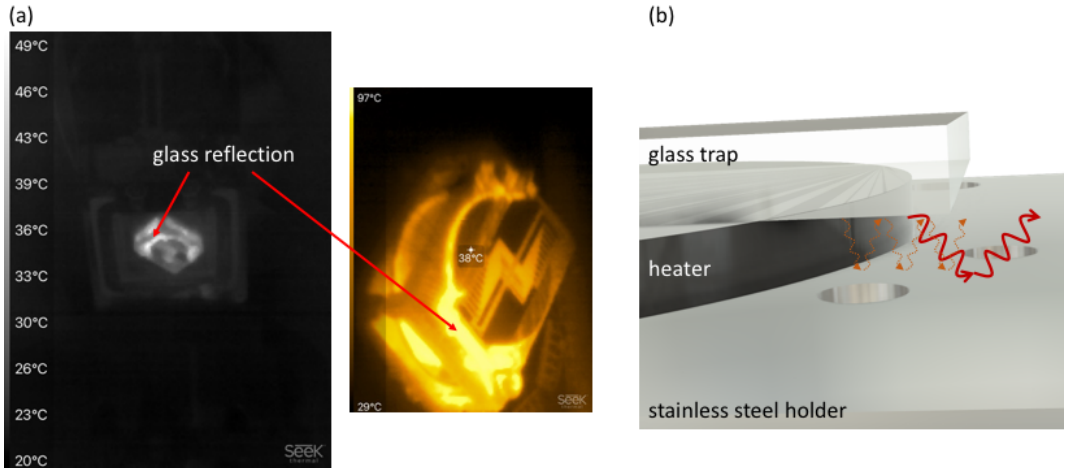

Figure 5.7: (a) The indicated bright areas in the thermal images of the trap in vacuum are a reflection of the thermal radiation from the bottom of the fused silica trap substrate in the stainless steel holder below. The temperatures measured at this location on the images were used for trap temperature calibration. (b) 3D rendering of the trap, heater and stainless steel holder with an illustration of the reflection of thermal radiation. The photons might reflect once off the metal below (thick red arrows) or bounce more times in the cavity created between the trap and the metal (dotted orange arrows).

Thermal camera

A thermal camera has a detector that detects thermal photons in the wavelength range of several microns. The Stefan-Boltzmann equation relates the power per area measured, j ,to the temperature T of the object being imaged:

$$j = \epsilon \sigma T^4,$$

where ϵ is the emissivity of the object. To use a thermal camera to image something inside a chamber, a window must be used that transmits infrared radiation relevant to objects at temperatures above 300 K. The window, in this case made of ZnSe, will attenuate some power, so that the total measured power is reduced by a factor $f < 1$:

$$j' = f \epsilon \sigma T^4. \tag{5.2}$$

This power measured by the camera is then converted in the camera software to a 'temperature' by solving Eqn. 5.2 for T and is displayed in units of °C. The attenuation by the window reduces j', and thereby the the displayed 'temperature', which we will refer to as T' with arbitrary units. Additionally, the camera does not accurately account for lower emissivity objects, and instead mostly assumes a black-body for everything. This inaccuracy means that the camera will read lower temperatures for low emissivity objects, such as a polished metal surface.

For these reasons, the thermal camera must be calibrated for measurements through the window and for objects whose emissivity is lower than one. Several different tests were done to see the systematic offset of the temperature using materials of reasonably known emissivities. The uncertainty in this correction for emissivity is the largest source of uncertainty in temperature in this work.

In particular, we calibrate for the emissivity of glass, since that is what is imaged in vacuum. An image of the trap in vacuum (Fig. 5.7a) shows a hot region on the edge of the trap, where highest measured temperatures were always recorded. This region is a reflection of the thermal radiation from the glass bottom of the trap by the stainless steel mount. As illustrated in Fig. 5.7b, the radiation may reflect many times, creating a cavity for thermal photons that closely resembles a black-body.

We calibrate the correction for emissivity and the window by placing a piece of glass on a hotplate and measuring with the thermal camera through an identical ZnSe window. The reference temperature was measured using a LaserGrip 630 model with similar sensors to the thermal camera, but no spatial resolution and a large spot size (22.5 mm). The LaserGrip showed agreement with the hotplate setting and thermocouples attached to the hotplate. When viewing the hotplate with the thermal camera, the high resolution revealed some hot and cold spots on the plate. The large spot size of the LaserGrip ensures that that once thermal equilibrium is reached with the sample, an average temperature is measured. The conversion for finding the actual temperature of the glass, T_a, is empirically determined to be

$$T' = \frac{T_a}{(1-0.678)e^{-\frac{T_a - 21^\circ\mathrm{C}}{18.24^\circ\mathrm{C}}} + 0.678} \tag{5.3}$$

when T' is displayed in °C. While we are confident in this conversion for a glass sample, the glass reflection that we use may not have the same emissivity. We can estimate the uncertainty in the temperature calibration by looking at the glass reflection radiation behavior. Figure 5.7b shows how the radiation from the glass bottom of the trap either reflects from the metal and out to the camera or bounces around between the glass and the metal. In the case of a single reflection, from the Stefan-Boltzmann law, the total radiated power is the combination of the reflected power and the radiated power from the metal itself:

$$P_{\mathrm{tot}} = \sigma\epsilon_g(1-\epsilon_m)T_g^4 + \sigma\epsilon_m T_m^4$$

where σ is the Stefan-Boltzmann constant, ϵ_g and T_g are the emissivity and temperature of the glass, and ϵ_m and T_m are the emissivity and temperature of the metal. Since the heater is resting in the metal holder, we can assume that the glass and metal are at the same temperature. Even a 5 K difference between them would be a very small $< 1\%$ uncertainty in the radiated power. Then the total power is proportional to $\epsilon_g + \epsilon_m(1-\epsilon_g)$. The second term is very small, and can be neglected so that the total power is just that of regular glass (.85-.95). With even more reflections, the glass and metal together create a cavity that radiates like a black-body with emissivity $\epsilon = 1$. For the final temperature calibration, we assume the emissivity from the calibration with glass. The uncertainty from the emissivity

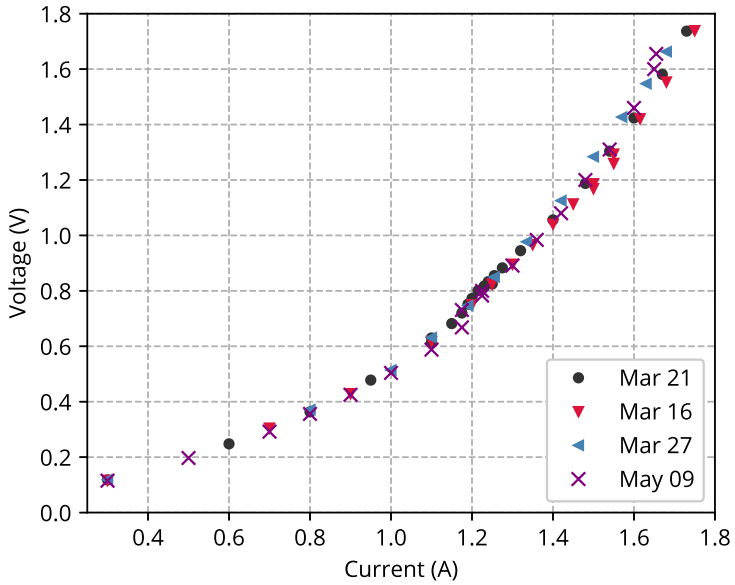

Figure 5.8: Recorded current applied to the heater and 4-wire measurements of the voltage across the heater. Points in March correspond to temperature scaling measurements reported in Chapter 6. The May data is from the calibration done after the IR window was installed.

(.85-1) is taken into account by assigning an uncertainty of ±10% in the actual difference to room temperature.

Calibration from power to actual temperature

Due to the late addition of the ZnSe window and the thermal camera, during the temperature scaling measurements presented in this work, only the power applied to the heater was recorded. After the window was added, a calibration was done to determine the relationship between input power to the heater and actual temperature. We are confident that the heater was behaving in the same way during the measurements and the subsequent calibration because of the consistency of the resistance under heating. The resistance of the heater depends on the final temperature reached, and it is quantifiable in a graph of current vs. voltage (IV-curve), whose slope is the resistance, as shown in Fig. 5.8. The consistent behavior of the heater between these runs shows that the heat load was likely the same, and the temperatures reached were the same (within any measurement uncertainties we already have).

During the calibration, we recorded current applied to the heater and the 4-wire voltage measured, which together determined the input electrical power, P_{elec}, and the displayed

value of T' on the camera of various points in vacuum including the trap and the glass reflection. The data from this calibration and the fit to the model for conduction and radiation, Eqn. 5.1, are shown in Fig. 5.6. We find that the conduction and radiation parameters from the fit to Eqn. 5.1 are larger than the values for the specifications. There is a considerable ($k' \approx 10^{-3}$ W/K) amount of conduction, which is reasonable given that the heater is in direct contact with the trap and the stainless steel holder. Increased radiation losses from hot elements connected to the heater makes the radiation parameter an order of magnitude higher, $\epsilon' \approx 10^{-4}$ m^2.

A close look at the low-power limit reveals that the data are systematically lower than the fit to the model. It's possible that at low temperatures, the model does not properly account for heater behavior due to unknown details about the heater; the heater is designed to operate at high power, reaching temperatures near 1000 °C. We assume the trap temperature and the heater temperature are the same, or at least similar to within measurement uncertainties.

We instead turn to an empirically determined calibration and compare the results to the model in Fig. 5.6b. The conversion from power P to T' has an empirically determined functional form:

$$T' = \kappa(1 - e^{-(1.387\ \mathrm{W}^{-1})P})\sqrt{P} + 20.68\ ^\circ\mathrm{C} \tag{5.4}$$

where $\kappa = 89.2\ \frac{^\circ\mathrm{C}}{\mathrm{W}^{1/2}}$. The data and the fit for the displayed 'temperature' in °C for the glass reflection are shown in Fig. 5.9. The conversion for a material with a lower emissivity, such as the trap surface, has a smaller value of κ, but follows the same curve.

The final empirical calibration curve from input power to actual trap temperature is the dashed line in Fig. 5.6b. In summary, we find that, for high powers, the calibration curve follows the model for conduction and radiation, despite the differences in the empirical form of the conversion from input power to actual temperature. The empirical curve provides a better estimate of the temperature at low applied powers, so we use this curve as the accepted conversion.

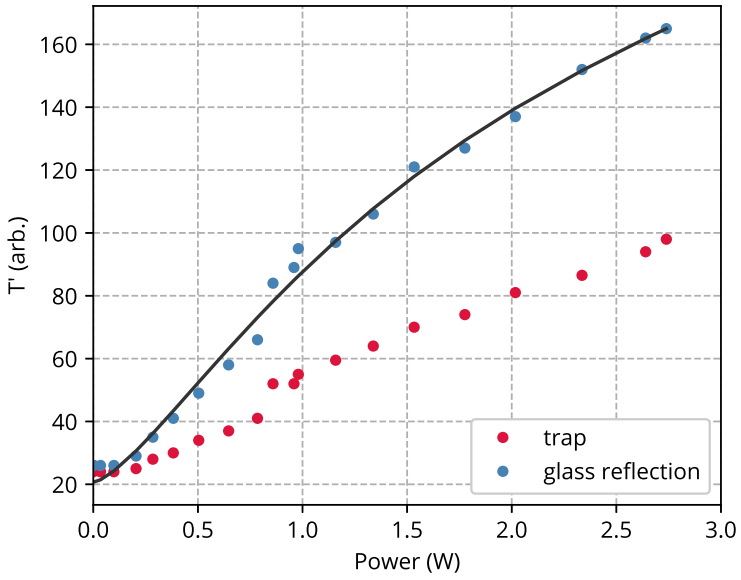

Figure 5.9: Displayed 'temperature' T' is from the thermal camera using the point function on the trap surface and glass reflection (corresponding to the maximum value recorded). The solid line is the accepted conversion input power to display 'temperature' as indicated by the SEEK Thermal software in °C

Chapter 6

Temperature and frequency scaling results

In this chapter, we report heating rate measurements and their dependence on temperature and frequency. We find that at high temperatures, the heating rates exhibit a saturation, contrary to expectations of a power law behavior. We rule out technical noise from the heater current and Johnson noise from the heater and the trap electrodes. The frequency scaling follows a near $1/f$ behavior, with a decrease in the power law exponent at high temperatures. A t-test is performed to determine the statistical significance of the decrease. Also in this chapter is an account of an anomalous event where heating rates were elevated at a single electrode for several days. The event serves as evidence for the dominance of surface noise in the measurements with this trap.

6.1 Temperature scaling

The temperature scaling was measured at three locations on the trap chip to find out how much the temperature dependence of electric-field noise varies across the surface trap. The locations were centered at electrodes 3, 4, and 5 (referred to as locations 1, 2, and 3), which are separated by distances of 120 μm and 220 μm as shown in Fig. 6.1.

For the temperature scaling measurements, the axial frequency is set to $\omega = 2\pi \times 1$ MHz to make comparisons to other reported results straightforward. For each trapping location in turn, the temperature was stepwise monotonically increased and heating rates were measured once the temperature stabilized at the desired point. We are able to measure heating rates from room temperature up to about 530 K. Ion lifetimes remain stable at several hours for temperatures up to about 450 K, then degrade quickly above that likely due to outgassing of materials near the ion. For the highest temperature data taken, ion lifetimes were only several minutes (long enough for about one heating rate measurement). During the data taking, the power delivered to the heater was used as an indication of temperature by monitoring the heater resistance and current applied. The heating rates at all three locations as a function

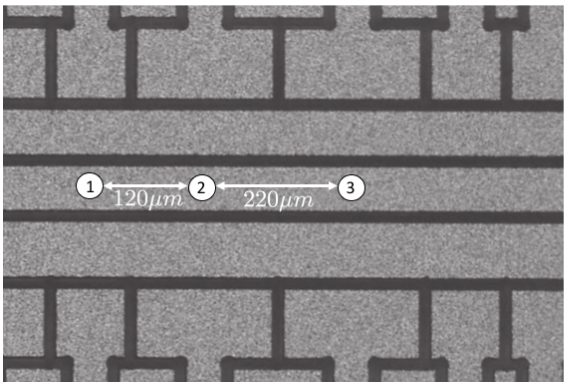

Figure 6.1: Optical microscope image of the trap showing the three locations where data was taken as presented in this thesis. The ion was trapped ≈ 72 μm above this surface.

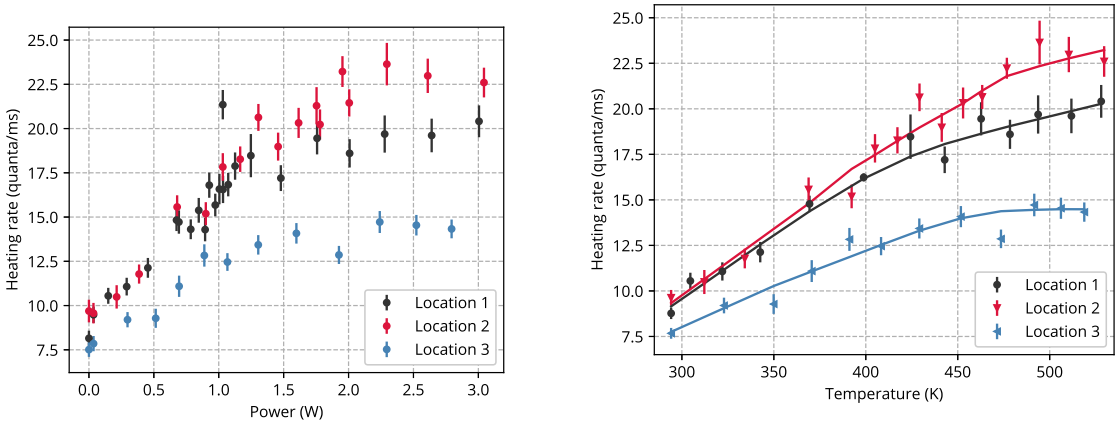

Figure 6.2: (a) Heating rates from all three locations indicated in Fig. 6.1 as a function of power delivered to the heater. Each heating rate was measured using the carrier Rabi flop method (Sec. 3.5). (b) Post-processed data has been weighted-averaged with a 2% window on temperature. The power was converted to temperature using thermal camera calibrations detailed in Sec. 5.3.

of applied power are documented in Fig. 6.2a for measurements taken over a one week span.

We expect that different locations on the same trap to show similar heating rate behavior since the trap material and previous treatment does not vary between them. Any differences would be ascribed to location surface variations and would indicate the magnitude of those variations. We observe variations of about $20 - 25\%$ at room temperature and a similar saturation point of two times the room temperature values.

Heating rate data was post-processed for ease of analysis and conversion of power into temperature. The power was converted to temperature using calibrations with the thermal camera (Sec. 5.3). There is a systematic uncertainty in the difference to room temperature

of ±10% that does not significantly affect the analysis or conclusions drawn from the results (discussion in Sec. 7.4). A weighted average heating rate is presented with a temperature window of 2% for grouping measurements at the same temperature in Fig. 6.2b. Also included in Fig. 6.2b is a smooth curve to aid in data analysis. The smooth curve is calculated using local regression smoothing as implemented by the 'lowess' function in the StatsModels python package [53]. For each data point x_i, the method takes a fraction (0.55) of the closest data points and does a linear regression weighted by distance from $x_i - x_j$. This process is iterated 100 times to find a 'smoothed' value of the curve at x_i.

6.2 Ruling out technical noise

In order to confirm that the observed behavior is due to surface-related noise, we must rule out technical noise possibilities such as current or Johnson noise from the heater.

Current noise

To test if the rise in heating rates was proportional to current applied to the heater, we measured heating rates while the heater was at a reduced current, 'off', but still at an elevated temperature. The procedure was to

- use a high heater current to heat the trap above 400 K
- turn the current down to 0.3 A over the span of about 3 minutes, a safe ramp speed for the heater
- calibrate the line center and magnetic field (takes about 1 minute)
- repeat heating rate measurements with carrier Rabi flops at 0 and 5 ms and record the heater resistance during the measurement

This procedure was done twice, starting with 1.4 and 1.5 A on the heater, respectively. The results are shown in Fig. 6.3. In general, when increasing the temperature by 10 K in a single step with the heater running, it takes about 5-10 minutes for the temperature of the trap to stabilize. Additionally, this particular procedure also shows that a three minute ramp down and one minute wait time starting from $\approx$ 420 K ends up at $\approx$ 360 K. If the elevated heating rate was due to the current in the heater, then one would expect the heating rate to immediately drop due to the reduced current. However, we observed that the heating rate followed the same behavior with resistance, and the current did not contribute. The resistance of the heater is a good indicator of temperature.

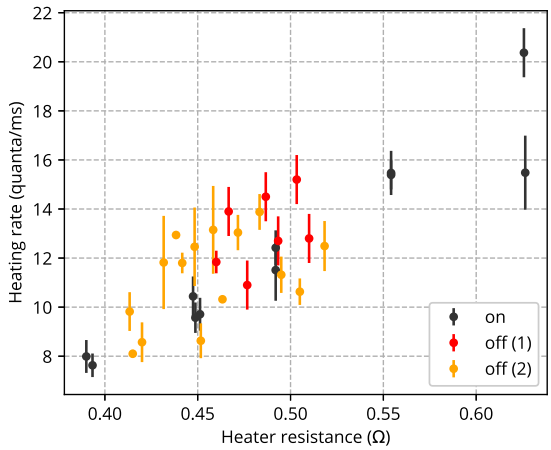

Figure 6.3: In black are heating rates measured with the heater on, where increasing resistance also corresponds to increasing temperature. Heating rates in red and orange were measured with the heater current at 0.3 A, while the trap cooled in ambient conditions. The wide spread is due to the rough method that was used, as detailed in Sec. 6.2.

Johnson noise

Another possible source of noise unrelated to surface dynamics is Johnson noise, as previously described in Sec. 3.2. While this type of noise is present in all conductors in our system, the temperature scaling observed reveals that the dominant source of noise is localized to components in our system that undergo temperature changes when the heater is activated. First, we consider the thin metal film of the trap and estimate the level of Johnson noise that might be present at even the highest temperatures measured. The DC resistance of an ideal thin film depends on temperature by [31] [54]

$$R = R_0(1 + \alpha(T - T_0)) \tag{6.1}$$

where alpha is a factor that depends on the grain structure of the thin film and ranges from 0.01 to 20, and R_0 is the resistance at room temperature T_0. This would result in a temperature dependence of $S_E \propto T^2$, which is already inconsistent with the observed results. For aluminium, $\alpha \approx .004$ K^{-1} , which results in a noise spectral density for Johnson noise (Eqn. 3.2) from the trap electrodes at 530 K of $\dot{\bar{n}} < 10^{-4}\ \frac{\text{quanta}}{\text{ms}\cdot\Omega} \times R_{300\text{K}}$. (For $^{40}Ca^+$ and a trap frequency of 1 MHz, spectral density in V^2/m^{2}Hz can be quickly converted to heating rate in quanta/ms by $\dot{\bar{n}} = S_E \times 1.5 \times 10^{11}$.) The lowest heating rate we observe at 530 K is about 14 quanta/ms. If Johnson noise were a contributing factor at this high temperature, that would imply a room temperature resistance of 1 kΩ. In previous work with this same set up, the resistance of an electrode and wirebond connection was estimated to be 6-8 Ω [30]. Using this more realistic estimate, the Johnson noise at 530 K would be $< 10^{-3}$quanta/ms,

which is five orders of magnitude lower than observed values and likely does not play a role in the presented measurements.

There might also be Johnson noise from the heater itself, of which we have measured the resistance as a function of temperature (see Sec. 5.3 for details). The resistance of the heater at maximum temperature measured of ∼530 K is 1.2 Ohm. The ion is a distance of 72 μm from the trap surface and the trap chip is ∼500 μm thick, for a total distance of d = ∼570 μm. The effective distance (Eqn. 3.3) is difficult to calculate since the exact geometry of the trap relative to the heater is not straightforward to estimate. However, we can take a worst-case scenario and assume the effective distance is the actual distance of 570 μm. These parameters result in $S_E \approx 10^{-13}$ V^2/m^{2}Hz or $\dot{\bar{n}} \approx 10^{-2}$ quanta/ms, which is three orders of magnitude lower than recorded heating rates at that temperature. Additionally, the heater resistance continues to increase at high temperatures, but the heating rates do not, which contradicts the proportional behavior predicted by Johnson noise. It is also important to note that the heater is enclosed in a conducting, grounded, molybdenum shell that likely shields any noise from the resistance inside even more.

6.3 Frequency scaling results

Initially, the frequency scaling was measured using 4-6 different frequencies over the full possible range given the limitations of the output of the DC voltage sources. Due to the geometry of the trap electrodes, and the larger size of electrodes 4 and 5, higher trap frequencies were reachable at locations 2 and 3 than at location 1. Fig. 6.4 shows the results of those measurements at both room temperature and elevated temperatures. This full range measurement shows that the scaling is $1/f$ over the entire range of accessible frequencies. There is also no sign of technical noise such as a peak in the spectrum.

A new, more precise measurement was done next to reduce the uncertainty in the heating rate measurements for better estimates of the scaling exponent α. For each location and temperature, the highest and lowest possible frequencies were chosen given the limitations of our electronics and the high heating rates at low frequencies. This procedure of taking data over extended periods of time also minimizes the influence of slow drifts in the experimental apparatus, such as the laser alignment, or drifts in the experimental parameters, such as laser power. Over the course of several hours, we cycle through the high and low frequency heating rate measurements, with a total of 10-20 rates per frequency. For each frequency, we compile all $\bar{n}(t_{\text{wait}})$ and fit to a single line. Both the initial and the precise measurements are shown in a single plot in Fig. 6.4b and the exact values and uncertainties are reported in Table 6.1. The precision frequency scaling improved uncertainties on the frequency scaling exponent at each location from the initial measurements with 3-10% uncertainty to 2-3% uncertainty. Additionally, the spread of values across locations at high temperatures improved from 6% to 2%.

We note that intensity noise on sub-second timescales on the laser driving the Rabi flops causes a faster decay of the Rabi flops which, for our experimental parameters, leads to a

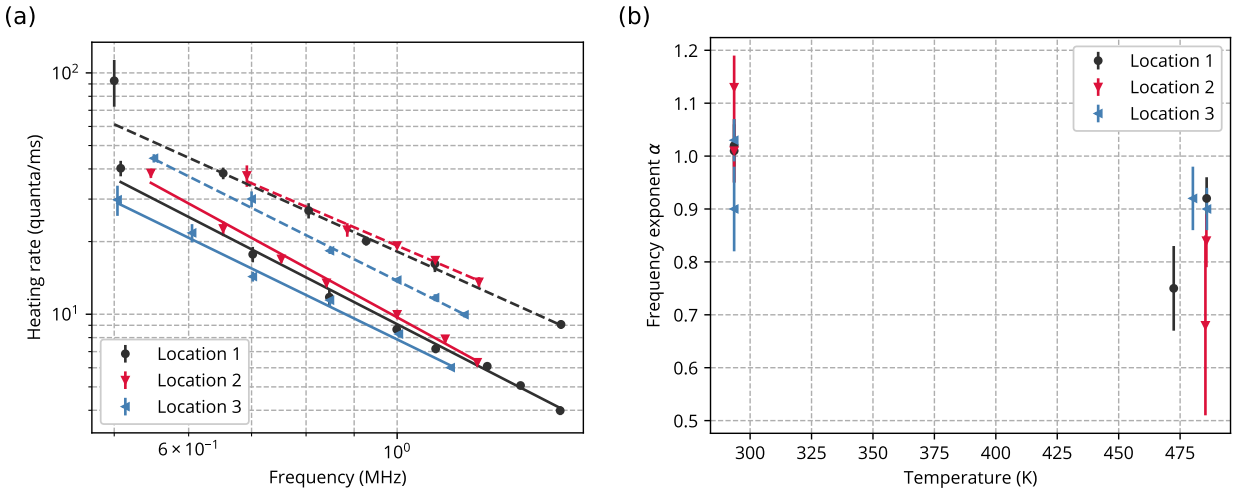

Figure 6.4: (a) Initial frequency scaling results at all three locations shows a $1/f^{\alpha+1}$ dependence. Each data point is the weighted average of several heating rate measurements, and not a conglomerate linear fit to all $\bar{n}$ data as in previous temperature scaling data. The dashed lines and corresponding data are measurements at high temperatures and the solid below are at room temperature (b) Combined full frequency scaling and precision frequency scaling results for the frequency scaling exponent α as a function of temperature.

slight underestimate of heating rates at low trap frequencies and a slight overestimate of heating rates at high frequencies. Consequently, our calculation of the scaling exponent α likely underestimates the true value by 1-3 %, which is smaller than our measurement uncertainty.

The main takeaways of these frequency scaling results are first, that α is close to one, which narrows the possible models that explain the behavior. Second, there is a downward trend in the α values as the temperature is increased. In the following section, we quantify that decrease and develop a statistical test for proving that the decrease is real.

6.4 t-test for frequency scaling

Having observed a discernible decrease in the value of the frequency exponent α at high temperatures, it is desirable to develop a statistical statement about the validity of the results. The t-test was developed in the 1908 paper written by William Gosset under the alias "Student" under the employ of the Guinness Brewing Company entitled "The Probable Error of a Mean" [55]. It is a test that is suitable for small sample sizes, such as the three locations we present. The result of the test is a confidence interval for rejecting the hypothesis that α remains unchanged at high temperatures, and thereby confirming that the decrease is statistically significant.

Location	293 K	480 K	$\alpha_R - \alpha_H$
	α_R	α_H	$\Delta\alpha$
1	1.02(4)	0.92(4)	0.10(5)
2	1.01(6)	0.84(5)	0.17(8)
3	1.03(4)	0.90(4)	0.13(5)
1'	1.01(6)	0.75(8)	0.26(10)
2'	1.13(6)	0.68(17)	0.45(18)
3'	0.90(8)	0.92(6)	-0.02(10)
Average			0.13(3)

Table 6.1: Results of the fits for the frequency scaling results at room temperature and high temperature to the form $\dot{\bar{n}} \propto 1/\omega^{\alpha+1}$. Primed locations refer to the full range frequency scaling results and unprimed are precision scalings. An analysis of the statistical significance of $\Delta\alpha$ follows in Sec. 6.4 showing that α is in fact decrased at higher temperatures.

Theory

In the case that a data sample is not sufficiently large, it is difficult to determine with certainty the true parent distribution from which the sample is drawn. Instead of using a normal distribution, it is necessary to use a probability distribution which accounts for the underestimation of the standard deviation due to a small number of samples, namely a Student's t-distribution:

$$p_t(t,\nu) = \frac{1}{\sqrt{\nu\pi}} \frac{\Gamma((\nu+1)/2)}{\Gamma(\nu/2)} \left(1 + \frac{t^2}{\nu}\right)^{-(\nu+1)/2} \tag{6.2}$$

The Student's t-distribution gives the probability that a sample mean is a certain distance from the true mean. That distance is expressed as the number of standard deviations of the sample and referred to as the t-value. The distribution is a function of the t-value and the number of degrees of freedom ν, which for N samples with the mean calculated from those samples results in $\nu = N - 1$.

Figure 6.5 shows a comparison between the normal and the Student's t-distribution for $\nu = 2$. If N samples have a mean $\overline{x}$ and standard deviation s and the true population has a mean μ, the t-value of the result is

$$t = \frac{\overline{x} - \mu}{s} \tag{6.3}$$

For a positive t-value single tail test, the probability that such a result occurred for an assumed true mean μ is

$$P_{\overline{x}} = \int_t^\infty p_t(t,\nu) \tag{6.4}$$

and the confidence level of a result is stated as the rejection of the hypothesis that μ is the true mean as a percentage $100\% \times (1 - P_{\overline{x}})$.

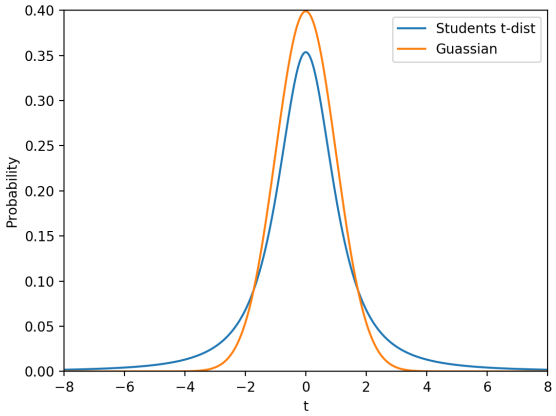

Figure 6.5: Comparison of Gaussian normal distribution and the Student's t-distribution (Equation 6.2) for the same mean and sample standard deviation and two degrees of freedom. The t-distribution has longer tails that account for the underestimation of the standard deviation

Application

The t-test is applied to the frequency scaling data in Table 6.1. To determine if the frequency scaling exponent α is changed at high temperatures, there are two ways to approach the results. First, each location can be treated separately and may have a different true value of $\Delta\alpha$. The uncertainties reported in Table 6.1 are standard one sigma uncertainties, and could be used to find Gaussian confidence intervals. However, a second approach takes the three locations together as samples from a larger population that consists of measurements at more locations. A t-test may be applied applied to the difference $\Delta\alpha$ across the larger population. For an assumed true population mean of $\mu = 0$ and an unweighted standard deviation of the six samples (two at each location), the t-value is $t = 4.4$. This t-value results in a 99.6% confidence level rejection of the hypothesis that the frequency scaling remains unchanged at high temperature when the location is varied. Instead, a decrease of 0.13(3) is observed in the frequency scaling exponent. This results predicts that $\Delta\alpha$ would also be non-zero if we measured at more trapping locations.

6.5 The anomaly

The following is an account of a single dramatic change in the heating rate specifically at trapping location 1 (E3). It is likely that the change was a result of surface properties, since the change was local, temporary, still followed close to $1/f$ scaling in frequency, and showed similar temperature scaling results. This anomaly happened prior to the data presented in the previous sections.

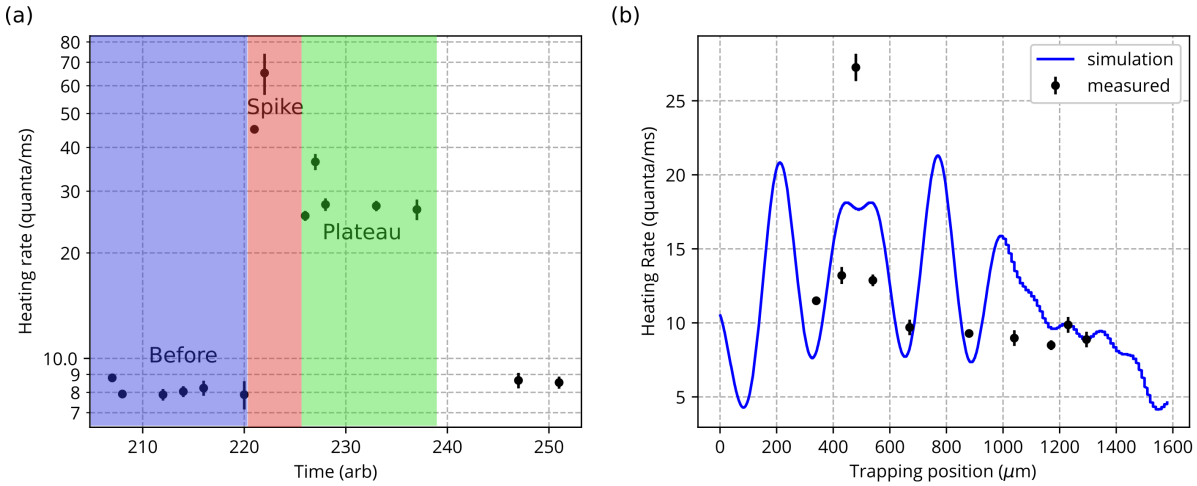

Figure 6.6: (a) Room temperature heating rates at E3 over time. The shaded region labels are used in the text for discussion of the event. (b) Black data point are heating rates taken after the spike, during the 'plateau', across the length of the trap. The simulation is for voltage noise that is uncorrelated between electrodes and does not show a match to the observed behavior. The overall amplitude of the simulation is arbitrarily normalized to a single heating rate value (at 1300 μm), and we only compare relative values at different locations.

After several weeks of operation of the heater and trap, we increased the power applied to the heater to about 6 W. The calibration curve from Chapter 5 does not apply to the heater behavior prior to the anomaly, but we estimate that the temperature reached was in the range of 300-350°C based on comparisons of IV-curves and heating rate measurements before and after. The goal was to outgas the heater and trap to improve ion lifetimes at the upper temperature range of measurement. After cooling back down to room temperature, the heating rate at E3 spiked to about eight times it's normal value. The heating rate at that location at room temperature is plotted over time in Fig. 6.6a. 'Before' the spike, the heating rate was about 8 quanta/ms. During the worst of the 'spike', the rates were extremely elevated to > 50 quanta/ms. Within a few days after the spike, the rates 'plateaued' in the high twenties for several days. Fig. 6.6b shows the heating rates by location across the trap during that plateau. About one week later, after several iterations of heating the trap and measuring at other locations, the heating rates return to the 'before' values. These labels of 'before, 'spike', and 'plateau' will be used for further discussion of the event.

We can rule out this being a new source of technical noise with simulations of voltage noise. The type of noise simulated is technical noise correlated across a single electrode, but uncorrelated between them. Due to the varying shape of the electrodes across the trap, uncorrelated voltage noise on all electrodes has a varying projection on the axial mode of motion along the trap axis and the effects add to give a total amount of noise that varies

Time	A	α
Before	9.2(1)	1.04(4)
Spike	57.4(9)	1.45(9)
Plateau	23.5(4)	1.86(11)

Table 6.2: Summary of fit parameters for frequency scaling measurements taken before, at the spike, and during the plateau. Those times are labeled in Fig. 6.6 and described in Sec. 6.5.

along the trap axis. The results of a simulation of this type of noise along possible trapping positions is shown in Fig. 6.6b alongside heating rate measurements taken during the plateau. The behavior observed does not match the simulation for this type of noise and the heating rate data show that the anomaly was isolated to E3. The only quantifiable difference between the locations along the trap is that prior to this incident, we had only been actively trapping at E3, making it more exposed to laser light over that period of time, including during heating.

Temperature scaling measurements were also taken at the corresponding times, and those results are shown in Fig. 6.7a. In addition, frequency scaling measurements taken immediately during the highest spike and after that while the noise showed a high plateau show approximately $1/f$ scaling. The frequency scaling of the noise 'before', at the 'spike', and during the 'plateau' in time is plotted in Fig. 6.7b and the fit parameters for $\dot{\bar{n}} = A/\omega^{\alpha+1}$ are available in Table 6.2.

In summary, the anomaly was an interesting event that occurred in the middle of trap operation. The only difference between locations can be attributed to the location of the anomaly having more laser exposure. It is also possible that another unknown surface factor such as a calcium granule from the oven caused the elevated noise level.

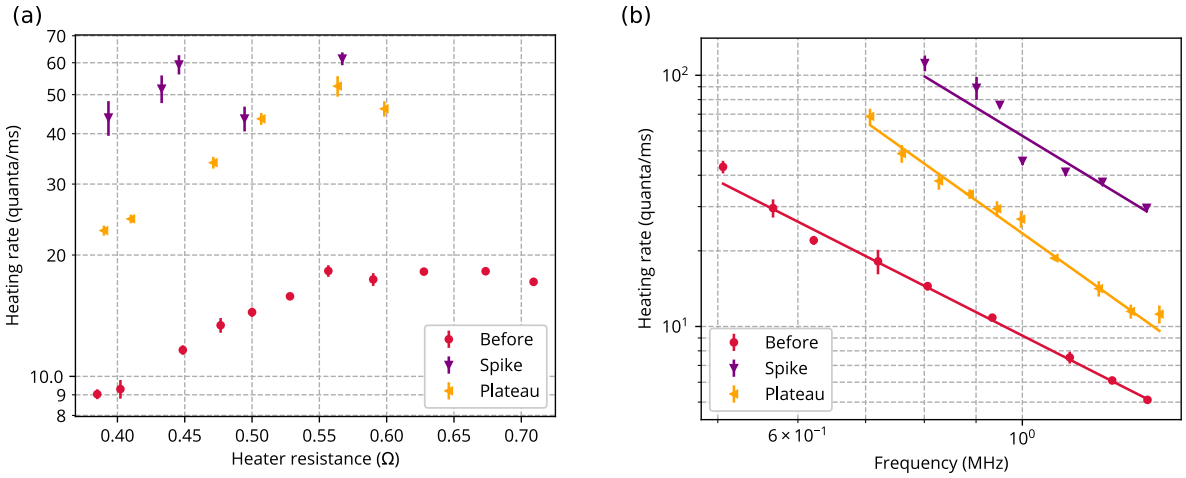

Figure 6.7: (a) Temperature scaling results before, at the spike, and during the plateau. Resistance of the heater is used as an indication of temperature since the we do not have a reliable temperature calibration prior to the spike. (b) Room temperature frequency scaling measurements before, at the spike, and after the spike during the plateau with fits to $\dot{\bar{n}} \propto \omega^{\alpha+1}$ with parameters in Table 6.2.

Chapter 7

Results in the context of the thermally activated fluctuator (TAF) model

7.1 TAF model

In a 1939 French manuscript, Surdin proposed a model for 'Flicker noise' in metals that explained the $1/f$ characteristic of the noise based on a distribution of electron recombination constants and thermally activated currents [56]. In a similar vain, a modification to Schottky's theory for flicker noise was proposed in 1950 that postulated a spread in the values of the diffusion barrier across a metal surface. An equal spread of barriers accounted for experimentally observed $1/f$ dependence of the noise. [57, 58] Finally, in 1979, Dutta, Dimon, and Horn refined the theory for $1/f$ noise into a general model assuming only that the noise is caused by random thermally-activated processes [5]. The theory was further explained and put into the context of measurements in the 1981 review by Dutta and Horn [59].

General theory

A thermally-activated process is described by a two-state system with an energy barrier for traversing between the two states. Thermal energy drives the process randomly between states, with statistics determined by the Boltzmann distribution. This general process is illustrated in Fig. 7.1, including a sample time evolution of the state of the system, called random telegraph noise. We call such a system a thermally-activated fluctuator (TAF), because it's state fluctuates in time. There are many physical process that can be described by such a model such as an atom moving in a lattice, a molecule that desorbs from and re-adsorbs to the surface, a defect hopping over a grain boundary, or a configuration of atoms changing their orientation or lattice structure.

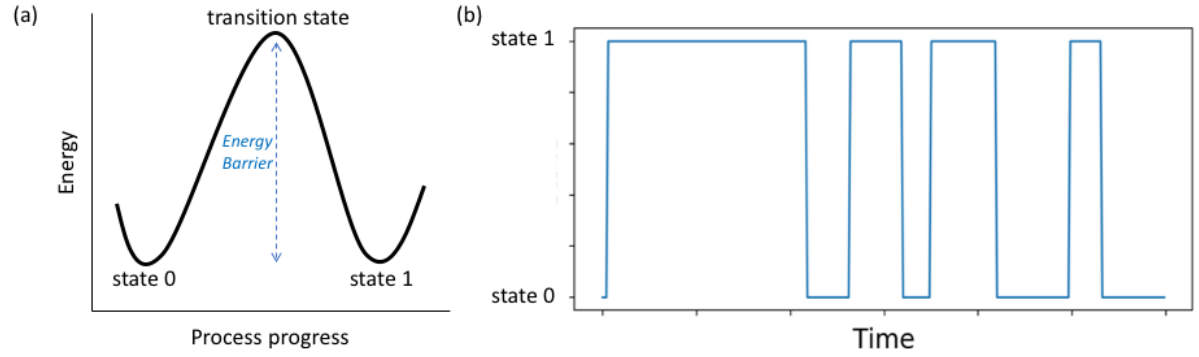

Figure 7.1: (a) Energy diagram over the course of a general thermally activated process. As the process progresses, the system moves from state 0 to state 1 through a transition state. This progression requires enough energy to surmount the energy barrier. The process may proceed in both directions. (b) Sample random telegraph noise, in which the state of the system switches over time via thermal activation.

In general, a randomly switching 2-state system with a characteristic time, τ, has an auto-correlation function

$$\langle x(t)x(t-t_0)\rangle \propto e^{-|t_0|/\tau}.$$

By the Wiener-Khintchine theorem, the Fourier transform of the autocorrelation function is the noise spectral density of the random process [60]

$$S(\omega) = \frac{\tau}{\omega^2\tau^2+1},$$

which is a Lorentzian spectrum with a corner frequency of τ^{-1}.

If the process is thermally activated then $\tau = \tau_0 e^{E/kT}$ where E is the activation energy of the process, and T is the temperature of the thermal bath. This equation for τ can be derived from an integral of the Boltzmann distribution above the activation energy [60], and was first derived from published experimental data by Arrhenius in 1889 for chemical reaction rates [61]. It can be thought of as a relaxation time for the process, where τ_0 is the time between attempts to surmount the energy barrier, and $e^{E/kT}$ is the fraction of times that it will make it [60, 62]. With this substitution for τ, the noise spectral density will then also depend on temperature:

$$S(\omega,T) = \frac{\tau_0 e^{E/kT}}{\omega^2\tau_0^2 e^{2E/kT}+1}. \tag{7.1}$$

For a fixed frequency, the noise will exhibit a peak when $\omega = \tau^{-1}$, or equivalently when $k_\mathrm{B}T_\mathrm{peak} = -E/\ln(\tau_0\omega)$. This peak will be broad for high energy barriers, with a width of about $k_\mathrm{B}T_\mathrm{peak}$. An example of the noise from a TAF with a barrier of 0.5 eV is illustrated in Fig. 7.2 with the frequency spectrum near the peak and the corresponding temperature dependence of the noise $S(\omega,T)$ at $\omega = 1$ MHz.

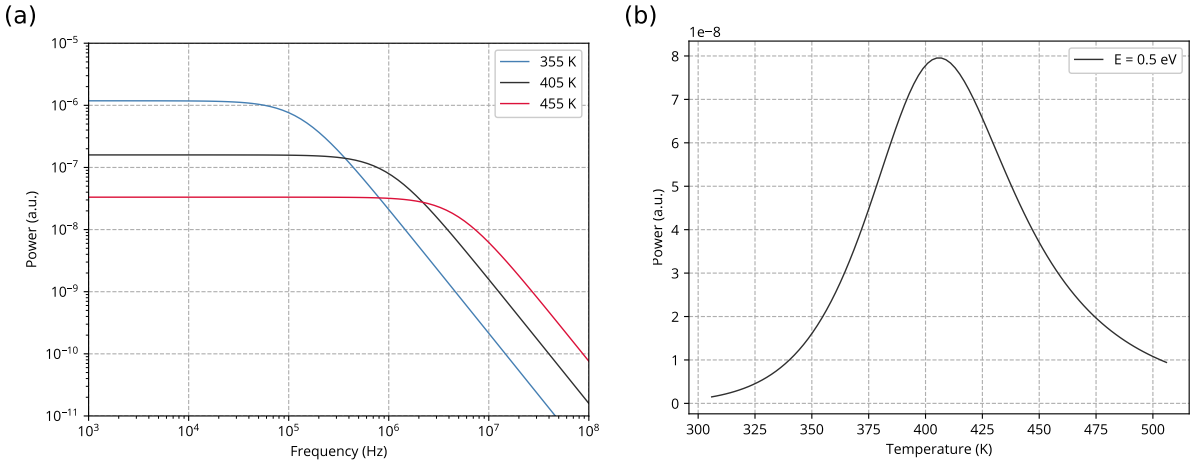

Figure 7.2: (a) The power spectral density of a single fluctuator with an energy barrier of 0.5 eV at three different temperatures. As the temperature is increased, the Lorentzian spectrum is broadened, and the noise occurs at higher frequencies due to the increasing probability of overcoming the energy barrier. The black curve at 405 K corresponds to a corner frequency of 1 MHz. (b) The temperature dependence of the noise at 1 MHz of a single 0.5 eV barrier fluctuator. The noise peaks at 405 K corresponding to the temperature at which the corner frequency of the power spectral density is 1 MHz.

If we now consider a large number of fluctuators with different activation energies that have a distribution $D(E)$, then we add all of their contributions to the total noise spectral density

$$S(\omega, T) = \int \frac{\tau_0 e^{E/kT}}{\omega^2 \tau_0^2 e^{2E/kT} + 1} D(E) dE. \tag{7.2}$$

S is now a function of frequency, ω, and temperature, T, and a distribution of activation energies, $D(E)$. The simplest assumption for this equation is that there are a fixed number of fluctuators with set energy barriers and τ_0 is the same for all fluctuators. It is possible that $D(E)$ might actually be $D(E, \tau_0, T)$, with a distribution of values for τ_0, and energy barriers or total number of fluctuators that depends on temperature. For now, we continue with an assumed average value of τ_0, since varying τ_0 by even an order of magnitude changes T_{peak} by less than 15% and does not affect our use of the model or conclusions. We also assume that $D(E)$ is independent of temperature. If the density were to change with increasing temperature, this would likely result in a temperature dependence of the noise that can not be explained by the model, such as sharp inclines and unexplained frequency scaling dependence.

Equation 7.2 can also be written as

$$S(\omega, T) = \int \frac{1}{\cosh(E - \bar{E})/k_{\text{B}}T} D(E) dE \tag{7.3}$$

and it is easier to see that the integrand is a strongly peaked function at $E = \bar{E}$ with $\bar{E} \equiv -k_B T \ln(\omega\tau_0)$. Assuming that $D(E)$ varies smoothly on the scale of $k_B T$ (a valid assumption for most physical processes), we can take the value of the integrand at the peak. To make a further approximation, we Taylor-expand the integrand around $E = \bar{E}$ and take the first term to determine an approximate expression for $D(E)$ given a measured noise spectrum $S(\omega, T)$:

$$D_{\text{approx}}(E) = \frac{\omega}{k_B T} S(\omega, T). \tag{7.4}$$

We now define a frequency scaling exponent α where $S \propto \omega^{-\alpha}$. The exponent α is then derived from Eqn. 7.4 using $\alpha = -\frac{\partial \ln S}{\partial \ln \omega}$ [59]:

$$\alpha(\omega, T) = 1 - \frac{1}{\ln \omega\tau_0} \left(\frac{\partial \ln S}{\partial \ln T} - 1 \right). \tag{7.5}$$

In this model, the frequency scaling exponent α depends on temperature and its approximate dependence can be linked to the temperature scaling by Eqn. 7.5. This correspondence between frequency and temperature scaling can be used to test the applicability of the model.

7.2 Caveats to application of the TAF model

Approximating the distribution

The approximation in Eq. 7.4 is only valid if the integrand in Eq. 7.3 is sharply peaked compared to $D(E)$. The function $\cosh^{-1}(E - \bar{E})$ has a FWHM of about $k_B T$, so the approximation breaks down when $D(E)$ has any features that are sharper than that. Additionally, as $k_B T$ increases, neglect of higher order terms of the Taylor expansion leads to an overestimation of $D(E)$. This effect can be corrected for in the analysis by inserting $D_{\text{approx}}(E)$ into Eq. 7.2 and comparing the back-calculated $S(T)$ to the measured data. We then apply a multiplicative correction to $D_{\text{approx}}(E)$ to report closer to the estimated true value of $D(E)$.

Distribution degeneracy

A careful look at Eq. 7.2 reveals that $D(E)$ derived from $S(T)$ at a fixed frequency is not a unique distribution.

First, there is an intrinsic limit to the resolution that can be extracted from $S(T)$. A single fluctuator has a distribution that is a δ-function at its energy barrier. However, the peak in $S(T)$ from a single fluctuator has a width on the order of $k_B T$, like the example in Fig. 7.2b. In analogy to an optical resolution, two peaks in the distribution can only be resolved in $S(T)$ if they are separated by an energy on the order of $k_B T$. While the physical distribution of energy barriers may have features sharper than that, they will not be reflected in the observed behavior.

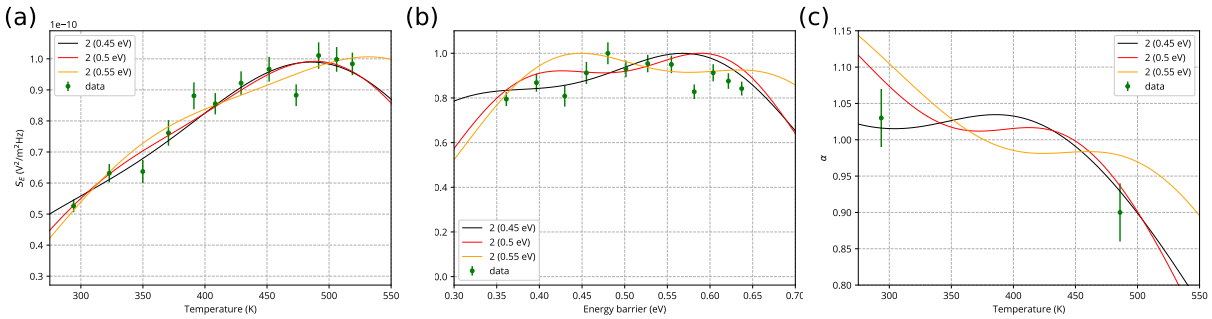

Figure 7.3: An illustration of the uncertainty in the underlying distribution that can explain the observed data. (a) Data from location 3 plotted with three different noise spectra from the corresponding distributions in (b). (b) Data converted to D_{approx} and the three test distributions. (c) Calculated α dependence for each distribution and the precision frequency scaling α data from location 3.

Even if we assume some continuity and smoothness of $D(E)$, it is possible that several distributions may exhibit similar temperature scaling behavior. Figure 7.3 illustrates this point using a distribution that is the sum of two Gaussians and varying the center between them. The data is fit to three different distributions, each with two Gaussians equally spaced from the indicated center point. Their widths and spacing are constrained to be equal, and the amplitudes are varied to fit the data. All three fit the data reasonably well, despite their qualitative differences. Even though $S(T)$ is similar for all three variations (Fig. 7.3a), the distributions have distinct characteristics (Fig. 7.3b).

Finite range of data-taking

Experimentally, the information that can be extracted is limited to the range of data taken (in frequency and temperature), which translates into a finite range of energy barriers that can be effectively probed. As evidenced in Eqn. 7.5, the behavior of the frequency exponent alpha is sensitive to the slope of $S(T)$, which comes from the slope of the underlying distribution. Due to the large uncertainty on slope at the end of the range of meseaurement, the predited α value is especially sensitive at the end of the range (Fig. 7.3c). These properties will be discussed further in the context of the measured data in the following section.

7.3 The data in the TAF model

To apply the TAF model to the data and find a distribution of energy barriers, we must first choose an appropriate value for the parameter τ_0, where τ_0^{-1} is the attempt frequency for surmounting the energy barrier. For the movement of atoms in a crystal lattice, the relevant quantity is the characteristic atomic vibrational frequency. In solid state systems such as

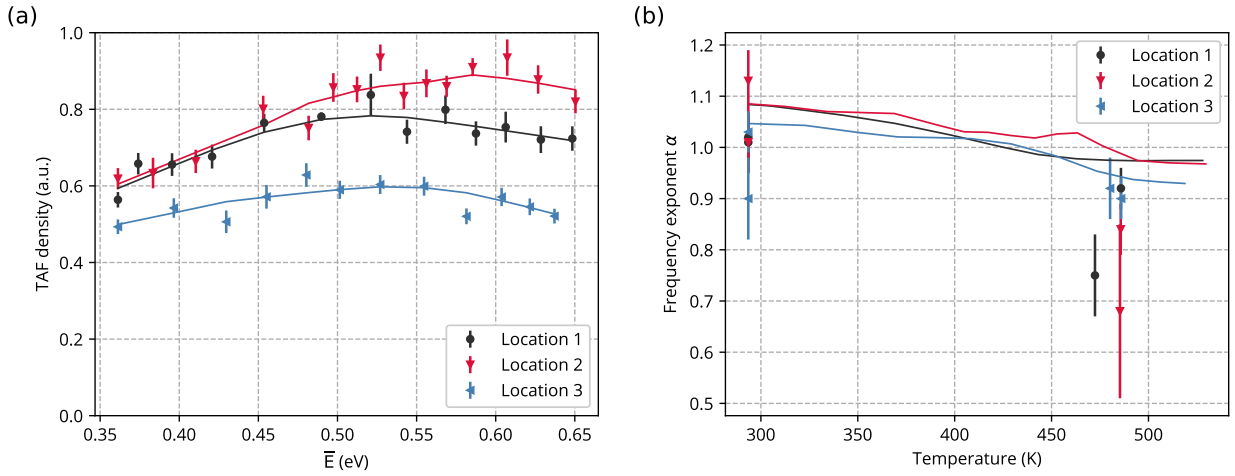

Figure 7.4: (a) Calculated and corrected distribution of energy barriers that can explain the observed temperature scaling. We observe a broad peak around 0.5 eV at all three locations. This distribution is the clue to the underlying physical mechanism. (b) Predicted frequency exponent behavior derived from the smoothed curve of the temperature scaling data together with the measured values at all three locations. We see a match between the predicted downward trend and the data.

thin metal films, the Debye frequency ω_D quantifies the highest frequency phonon mode of the lattice, and is a good estimate for the appropriate value of τ_0^{-1} [62]. Additionally, typical relaxation times observed in condensed matter are usually $10^{-14} - 10^{-11}$ sec [60]. In the following analysis, we assume $\tau_0 = 10^{-13}$ and note that even a change in τ_0 of an order of magnitude results in a less than 15% change in the corresponding energy barrier $\bar{E} \equiv -k_B T \ln(\omega\tau_0)$ in the range of frequency and temperature relevant to this data. This change would result in a small shift left or right of the calculated distribution. The effect on the predicted α behavior is less intuitive, but essentially results in a change in the slope of the prediction that is smaller than the experimental uncertainties.

Over the range of measurable energy barriers, determined by frequency and temperature range, we find the results can be described as coming from a distribution of fluctuators with a broad peak around 0.5 eV at all three locations (Fig. 7.4a). Using the smoothed lines (see Sec. 6.1 for details), we calculated the predicted frequency scaling exponent behavior and plot it with the frequency scaling data in Fig. 7.4.

The expected behavior of α can be intuited from the slope of the TAF distribution. A flat distribution results in a frequency scaling of exactly $\alpha = 1$, which can be easily seen in Eqn. 7.5 when S is linear in temperature and $\frac{\partial \ln S}{\partial \ln T} = 1$. With an increasing slope, there are more high-energy barriers that oscillate less frequently at a given temperature, resulting in slightly more low frequency noise, and an increase above one in α. Conversely, if the slope is decreasing, there are more low-energy barriers that oscillate more frequently at a

given temperature and α is tipped in the other direction to slightly below one. Given the broad peak in the distribution, we expect α to be larger than one at room temperature, and less than one at elevated temperatures (Eqn. 7.5). We find that the decrease in α at high temperatures is consistent with the predicted downward trend. As detailed in Fig. 7.3, there is some uncertainty associated with the predictions of the frequency scaling exponent, but the downward trend is still in qualitative agreement.

7.4 Temperature uncertainty

The trap temperature is estimated from thermal images of the trap/heater assembly as detailed in Sec. 5.3. We conservatively estimate the uncertainty in the difference to room temperature of $\pm 10\%$. In this section, we discuss the implications of the uncertainty in the context of the TAF model.

In Fig. 7.5, we consider the extreme cases of emissivity deviations of $+10\%$ (the low-temperature case) and -10% (the high-temperature case) for data collected at location 1. Figure 7.5a replicates the the temperature scaling from location 1: depending on the temperature calibration, the data are stretched to higher or compressed to lower temperatures. The effect on the fluctuator distribution is qualitatively similar, as we map temperature to fluctuator energy.

The frequency scaling exponent α is related to the slope of the noise spectrum by Eqn. 7.5, and the noise spectrum is proportional to the heating rate. As depicted in Fig. 7.5a, the systematic shift in temperature either stretches or compresses the noise spectrum with respect to temperature. Due to the steeper slope when the curve is compressed, in the low-temperature case α is expected to change more steeply across the temperature range. In the high-temperature case it varies more weakly due to the smaller values of the slope of the spectrum. Figure 7.5b shows the differing predictions for α depending on the accepted temperature values, and illustrates how this contributes to the uncertainty in the prediction in Fig. 7.4.

7.5 Connection to a physical mechanism

The TAF model itself does not assume a physical microscopic mechanism that is behaving as a TAF. In the case of a trapped ion, a TAF must consist of a changing charge distribution that has a state-dependent electric-field above the surface. While the possible noise sources that could behave as TAF in our trap is an open research question, we can speculate on some possibilities. First, we calculate, under some simple assumptions, the number of TAF-dipole sources that could reach the level of noise observed in our trap. Next, we connect our results to a large body of work on the $1/f$ noise in solid state systems and suggest that defect dynamics may play a role in the noise.

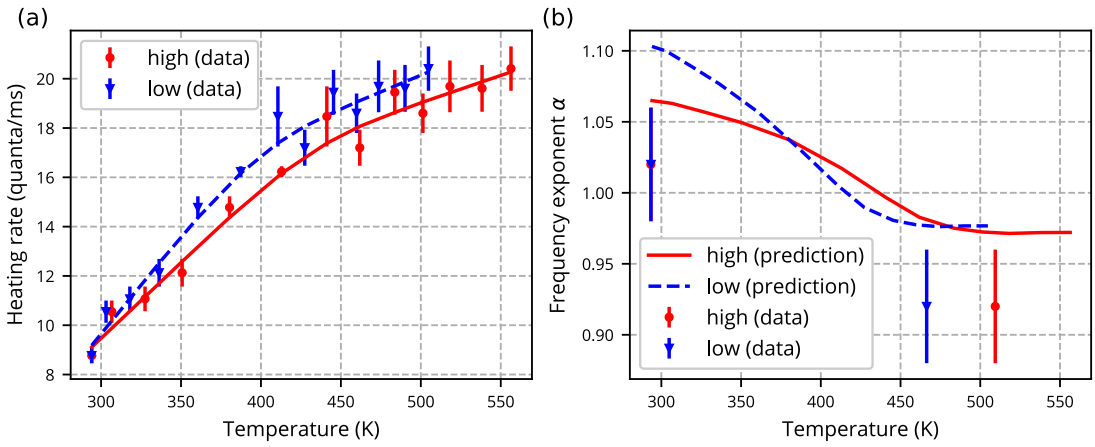

Figure 7.5: Exploring the implications of uncertainty in trap temperature. We conservatively estimate a 10% uncertainty in the emissivity of the reflection of the bottom glass of the trap based on independent calibrations. The 'high' ('low') temperature data assumes a 10% lower (higher) emissivity, and the data is shifted to the right (left). (a) The effect on the temperature scaling data of this uncertainty. The effect on the fluctuator distribution is qualitatively similar. (b) The effect of the uncertainty shifts the frequency exponent data in the same manner, but the prediction is different due to the new slope of the temperature scaling.

Simple dipole extension of TAF

Here we discuss the number of fluctuating dipole noise sources needed to reproduce the electric-field noise level in our trap. Electric field fluctuations parallel to the surface due to an averaged dipole fluctuation spectrum S_μ are given by [19]

$$S_{\mathrm{E}} = \frac{3\pi}{4\sigma_d} \frac{1}{(4\pi\epsilon_0 d^2)^2} S_\mu, \tag{7.6}$$

where σ_d is the areal density of dipoles, and d is the distance to the electrode surface. For a distribution of energy barriers $D(E)$,

$$S_\mu = \mu^2 \frac{\pi k_{\mathrm{B}} T}{4\omega} D(E = -k_{\mathrm{B}} T \log(\omega\tau_0)). \tag{7.7}$$

Assuming a Gaussian form for $D(E)$ and $\mu = 5$ D (a common assumption for dipoles on the atomic scale), then $\sigma_d \approx 7 - 10 \times 10^{18}$ m^{-2}, or approximately 7-10 TAF dipoles per square nanometer. We note here that the roughness of the trap surface increases the effective surface area and that noise sources near the surface may play a role, both making a volumetric density a maybe more appropriate measure.

Connection to solid state systems

The TAF model as presented in the previous section was developed by Dutta, Dimon, and Horn [5] to explain resistance fluctuations in metal films. Many experiments since then have confirmed that the likely cause of the noise is defect migration. Defects in the metal lattice serve as scattering centers for electrons as they move through the metal. If those defects are mobile, then the effective scattering cross-section for electrons depends on their orientation. Several experiments have confirmed that the fluctuations also happen in equilibrium [63]. By applying a current, the equilibrium fluctuations can be amplified and measured as current noise.

These experiments revealed several properties of the mechanism behind the noise. By studying volume and grain size dependencies, and the effects of annealing, it was determined that processes on the grain boundaries are the dominant source of noise with energy barriers in the range of 0.3-1.0 eV [64, 65, 66]. Furthermore, Biery *et al.* extracted energy of formation and migration of noise processes in Al and Al-Cu films to determine the process causing $1/f$ noise was motion of Al along grain boundaries [67]. The addition of Cu only affects Al motion along the grain boundary, not in the bulk of the grain, and an increase in activation energy when Cu is added was expected and observed by Koch *et al.* [68].

There are similarities between our system and these solid state results. The trap electrodes are also an Al-Cu material, and SEM images of similar samples reveal a fine-grained structure of the metal with many grain boundaries that could be locations for defect migration. Measurements such as the ones in Al-Cu films by Koch *et al.* [68] show a similar correspondence to the TAF model, with energy barriers peaking in the same region, around $0.5 - 0.6$ eV. The similarities suggest that the noise in our surface trap is potentially related to defect migration on the grain boundaries. However, there is still a very open question as to how this motion could translate into an electric-field fluctuation. Other factors such as work function variations, oxide layer defects, and contaminate dipoles stuck to the surface likely play a role in conjunction with defect dynamics.

One curious property of observed $1/f$ noise in metal films and semiconductors is that a low-frequency 'cut-off' or 'rollover' into a flat spectrum has never been observed [60]. In a finite size sample, there is a finite limit to the height and width of the energy barriers, resulting an a maximum characteristic relaxation time, or equivalently a minimum frequency τ^{-1} where the spectrum should reach a finite value. While physically such a frequency must exist, the corresponding measurement time could be as long as the age of the universe. Some of the lowest measurements were down to 10^{-7} Hz [69]. This property is one of the remaining paradoxes of the model.

7.6 Other models

Previous temperature scaling results have fit either a power law or Arrhenius-type behavior, and in this section we explore the relevance of those functional forms to our data. A power

Location	Power Law T^γ		Arrhenius $e^{-T_0/T}$		
	γ	χ^2_P	T_0	E_b	χ^2_A
1	1.4(1)	5.1	550(40)	0.047(3)	2.6
2	1.6(1)	2.7	620(33)	0.053(3)	1.7
3	1.1(1)	2.8	430(40)	0.037(3)	1.9

Table 7.1: Summary of fit parameters for power law and Arrhenius dependence. The values of the reduced χ^2 indicate the goodness of fit.

law ($\dot{\bar{n}} = \dot{\bar{n}}_0 T^\gamma$) is a common result in heating rate temperature scalings. We find that the temperature exponent γ for our data is similar to those from Bruzewicz *et al.* [42], but the values of the reduced χ^2 are large, presented as χ^2_P in Table 7.1. There is no known model for a power law scaling of this type. Arrhenius behavior ($\dot{\bar{n}} = \dot{\bar{n}}_0 e^{-T_0/T}$) has also been observed in heating rate temperature scaling results. Previous published values of T_0 are 40 K [40], 45 K and 63 K [36]. The values of T_0 for our data are an order of magnitude higher (Table 7.1) and vary by several σ from one location on the trap to another. The statistical uncertainties of our data also result in high values for reduced χ^2, presented as χ^2_A in Table 7.1, but an underestimation of those uncertainties such as an unaccounted for systematic error could be the reason. Beyond the applicability of the functional form, we discuss the implications of the observed fits in terms of two possible physical models that have Arrhenius behavior: diffusion adatom dipoles and fixed fluctuating dipoles.

Diffusion

One proposed model for electric field noise is based on the diffusion of adatom dipoles around on the surface of the trap. The rearrangement of adatoms causes spatial fluctuations in the density of charges. Several experiments have seen frequency scaling results that support this hypothesis [44, 32].

Thermally activated diffusion is described by a diffusion constant at high temperatures of

$$D = D_0 e^{-E_\mathrm{b}/k_\mathrm{B}T} \tag{7.8}$$

where E_b is the diffusion barrier. Diffusion on a smooth, infinite, planar surface is described by [19]

$$S_\mathrm{E} \propto \frac{D_0 e^{-E_\mathrm{b}/k_\mathrm{B}T}}{\omega^2}. \tag{7.9}$$

First we note that the frequency scaling we measure is $1/f$, not a $1/f^2$ dependency predicted by this model. As summarized in Table 7.1, we find diffusion barriers, $E_\mathrm{b} = T_0/k_\mathrm{B}$, of about 0.05 eV. These energy barriers are very low compared to the calculated possible energy barriers in gold traps by Kim *et al.* [34] of 0.13-0.57 eV. The possible energy barriers in aluminum or a disordered aluminum-oxide are unknown to us.

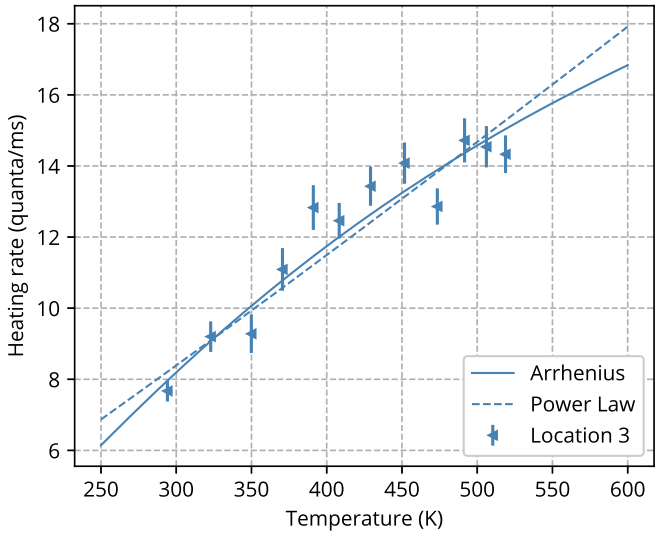

Figure 7.6: Temperature scaling data at Location 3 with a fit to an Arrhenius curve (solid) and a power law (dashed). The resultant fit parameters are summarized in Table 7.1 and the implications are discussed in Sec. 7.6.

Adatom Dipoles

Adatoms close to a surface are attracted by the van der Waals force, but repelled by electronic wavefunction overlap at distances too close to the surface [19]. This balance of forces results in a potential minimum at distances of a few angstroms from the surface, creating an induced surface dipole moment. This dipole moment can fluctuate due to phonon-induced transitions between vibrational states in the attractive potential. [38] The frequency spacing of these vibrational states, ν_{10}, depends on the adatom, but is typically around 1 THz, which corresponds to the zero temperature decay rate from the excited to ground state, Γ_0, of 1 to a few hundred MHz.

If there is a distribution of transition rates from several different energy levels, even for a single dipole, there will be a regime where the noise scales as $1/f$ and the temperature scaling follows an Arrhenius curve [38]. We can estimate where in frequency this $1/f$ region would occur and evaluate the model by fitting our data to $\dot{\bar{n}} = \dot{\bar{n}}_0 e^{-T_0/T}$.

The results of fits at each location are shown in Table 7.1, and T_0 is on average 530 K. This value T_0 would suggest that $\nu_{10} \approx 11$ THz , which is larger than the Debye frequency of 8 THz in aluminum [70]. In polycrystalline materials, such as our trap, the Debye frequency is even lower due to the excess volume [71], ruling out phonon-driven dipole fluctuations.

We can also use the average of value of T_0 to estimate where the $1/f$ region would occur in terms of frequency. The zero temperature decay rate, Γ_0, depends on properties of the

material, and the bound adatom [38]:

$$\Gamma_0 = \frac{1}{4\pi}\frac{\nu_{10}^4 m}{v^3 \rho} \tag{7.10}$$

which only holds if $\nu_{10} < \omega_{\mathrm{D}}$, the Debye frequency of the bulk material. In aluminum, the speed of sound is $v = 6320$ m/s, and the density is $\rho = 2.7$ g/cm^3. For these parameters, $\Gamma_0 = 10$ THz. The $1/f$ region begins around $\omega_c \approx \Gamma_0[1 + (e^{h\nu_{10}/k_{\mathrm{B}}T} - 1)^{-1}]$, which for the highest temperatures measured in this work, is approximately $1.6\times\Gamma_0 = 16$ THz, suggesting that in our measurement range the frequency scaling would still be flat. To summarize, the combined frequency and temperature scaling we observe is not compatible with the adatom dipole model as outlined by Savfavi-Naini *et al.* [38] due to the physical inconsistencies with the model and the observed parameters in our results.

Chapter 8

Summary and outlook

This thesis began with an overview of aspects of quantum control of trapped ions (Chapter 2). We focused on the operation of surface ion traps, which are are designed for scaling trapped-ion systems into many-qubit quantum-computing devices. The main method for taking data in this work used Rabi flops on the $|S\rangle \rightarrow |D\rangle$ transition, and we outlined how these Rabi flops can be used to read out the motional mode occupation of a trapped ion. To measure a heating rate of the motional mode, Rabi flops were measured with increasing wait time after Doppler cooling. There are other methods for measuring heating rates that are not discussed in this work such as motional sideband comparisons [9], and it may be instructive in the future to compare these methods including their possible systematic biases.

Heating rate measurements with trapped ions are used to probe electric-field noise above surfaces. In Chapter 3, we explored the the potential problems that electric-field noise creates for the future of trapped ion qubits. While in the short term electric-field noise may not be a major limiting factor in gate fidelities, as we move forward in the field, they are likely to become a major obstacle. We argued that observed excess electric-field noise in ion traps is not well understood, and uncovering the mystery may be key to the future of scalable ion trap systems. We outlined why the surface of the trap itself is believed to be the main cause of the excess noise. We focused particularly on the behavior of electric-field noise with changing temperature and summarized previous results in the field. Finally, there are several experimental considerations for measuring electric-field noise that were discussed. The setup used for measurements in this work was described in detail in Chapter 4, including the unique heater that was used for above room temperature explorations of electric-field noise. The heater is what enabled the new, high-temperature measurements of electric-field noise presented in this thesis.

In Chapter 5, we explored possibilities for high-temperature effects using the special in vacuum heater in use in this work. Those possibilities include desorption of contaminants from the surface, and we presented relevant desorption temperatures for various contaminants from a gold surface from our collaborators at Lawerence-Livermore National Laboratory. More relevant information for our studies might be desorption from a rough surface, and there could be experiments that explore desorption as a method for surface cleaning. The

second possibility that was explored was annealing of the metal trap electrodes. Several tests were done to explore the viability of annealing traps *in situ*, and we concluded that the current trap composition of aluminum and copper will likely melt and cause trap damage before undergoing any kind of phase change. However, we discussed the idea of using a 4wt% Al-Cu composition to achieve a solid state phase transition. This type of in situ change of the microstructure of the electrodes would be a new exploration of electric-field noise that might be separate from the effects of contaminants. More tests should be done to fully characterize the phase transition using fused silica substrates, *ex situ* annealing, and SEM or potentially AFM for imaging the samples.

For this work, the heater was used to measure the temperature and frequency scaling of electric-field noise, and in Chapter 6, we presented the results of those measurements. We ruled out technical noise to confirm that the results were reflective of surface-related noise. The frequency scaling showed a decrease in the power-law exponent at high temperatures, and we quantified that decrease using a t-test. This decrease was relevant to the interpretation of the data in the context of the thermally-activated fluctuator (TAF) model.

An understanding of the results was explained in terms of the TAF model in Chapter 7. The model was explored in detail, including intuitive explanations for the expected behavior of noise due to TAF. When the TAF model was applied to the temperature scaling data, the result was a distribution of fluctuators with energy barriers in the range of 0.5 eV. The shape of the distribution led to a prediction of the behavior of the frequency scaling exponent that was consistent with the decrease observed in the data. We believe that the TAF model is the best model to describe both our frequency and temperature scaling data. We also note that this might be the first ion trap electric-field noise study where a single model corresponds to the temperature and frequency scaling data together.

Finally, we discussed that the TAF model was developed to explain resistance fluctuations in metal films that are associated with defect dynamics [5, 59]. The common theoretical description and similarity of the physical systems suggests that maybe defect dynamics should be considered in future models for electric-field noise in ion traps. Many of the results in metal films suggest that metal defect motion at grain boundaries in particular contribute dominantly to the resistance noise [67, 65, 68]. A major open question remains as to how motion of a metal defect, such as a vacancy, could lead to electric-field fluctuations that are large enough to explain observed levels of noise. Future experiments might explore the effects of metal microstructure more directly, such as grain boundary changes or surface roughness variations. Electric-field noise in surface ion traps is a complex phenomenon to understand. If we hope to solve the problem in the future, experiments such as these high-temperature studies must continue to illuminate the underlying physical causes.

Bibliography

[1] Iulia Buluta and Franco Nori. "Quantum simulators." In: *Science* 326.5949 (2009), pp. 108–11. ISSN: 1095-9203. DOI: 10.1126/science.1177838. URL: http://www.ncbi.nlm.nih.gov/pubmed/19797653.

[2] Gabriel Popkin. "Quest for Qubits". In: *Science (80-.).* 354.6316 (2016), p. 1091.

[3] J. Burnett et al. "Evidence for interacting two-level systems from the 1/f noise of a superconducting resonator". In: *Nat. Commun.* 5.1 (2014), p. 4119. ISSN: 2041-1723. DOI: 10.1038/ncomms5119. URL: http://www.nature.com/articles/ncomms5119.

[4] M. Kim et al. "Decoherence of Near-Surface Nitrogen-Vacancy Centers Due to Electric Field Noise". In: *Phys. Rev. Lett.* 115.8 (2015), p. 087602. ISSN: 0031-9007. DOI: 10.1103/PhysRevLett.115.087602. URL: https://link.aps.org/doi/10.1103/PhysRevLett.115.087602.

[5] P. Dutta, P. Dimon, and P. M. Horn. "Energy Scales for Noise Processes in Metals". In: *Phys. Rev. Lett.* 43.9 (1979), pp. 646–649. ISSN: 0031-9007. DOI: 10.1103/PhysRevLett.43.646. URL: https://link.aps.org/doi/10.1103/PhysRevLett.43.646.

[6] Clemens Müller, Jared H Cole, and Jürgen Lisenfeld. "Towards understanding two-level-systems in amorphous solids-Insights from quantum circuits". In: *Arxiv Prepr.* (2018). arXiv: 1705.01108v2. URL: https://arxiv.org/pdf/1705.01108.pdf.

[7] W A Phillips. "Two-level states in glasses". In: *Reports Prog. Phys.* 50.12 (1987), p. 1657.

[8] J D Jackson. *Classical Electrodynamics*. 3rd editio. John Wiley \& Sons, New York, 1998.

[9] Christian Felix Roos. "Controlling the quantum state of trapped ions". Doctoral thesis. University of Innsbruck, 2000.

[10] D. Leibfried et al. "Quantum dynamics of single trapped ions". In: *Rev. Mod. Phys.* 75.1 (2003), pp. 281–324. ISSN: 0034-6861. DOI: 10.1103/RevModPhys.75.281. URL: http://dx.doi.org/10.1103/RevModPhys.75.281.

[11] J. Chiaverini et al. "Surface-electrode architecture for ion-trap quantum information processing". In: *Quantum Inf. Comput.* 5 (2005), pp. 419–439. URL: http://arxiv.org/abs/quant-ph/0501147.

[12] C E Pearson et al. "Experimental investigation of planar ion traps". In: *Phys. Rev.* 73 (2006), p. 32307. DOI: 10.1103/PhysRevA.73.032307. URL: https://journals.aps.org/pra/pdf/10.1103/PhysRevA.73.032307.

[13] Signe Seidelin et al. "Microfabricated surface-electrode ion trap for scalable quantum information processing." In: *Phys. Rev. Lett.* 96 (2006), p. 253003. URL: https://www.nist.gov/publications/microfabricated-surface-electrode-ion-trap-scalable-quantum-information-processing.

[14] N Daniilidis et al. "Fabrication and heating-rate study of microscopic surface electrode traps". In: *New J. Phys.* 13 (2011), p. 013032. DOI: 10.1088/1367-2630/13/1/013032. arXiv: arXiv:1009.2834. URL: http://iopscience.iop.org/article/10.1088/1367-2630/13/1/013032/meta.

[15] Hao-Kun Li et al. "Realization of Translational Symmetry in Trapped Cold Ion Rings". In: *Phys. Rev. Lett.* 118.5 (2017), p. 053001. ISSN: 10797114. DOI: 10.1103/PhysRevLett.118.053001. arXiv: 1605.02143 [arXiv:quant-ph]. URL: https://link.aps.org/doi/10.1103/PhysRevLett.118.053001.

[16] Peter Maunz. *High Optical Access Trap 2.0*. Tech. rep. Albuquerque, NM, and Livermore, CA (United States): Sandia National Laboratories, 2016, pp. 796–2016. DOI: 10.2172/1237003. URL: http://prod.sandia.gov/techlib/access-control.cgi/2016/160796r.pdf.

[17] F Schmidt-Kaler et al. "The coherence of qubits based on single Ca+ ions". In: *J. Phys. B At. Mol. Opt. Phys.* 36 (2003), p. 623.

[18] T.W. W Hänsch and A.L. L Schawlow. "Cooling of gases by laser radiation". In: *Opt. Commun.* 13.1 (1975), pp. 68–69. ISSN: 0030-4018. DOI: 10.1016/0030-4018(75)90159-5. URL: https://www.sciencedirect.com/science/article/pii/0030401875901595.

[19] M. Brownnutt et al. "Ion-trap measurements of electric-field noise near surfaces". In: *Rev. Mod. Phys.* 87.4 (2015), pp. 1419–1482. ISSN: 0034-6861. DOI: 10.1103/RevModPhys.87.1419. arXiv: 1409.6572v1. URL: http://link.aps.org/doi/10.1103/RevModPhys.87.1419.

[20] R. Bowler et al. "Coherent Diabatic Ion Transport and Separation in a Multizone Trap Array". In: *Phys. Rev. Lett.* 109.8 (2012), p. 080502. ISSN: 0031-9007. DOI: 10.1103/PhysRevLett.109.080502. URL: https://link.aps.org/doi/10.1103/PhysRevLett.109.080502.

[21] D. T. C. Allcock et al. "A microfabricated ion trap with integrated microwave circuitry". In: *Appl. Phys. Lett.* 102.4 (2013), p. 44103. ISSN: 0003-6951. DOI: 10.1063/1.4774299. URL: http://aip.scitation.org/doi/10.1063/1.4774299.

[22] N Daniilidis et al. "Wiring up trapped ions to study aspects of quantum information". In: *J. Phys. B* 42.15 (2009), p. 154012. ISSN: 0953-4075. DOI: 10.1088/0953-4075/42/15/154012. URL: http://stacks.iop.org/0953-4075/42/i=15/a=154012?key=crossref.c85ec400f8b1c300df78abfce5d7ce88.

[23] J I Cirac and P Zoller. "Quantum Computations with Cold Trapped Ions." In: *Phys. Rev. Lett.* 74.20 (1995), pp. 4091–4094. ISSN: 0031-9007. URL: http://www.ncbi.nlm.nih.gov/pubmed/10058410.

[24] A Sørensen and K Mølmer. "Quantum Computation with Ions in Thermal Motion". In: *Phys. Rev. Lett.* 82 (1999), p. 1971. DOI: 10.1103/PhysRevLett.82.1971.

[25] G Kirchmair et al. "Deterministic entanglement of ions in thermal states of motion". In: *New J. Phys.* 11.2 (2009), p. 23002. ISSN: 1367-2630. DOI: 10.1088/1367-2630/11/2/023002. URL: http://stacks.iop.org/1367-2630/11/i=2/a=023002?key=crossref.be3fc247c634554dc69f59ebce95a834.

[26] J.P. P. Gaebler et al. "High-Fidelity Universal Gate Set for Be 9 + Ion Qubits". In: *Phys. Rev. Lett.* 117.6 (2016), p. 060505. ISSN: 0031-9007. DOI: 10.1103/PhysRevLett.117.060505. URL: https://link.aps.org/doi/10.1103/PhysRevLett.117.060505.

[27] J. B. Johnson. "Thermal Agitation of Electricity in Conductors". In: *Phys. Rev.* 32.1 (1928), pp. 97–109. ISSN: 0031-899X. DOI: 10.1103/PhysRev.32.97. URL: https://link.aps.org/doi/10.1103/PhysRev.32.97.

[28] H. Nyquist. "Thermal Agitation of Electric Charge in Conductors". In: *Phys. Rev.* 32.1 (1928), pp. 110–113. ISSN: 0031-899X. DOI: 10.1103/PhysRev.32.110. URL: https://link.aps.org/doi/10.1103/PhysRev.32.110.

[29] David Leibrandt, Bernard Yurke, and Richart Slusher. "Modeling ion trap thermal noise decoherence". In: *Quantum Inf. Comput.* 7.1 (2007), pp. 52–072. URL: http://www.rintonpress.com/xqic7/qic-7-12/052-072.pdf.

[30] N. Daniilidis et al. "Surface noise analysis using a single-ion sensor". In: *Phys. Rev. B* 89.24 (2014), p. 245435. ISSN: 1098-0121. DOI: 10.1103/PhysRevB.89.245435. URL: http://link.aps.org/doi/10.1103/PhysRevB.89.245435.

[31] J. W.C. De Vries. "Temperature and thickness dependence of the resistivity of thin polycrystalline aluminium, cobalt, nickel, palladium, silver and gold films". In: *Thin Solid Films* 167.1-2 (1988), pp. 25–32. ISSN: 00406090. DOI: 10.1016/0040-6090(88)90478-6.

[32] D. A. Hite et al. "100-Fold Reduction of Electric-Field Noise in an Ion Trap Cleaned with In Situ Argon-Ion-Beam Bombardment". In: *Phys. Rev. Lett.* 109.10 (2012), p. 103001. DOI: 10.1103/PhysRevLett.109.103001. arXiv: arXiv:1112.5419v1. URL: http://link.aps.org/doi/10.1103/PhysRevLett.109.103001.

[33] C. Noel et al. "Electric-field noise from thermally-activated fluctuators in a surface ion trap". In: *Arxiv Prepr.* (2018). arXiv: 1809.05624. URL: http://arxiv.org/abs/1809.05624.

[34] E. Kim et al. "Electric-field noise from carbon-adatom diffusion on a Au(110) surface: First-principles calculations and experiments". In: *Phys. Rev. A* 95 (2017), p. 033407. ISSN: 24699934. DOI: 10.1103/PhysRevA.95.033407. arXiv: 1610.01079.

[35] D T C Allcock et al. "Reduction of heating rate in a microfabricated ion trap by pulsed-laser cleaning". In: *New J. Phys.* 13.12 (2011), p. 123023. ISSN: 1367-2630. DOI: 10.1088/1367-2630/13/12/123023. URL: http://stacks.iop.org/1367-2630/13/i=12/a=123023?key=crossref.a64e2d675f5dd69983a07d7624d8928d.

[36] J. A. Sedlacek et al. "Distance scaling of electric-field noise in a surface-electrode ion trap". In: *Phys. Rev. A* 97 (2018), p. 20302. DOI: 10.1103/PhysRevA.97.020302. arXiv: 1712.00188.

[37] Muir Kumph et al. "Electric-field noise above a thin dielectric layer on metal electrodes". In: *New J. Phys.* 18.2 (2016), p. 023020. ISSN: 13672630. DOI: 10.1088/1367-2630/18/2/023020. arXiv: 1511.00624. URL: http://stacks.iop.org/1367-2630/18/i=2/a=023020?key=crossref.130a28137e2c845665e6d27aecf345a9.

[38] A. Safavi-Naini et al. "Microscopic model of electric-field-noise heating in ion traps". In: *Phys. Rev. A* 84.2 (2011), p. 023412. DOI: 10.1103/PhysRevA.84.023412. URL: http://link.aps.org/doi/10.1103/PhysRevA.84.023412.

[39] L Deslauriers et al. "Efficient photoionization loading of trapped ions with ultrafast pulses". In: *Phys. Rev. A* 74 (2006), p. 63421.

[40] J Labaziewicz et al. "Suppression of Heating Rates in Cryogenic Surface-Electrode Ion Traps". In: *Phys. Rev. Lett.* 100 (2008), p. 013001. DOI: 10.1103/PhysRevLett.100.013001. URL: http://journals.aps.org/prl/abstract/10.1103/PhysRevLett.100.013001.

[41] Jaroslaw Labaziewicz et al. "Temperature Dependence of Electric Field Noise Above Gold Surfaces". In: *Phys. Rev. Lett.* 101 (2008), p. 180602. URL: http://journals.aps.org/prl/abstract/10.1103/PhysRevLett.101.180602.

[42] C. D. Bruzewicz, J. M. Sage, and J. Chiaverini. "Measurement of ion motional heating rates over a range of trap frequencies and temperatures". In: *Phys. Rev. A - At. Mol. Opt. Phys.* 91 (2015), p. 041402. ISSN: 10941622. DOI: 10.1103/PhysRevA.91.041402. arXiv: 1412.5119.

[43] J. Chiaverini and J. M. Sage. "Insensitivity of the rate of ion motional heating to trap-electrode material over a large temperature range". In: *Phys. Rev. A* 89.1 (2014), p. 012318. ISSN: 1050-2947. DOI: 10.1103/PhysRevA.89.012318. arXiv: 1310.4385. URL: http://link.aps.org/doi/10.1103/PhysRevA.89.012318.

[44] Q A Turchette et al. "Heating of trapped ions from the quantum ground state". In: *Phys. Rev. A* 61 (2000), p. 063418. DOI: 10.1103/PhysRevA.61.063418.

[45] DJ Berkeland et al. "Minimization of ion micromotion in a Paul trap". In: *J. Appl. Phys.* 83.10 (1998), p. 5025. ISSN: 00218979. DOI: 10.1063/1.367318. arXiv: 1211.0101. URL: http://link.aip.org/link/?JAPIAU/83/5025/1.

[46] Thaned Pruttivarasin. "Spectroscopy , fundamental symmetry tests and quantum simulation with trapped ions". PhD thesis. University of California, Berkeley, 2014, p. 141.

[47] D. Gorman. "Noise sensing and quantum simulation with trapped atomic ions". PhD Thesis. University of California, Berkeley, 2018. URL: http://research.physics.berkeley.edu/haeffner/publications/dylan{_}gorman{_}thesis.pdf.

[48] Keith G. Ray et al. "vdW-corrected density functional study of electric field noise heating in ion traps caused by electrode surface adsorbates". In: *arXiv Prepr.* (2018). arXiv: 1810.10199. URL: http://arxiv.org/abs/1810.10199.

[49] P.A. Redhead. "Thermal desorption of gases". In: *Vacuum* 12.4 (1962), pp. 203–211. ISSN: 0042-207X. DOI: 10.1016/0042-207X(62)90978-8. URL: https://www.sciencedirect.com/science/article/pii/0042207X62909788.

[50] J A Sedlacek et al. "Evidence for multiple mechanisms underlying surface electric-field noise in ion traps". In: *Phys. Rev. A* 98 (2018), p. 63430. ISSN: 24699934. DOI: 10.1103/PhysRevA.98.063430. arXiv: 1809.07761. URL: https://journals.aps.org/pra/pdf/10.1103/PhysRevA.98.063430.

[51] P. Riani et al. "Ternary rare-earth aluminum systems with copper: A review and a contribution to their assessment". In: *J. Phase Equilibria Diffus.* 25.1 (2004), pp. 22–52. ISSN: 1547-7037. DOI: 10.1007/s11669-004-0169-7. URL: http://link.springer.com/10.1007/s11669-004-0169-7.

[52] M H Jacobs. *TALAT Lecture 1204 Precipitation Hardening*. Tech. rep. Interdisciplinary Research Centre in Materials, The University of Birmingham, UK, 1999.

[53] William S. Cleveland. "Robust Locally Weighted Regression and Smoothing Scatterplots". In: *J. Am. Stat. Assoc.* 74.368 (1979), pp. 829–836. ISSN: 0162-1459. DOI: 10.1080/01621459.1979.10481038. URL: http://www.tandfonline.com/doi/abs/10.1080/01621459.1979.10481038.

[54] D.C. Giancoli. *Physics: Principles with Applications, 7th Edition*. 7th ed. Pearson, 2014. ISBN: 9780321625922.

[55] Student. "The Probable Error of a Mean". In: *Biometrika* 6.1 (1908), p. 1. ISSN: 00063444. DOI: 10.2307/2331554. URL: https://www.jstor.org/stable/2331554?origin=crossref.

[56] M. Surdin. "Fluctuations de courant thermionique et le Flicker effect ". In: *J. Phys. le Radium* 10.4 (1939), pp. 188–189. ISSN: 0368-3842. DOI: 10.1051/jphysrad:01939001004018800. URL: http://www.edpsciences.org/10.1051/jphysrad:01939001004018800.

[57] F. K. Du Pré. "A Suggestion Regarding the Spectral Density of Flicker Noise". In: *Phys. Rev.* 78.5 (1950), pp. 615–615. ISSN: 0031-899X. DOI: 10.1103/PhysRev.78.615. URL: https://link.aps.org/doi/10.1103/PhysRev.78.615.

[58] A Van Der Ziel. "On the noise spectra of semi-conductor noise and of flicker effect". In: *Physica* XVI.4 (1950). URL: http://pessina.mib.infn.it/WOLTE2014/vanderziel/1-s2.0-0031891450900784-main.pdf.

[59] P. Dutta and P. M. Horn. "Low-frequency fluctuations in solids: 1/f noise". In: *Rev. Mod. Phys.* 53 (1981), pp. 497–516. DOI: 10.1103/RevModPhys.53.497.

[60] Sh. Kogan. *Electronic noise and fluctuations in solids*. Cambridge University Press, 1996. ISBN: 0521070198. URL: https://books.google.com/books/about/Electronic{_}Noise{_}and{_}Fluctuations{_}in{_}Sol.html?id=s5tupGCMzBYC.

[61] Svante Arrhenius. "Über die Reaktionsgeschwindigkeit bei der Inversion von Rohrzucker durch Säuren". In: *Zeitschrift für Phys. Chemie* 4U.1 (1889), pp. 226–248. ISSN: 2196-7156. DOI: 10.1515/zpch-1889-0416. URL: http://www.degruyter.com/view/j/zpch.1889.4.issue-1/zpch-1889-0416/zpch-1889-0416.xml.

[62] C. Kittel. *Introduction to Solid State Physics*. Third. John Wiley & Sons, New York, 1966.

[63] Richard F. Voss and John Clarke. "Flicker (1 / f) noise: Equilibrium temperature and resistance fluctuations". In: *Phys. Rev. B* 13.2 (1976), pp. 556–573. DOI: 10.1103/PhysRevB.13.556. URL: https://link.aps.org/doi/10.1103/PhysRevB.13.556.

[64] D. M. Fleetwood and N. Giordano. "Direct link between 1/f noise and defects in metal films". In: *Phys. Rev. B* 31 (1985), p. 1157. ISSN: 01631829. DOI: 10.1103/PhysRevB.31.1157.

[65] Marc J C Van Den Homberg et al. "Electromigration and 1/f noise in single-crystalline, bamboo and polycrstalline Al lines". In: *Mat. Res. Soc. Symp. Proc* 473 (1997), p. 211. DOI: 10.1557/PROC-473-211. URL: https://doi.org/10.1557/PROC-473-211.

[66] J. A. Schwarz et al. "Grain size dependence of 1/f noise in Al-Cu thin-film interconnections". In: *J. Appl. Phys.* 70.3 (1991), pp. 1561–1564. ISSN: 00218979. DOI: 10.1063/1.349545.

[67] Glenn A Biery, Richard G Smith, and Peter J Ficalora. "Temperature dependence of the 1/f noise in heat-treated films of Al and Al-Cu". In: *Mat. Res. Soc. Symp. Proc* 309 (1993), pp. 313–320.

[68] R. H. Koch, J. R. Lloyd, and J. Cronin. "1/f noise and grain-boundary diffusion in aluminum and aluminum alloys". In: *Phys. Rev. Lett.* 55 (1985), p. 2487. ISSN: 00319007. DOI: 10.1103/PhysRevLett.55.2487.

[69] C. E. Parman, N. E. Israeloff, and J. Kakalios. "Conductance-noise power fluctuations in hydrogenated amorphous silicon". In: *Phys. Rev. Lett.* 69.7 (1992), pp. 1097–1100. ISSN: 0031-9007. DOI: 10.1103/PhysRevLett.69.1097. URL: https://link.aps.org/doi/10.1103/PhysRevLett.69.1097.

[70] D R Chipman. "Temperature Dependence of the Debye Temperatures of Aluminum, Lead, and Beta Brass by an X-Ray Method". In: *J. Chem. Phys.* 31 (1960), p. 3966. DOI: 10.1063/1.1735487. URL: https://doi.org/10.1063/1.1735487.

[71] Michael Wagner. “Structure and thermodynamic properties of nanocrystalline metals”. In: *Phys. Rev. B* 45.2 (1992), pp. 635–639. ISSN: 0163-1829. DOI: 10.1103/PhysRevB.45.635. URL: https://link.aps.org/doi/10.1103/PhysRevB.45.635.